



**Codes And Methods Improvements
for VVER comprehensive safety assessment**

Grant Agreement Number: 945081

Start date: 01/09/2020 - Duration: 36 Months

**D4.6 – Assessment of new advanced 2D and 3D
models in neutronic multi-parameter library generation**

S. Santandrea (CEA)

M. Tibergera, E. Noblat (EDF)

L. Graziano, B. Vezzoni, A. Brighenti (Framatome)

Version 1 – 31/08/2023



This project has received funding from the Euratom research and training program 2019-2020 under grant agreement No 945081.

CAMIVVER – Grant Agreement Number: 945081

Document title	Assessment of new advanced 2D and 3D models in neutronic multi-parameter library generation
Author(s)	S. Santandrea, M. Tiberga, E. Noblat, L. Graziano, B. Vezzoni, A. Brighenti
Document Type	Deliverable
Work Package	WP4
Document number	D4.6 – version 1
Issued by	CEA
Date of completion	31/08/2023
Dissemination level	Public

Summary

In this report we describe the work done in task 4.4, this consists of three main contributions. These are a new 3D transport method aimed at correctly compute depleted situations, then a set of advanced numerical models of the heavy reflector to underweight some of the main geometrical approximations done in classical schemes and finally we present a new 2D transport scheme that we will propose in next future for full scale 2D reactor core calculations.

The first item concerns the development and validation of a 3D deterministic tool to compute reference assembly solutions. This tool, comprised of its environment to couple with the necessary depletion and self-shielding capabilities of the APOLLO3® code, can be used to compute the axial reflector without approximations, model which is not carried out in the classical computational schemes. The work presented here show the first systematic validations of this approach against Monte Carlo (MC) results obtained with TRIPOLI-4® code.

For the second theme, we show that some approximations currently used in the nuclear industry, for example French, to model the heavy reflectors can give some power discrepancies at the core periphery. In particular transforming the curved geometry of the reflector into a one segmented Cartesian one determines local errors in pin by pin reaction rates that can exceed 10% when compared against MC codes. Analogously the fact of smearing the water holes into a homogenized medium can contribute for important local errors. Investigations have been carried out on PWR configuration (KAIST core) before applying to VVER ones.

Finally, the third item concerns the development of a higher order scheme in the solver TDT-MOC of the APOLLO3® code which has the precise intent, for future calculations, to address full 2D core scale calculations with high fidelity transport methods and a computational cost affordable with small cluster machines.

Approval


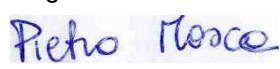

Version	First Author	WP leader	Project Coordinator
1	S. Santandrea (CEA) 31/08/2023	P. Mosca (CEA) 31/08/2023	D. Verrier (Framatome) 31/08/2023
	Signature 1 st author 	Signature WP leader 	Signature Coordinator 

Table of contents

Table of contents	3
1 Context	5
2 Basic 3D transport methods and computational issues treated in this deliverable	7
2.1 The polynomial expansion	7
2.2 Free transport iterations	8
2.3 Balance equation	9
2.3.1 Description of the term $Zrqlm$	10
2.3.2 Description of the term $\Delta l, rm$	11
2.3.3 Description of Γrm	12
2.5 Depletion coupling	13
2.5.1 3D case description and benchmarking.....	14
2.5.2 Context for a correct comparison between Monte-Carlo and deterministic calculation along depletion	16
2.5.3 Comparison of TRIPOLI-4 [®] vs APOLLO-3 [®] results	18
3 Advanced reflector modeling with APOLLO3[®]	23
3.2.1 Influence of a multi-zones self-shielding model	29
3.3 Evaluating the reflector modelling	32
3.3.1 Case 1: Homogenized cylindrical reflector.....	32
3.3.2 Case 2: homogenized Cartesian reflector (1 assembly step)	34
3.3.3 Case 3: homogenized Cartesian reflector (0.5 assembly step)	35
3.3.4 Case 4: homogenized Cartesian reflector (0.5 assembly step + square) ...	37
3.3.5 Case 5: homogenized Cartesian reflector (preserved volume).....	38
3.3.6 Case 6: homogenized Cartesian reflector (cell step)	40
3.3.7 Case 7: exact cylindrical reflector + multi-zone + octagonal water holes....	41
3.3.8 Case 8: exact cylindrical reflector + extended fuel slice	43
4 The new LS-xy method	44
4.1 The LS scheme	44
4.1.1 Transmission equation	45
4.1.2 Geometric average	46
4.1.3 Balance equation	47
4.1.4 Enforce conservation	47
4.2 The LS-xy method.....	48
4.2.1 Source approximation.....	48
4.2.2 Transmission equation	49
4.2.3 Geometric averages	50
4.2.4 Constant balance.....	51
4.2.5 Linear balance	51
4.2.6 Enforce conservation in LSxy	54
4.3 Some selected results.....	54
5 Conclusions	57

- 6 References59**
- 7 Appendix A: Contribution to KAIST-like core preliminary analyses using newly developed Python libraries for automatize ALAMOS use.....61**
- 8 APPENDIX B – Validation MOC3D: pin by pin reaction rates65**

1 Context

Within the H2020 CAMIVVER Project [1] Work Package 4 (WP4) aims to set up the framework for the development of an industrial calculation platform for neutronic lattice analysis and generating multi-parameter data libraries for core calculations using APOLLO3[®] [2], the new generation deterministic code developed by the Commissariat à l'Énergie Atomique et aux Énergies Alternatives (CEA) with the support of Framatome and Électricité de France (EDF).

This document corresponds to Deliverable 4.6: “*Assessment of new advanced 2D and 3D models in neutronics multi-parametric library generation*”, and it summarizes the work done inside the Task 4.4. The basic guidelines that were pursued in this task are of three types:

1. We developed a new method to compute 3D typical geometries for reactor physics applications in order to correctly model phenomena that are currently neglected in classical calculations, such as flux depression in grids or the thermal flux pic present in the axial reflector. We modeled these 3D phenomena not only in static calculations (where reference Monte Carlo calculations can currently be used) but also along depletion (where Monte Carlo simulations are extremely expensive and thus difficult to carry out). This last aspect is the main theoretical progress we developed with respect to pre-existing literature. The development of this new method has produced, among conference papers, a journal paper [5]. In this note, we also discuss supplementary results to benchmark the proposed approach.
2. We performed a set of studies to underweight the approximations that are usually adopted for heavy reflector modeling in the nuclear industry, for example French. Usually, the reflector model is based on slab preliminary lattice calculations [18] that are used to produce macroscopic cross sections under a conservation principle of some quantity of interest (typically albedos). These cross sections are then adopted to perform calculation at the core level, without the need for an explicit reflector model. It is worth noting that other approaches [19],[20],[21] exist where a 2D model of the reflector is used to produce macroscopic cross sections and an equivalence or discontinuity factors are then adopted when using these data at the core level. Here, we studied the impact of the homogenization of the water holes of the heavy reflector. This impact should certainly appear in models where no equivalence is done. Similarly, we analyzed the discrepancies introduced when the radial curvilinear geometry of the reflector is deformed into a Cartesian one. We also used the more refined self-shielding technique of APOLLO3[®], in order to obtain the best estimate results. Investigations have been carried out on PWR configuration (KAIST core) before applying to VVER ones.
3. Finally, we developed an enhanced version of the Linear Surface (LS) method already present in APOLLO2 or APOLLO3[®] codes [15]. The goal of the new method is to allow using coarser computational meshes and therefore improve the computational time. In this note, we describe some results that are nevertheless limited to transport (i.e., they do not include any acceleration). Therefore, the method is not mature for industrial applications. The upgrading of the acceleration

is ongoing, and we hope we will be able to propose it as soon as possible. The work done to develop this item has been synthesized in the journal paper [16].

In Appendix A we describe the description of a Python library that permits the use of ALAMOS tools to describe coherently the full set of geometries needed for lattice calculations in a full-core study, as the one done here for the KAIST-like example in Paragraph 5. In our study, in fact, we “mixed” the native APOLLO3[®] geometries with the external ones of ALAMOS, but in future industrial applications the use of full external tool for geometry preparation may be investigated. The work presented here is a first step for this analysis.

In Appendix B we relegate the set of figures that describe the spatial error distribution in the different axial layers of the 3D calculation presented in Section 2.

2 Basic 3D transport methods and computational issues treated in this deliverable

In Task 4.4 we developed new methods for advanced treatment of some specific modeling problems in reactor physics. The numerical technique used for these investigations concerns the method of characteristics (MOC) implemented inside the TDT solver of the APOLLO3[®] code. In this paragraph, we detail the main improvements introduced in this solver inside the CAMIVVER project.

The traditional implementation of MOC solvers is in 2D calculations, which are routinely used in lattice calculations for multi-parameter library production. In CAMIVVER, we retrieved a previous version of the code [3],[4] where a 3D MOC was implemented, and we extended it to treat depletion problems with a polynomial expansion of cross sections (or, equivalently, of nuclide densities). To comply with typical nuclear reactor geometries, which are extruded, this polynomial expansion is limited to the axial direction. The main application case of this method concerns the axial reflector, where a strong thermal flux peak exists that is generally completely neglected in lattice calculations, or roughly modeled with approximate mono-dimensional schemes.

While burnup increases, the spatial flux gradients provoke the appearance of similar variations in nuclide densities and therefore of macroscopic cross sections. The typical approximation of all transport codes available nowadays to the best of our knowledge, is to approximate the cross section spatial variation as a step-wise constant (i.e., a different constant value in each volume of the domain both radially and axially). This of course undermines the approach of considering higher order expansion for the neutron flux, since one can expect that (for sufficiently high burnups) the same spatial variation of fluxes characterizes macroscopic cross sections. Using higher order approximations for the former (flux) is ineffective without extending it to the latter (cross-sections and concentrations, at least for full depleted systems). The extension of the MOC 3D flux expansion to the cross sections has been done in [5] and we resume here the approach and results. We refer to this last reference for more details. An independent application of this approach to the future experimental high flux CEA reactor “Jules Horowitz” can be found in [6] , from which we have largely taken the theoretical presentation of the 3D MOC.

2.1 The polynomial expansion

For a given energy group, we can consider the angular moments $\vec{\Phi}(\vec{r}) = \{\Phi_n(\vec{r}), n = 1, N_m\}$, related to an expansion of order K of the angular flux $\psi(\vec{r}, \vec{\Omega})$ in terms of real spherical harmonics $\vec{A}(\vec{\Omega})$ [7], where $N_m = (K + 1)^2$ and the effective macroscopic cross section $\Sigma_\rho(\vec{r})$ written here for an arbitrary reaction ρ . Note that the previous spatial functions can be written with the help of a polynomial expansion over a base of order N_p so that at the interior of each computational region r , we can write these functions as:

$$\Phi_n(\vec{r}) = \vec{P}(\vec{r}) \cdot \vec{\Phi}_{n,r} \quad \text{and} \quad \Sigma_\rho(\vec{r}) = \vec{P}(\vec{r}) \cdot \vec{\Sigma}_{\rho,r},$$

2.1

$\vec{P}(\vec{r})$ being the polynomial base given by

$$\vec{P}(\vec{r}) = \{(\tilde{z}_r)^p, p = 0, N_p\}, \quad \tilde{z}_r = \frac{z_r - \bar{z}_r}{\Delta z_r/2}.$$

2.2

In the previous formulas, z_r , \bar{z}_r et Δz_r are, respectively, the axial coordinate, the value at the mid height of the “r-th” computational region and the axial width of this same region.

2.2 Free transport iterations

Take into consideration a chord of the basic tracking set. Here a chord is the intersection of a characteristics line with the boundaries identifying a computational region. Let define l as being the length and supposed to be parallel to $\vec{\Omega}$, where \vec{r}^- and $\vec{r}^+ = \vec{r}^- + l\vec{\Omega}$ are the entering and exiting positions, respectively. The exiting angular flux, ψ^+ is given by the following relation:

$$\psi^+ = e^{-\tau(l)}\psi^- + \vec{P}^{2N_p}(\vec{r}^-) \cdot \vec{T},$$

2.3

where the index « $2N_p$ » means that the vector T contains supplementary terms with respect to Eq 2.2 until the order $2N_p$, and

$$\vec{T} = \{T_k, k = 0, 2N_p\}, \quad T_k = \sum_{p=k}^{2N_p} \binom{p}{k} \left(\frac{2\mu}{\Delta z_r}\right)^{p-k} q_{r,p}(\vec{\Omega}) E_{p-k},$$

2.4

μ being the polar cosine of the direction $\vec{\Omega}$ and $\binom{p}{k}$ is the binomial coefficient. Eq. 2.3 is obtained from the integral formulation of the transport equation for the stationary one group situation. In Eq. 2.4 $\tau(s)$ is the optical length between \vec{r}^- and $\vec{r}^- + s\vec{\Omega}$ along the chord, the “transmission coefficient” T_k is expression of polynomial coefficient of order p , $q_{r,p}(\vec{\Omega})$, (which appears in the polynomial expansion of the emission density analogous to those of Eq. 2.2 for the one group angular for the angular emission density), and the integral term $E_{p-k} = \int_0^\tau dz z^{p-k} e^{-(\tau-z)}$. Inserting the macroscopic cross section polynomial expansions

into the expression of the optical length (which is the integral of the macroscopic cross section along the chord) we can write:

$$\tau(s) = \sum_{j=0}^{N_p} \Lambda_j s^{j+1}, \quad \Lambda_j = \sum_{i=0}^{N_p-j} \lambda_{ij}, \quad \lambda_{ij} = P_i(\vec{r}^-) \Sigma_{T,r,i+j} \left(\frac{2\mu}{\Delta z_r} \right)^j \frac{1}{j+1} \binom{i+j}{i}, \quad 2.5$$

where $\Sigma_{T,r,i+j}$ is the coefficient of the polynomial order $i + j$, for region r , of the total macroscopic cross section

As for the coefficients of the emission density, their expression includes the polynomial coefficients of the flux angular fluxes and of the cross sections (of each group) (Eq. 2.1):

$$q_{r,p}(\vec{\Omega}) = q_{r,p}^g(\vec{\Omega}) = \sum_{n=1}^{N_m} A_n(\vec{\Omega}) \sum_{g'} \sum_{j+k=p} \Sigma_{S,n,r,j}^{g' \rightarrow g} \Phi_{n,r,k}^{g'} + \frac{1}{k_{\text{eff}}} \sum_i \chi_i^g \sum_{g'} \sum_{j+k=p} \nu \Sigma_{F,i,r,j}^{g'} \Phi_{1,r,k}^{g'}. \quad 2.6$$

$\sum_{g'}$, \sum_i and $\sum_{j+k=p}$ express, respectively, the summation over the energy groups, over the number of fissile isotopes and over the polynomial components of order j of the cross sections and k of the flux, with the constraint that their sum has to be equal to p . $\Sigma_{S,n,r,j}^{g' \rightarrow g}$ is the scattering cross section coefficient of spatial order j of $\Sigma_{S,n}^{g' \rightarrow g}(\vec{r})$, which is at its turn the coefficient corresponding to the n -th angular moment of the transfer macroscopic cross section from group g' to group g (classically developed in Legendre polynomials). In the same way, $\nu \Sigma_{F,i,r,j}^{g'}$ is the spatial coefficient in the development of the number of neutrons produced by fission for the isotope i per unit volume produced by neutrons with incident group g' . χ_i^g is the spectrum emitted in group g by the fission of isotope i and k_{eff} is the effective multiplication factor.

Finally, the term E_{p-k} of Eq. 2.4 is given by the relation:

$$E_{p-k} = \int_0^l ds s^{p-k} e^{\tau(s)-\tau(l)}, \quad 2.7$$

which, due to the polynomial expression of the optical path, cannot be integrated in closed form. The calculation of this integral is therefore done by a quadrature Gauss formula of an adaptive type, which uses for each chord and group a suitable order, that is determined computing a suite of integrals with an increasing order until the numerical value converges (the error is estimated by the difference between two successive values). As an option the user can use the same order to compute all values for all regions and energy groups.

2.3 Balance equation

In order to update, for each region r and each energy group, the spatial coefficients of the angular moment of the flux are used

$$\vec{\Phi}_r = \{ \Phi_{n,r,p}, n = 1, N_m, p = 0, N_p \}.$$

2.8

These coefficients are retrieved solving the balance equation. With this equation we are able to close the system (with the transmission equation 2.3). From now on we will use the bold characters for vectors and matrices that will contain all spatial and angular components. Moreover, we will adopt the traditional numbering of angular moments with the anisotropy order l and the corresponding index m to enumerate the harmonics related to the same anisotropy order. The vector $\vec{A}(\vec{\Omega})$ of the real spherical harmonics will then be denoted as:

$$\vec{A}(\vec{\Omega}) = \{ \{ A_l^m(\vec{\Omega}), m = -l, l \}, l = 0, K \}$$

2.9

and this numbering is also adopted for the vector $\vec{\Phi}(\vec{r})$ of angular moments. Starting from the stationary integro-differential one group transport equation and projecting on the angular and spatial base defined by the product of spherical harmonics and spatial monomials, it is possible to obtain the following system of equations for each one of the $2K + 1$ admissible values of the index:

$$\Gamma_r^m \vec{\Phi}_r^m = \vec{Q}_r^m - \vec{\Delta}_r^m.$$

2.10

The vector terms are equal to:

$$\begin{aligned} \vec{\Phi}_r^m &= \{ \vec{\Phi}_{l,r}^m, l = |m|, K \} \\ \vec{Q}_r^m &= \{ (\mathcal{Z}_r \vec{q}_r)_l^m, l = |m|, K \} \\ \vec{\Delta}_r^m &= \{ \vec{\Delta}_{l,r}^m, l = |m|, K \} \end{aligned}$$

2.11

and the matrix Γ_r^m will be described in the following, as well as the components of the vector $(\mathcal{Z}_r \vec{q}_r)_l^m$ and $\vec{\Delta}_{l,r}^m$. Since each of these last elements contains $N_p + 1$ components one, the vectors of Eq. 2.11 will be formed by $(K - |m| + 1)(N_p + 1)$ elements. This implies that the dimensions of the system 2.10 vary in function of m .

2.3.1 Description of the term $(\mathcal{Z}_r \vec{q}_r)_l^m$

In this product, \vec{q}_r is the vector of $N_m(2N_p + 1)$ spatio-angular components of the emission density, such that

$$\begin{aligned}\vec{q}_r &= \left\{ \left\{ \oint \frac{d\vec{\Omega}}{4\pi} A_n(\vec{\Omega}) q_{r,p}(\vec{\Omega}), p = 0, 2N_p \right\}, n = 1, N_m \right\} \\ &= \left\{ \left\{ \left\{ \oint \frac{d\vec{\Omega}}{4\pi} A_l^m(\vec{\Omega}) q_{r,p}(\vec{\Omega}), p = 0, 2N_p \right\}, m = -l, l \right\}, l = 0, K \right\},\end{aligned}\tag{2.12}$$

and \mathcal{Z}_r is the following matrix:

$$\mathcal{Z}_r = \oint \frac{d\vec{\Omega}}{4\pi} \vec{Z}_r(\vec{\Omega}) \otimes \vec{Z}_r^{2N_p}(\vec{\Omega}).\tag{2.13}$$

The vector $\vec{Z}_r(\vec{\Omega})$ and $\vec{Z}_r^{2N_p}(\vec{\Omega})$ are defined as

$$\begin{aligned}\vec{Z}_r(\vec{\Omega}) &= \{A_n(\vec{\Omega}) \vec{P}_r(\vec{\Omega}), n = 1, N_m\} \\ \vec{Z}_r^{2N_p}(\vec{\Omega}) &= \{A_n(\vec{\Omega}) \vec{P}_r^{2N_p}(\vec{\Omega}), n = 1, N_m\},\end{aligned}\tag{2.14}$$

where, $\vec{P}_r(\vec{\Omega})$ and $\vec{P}_r^{2N_p}(\vec{\Omega})$ are the vectors described by Eq. 2.2, and their product $\vec{P}_r(\vec{\Omega}) \otimes \vec{P}_r^{2N_p}(\vec{\Omega})$, gives a numerical version of the mass matrix $\mathcal{P}^{2N_p} = \frac{1}{V_r} \int_r d\vec{r} \vec{P}(\vec{r}) \otimes \vec{P}^{2N_p}(\vec{r})$, V_r being the volume of the region r . The use of the numerical version of this operator instead of the analytical one is required for the stability of the iterations, as explained in [4].

2.3.2 Description of the term $\vec{\Delta}_{l,r}^m$

This second term is obtained applying the projection $\oint \frac{d\vec{\Omega}}{4\pi} A_l^m(\vec{\Omega}) *$ to the following streaming term:

$$\Delta \vec{J}_r(\vec{\Omega}) = \frac{\Delta_{\perp}(\vec{\Omega})}{V_r} \sum_{\substack{t \parallel \vec{\Omega} \\ t \in r}} [\vec{P}(\vec{r}_t^+) \psi_t^+(\vec{\Omega}) - \vec{P}(\vec{r}_t^-) \psi_t^-(\vec{\Omega})],\tag{2.15}$$

where $\Delta_{\perp}(\vec{\Omega})$ is the surface of the transversal area associated to the characteristics lines parallels to $\vec{\Omega}$ and the sum is done over all chords parallel to $\vec{\Omega}$ and intersecting r . The term $\Delta \vec{J}_r(\vec{\Omega})$ is cumulated during the transport sweep of trajectories applying the transmission Equation 2.3.

2.3.3 Description of Γ_r^m

Γ_r^m is a square matrix that can be defined by block. To this effect, it is necessary to introduce the two following matrices:

$$\begin{aligned} \mathcal{G}_r &= \{\mathcal{G}_{r,pi}, p = 0, N_p, i = 0, N_p\}, & \mathcal{G}_{r,pi} &= \sum_{k=0}^{N_p} \Sigma_{T,r,k} \mathcal{P}_{(p+k)i} \\ \mathcal{H}_r &= \{\mathcal{H}_{r,pi}, p = 0, N_p, i = 0, N_p\}, & \mathcal{H}_{r,pi} &= -\frac{2p}{\Delta z_r} \mathcal{P}_{(p-1)i}, \end{aligned} \tag{2.16}$$

where $\mathcal{P} = (\mathcal{P}^{2N_p})^T$. Finally, if we define b_R and b_C as being the indices of the bloc of lines and columns respectively, we can then define each of the $(K - |m| + 1)^2$ blocs of Γ_r^m as

$$(\Gamma_r^m)_{b_R b_C} = \begin{cases} \mathcal{G}_r & b_R = b_C \\ \alpha_{|m|+b_R}^m \mathcal{H}_r & b_R = b_C - 1 \\ \beta_{|m|+b_C-1}^m \mathcal{H}_r & b_R = b_C + 1 \\ 0 & \text{otherwise} \end{cases} \tag{2.17}$$

where α and β are given by:

$$\alpha_{l+1}^m = \frac{\sqrt{(l+m+1)(l-m+1)}}{2l+1} \quad \text{and} \quad \beta_{l-1}^m = \begin{cases} \frac{\sqrt{(l+m)(l-m)}}{2l+1} & |m| \leq l-1 \\ 0 & |m| > l-1 \end{cases} \tag{2.18}$$

2.4 Acceleration of free iterations

In the TDT-MOC solver of APOLLO2 and APOLLO3® the slow convergence of the free transport iterations (both mono energetic and fission) is accelerated with the DP_N [9] method, which has been recently adapted to 3D extruded geometries [8] and to the higher order flux and cross section descriptions [4],[5]. In particular, the extension to the higher order cross section was developed during the CAMIVVER project. The principle of this approach is to solve a problem for the error of the estimated solution at a given iteration but with simplified hypotheses (lower anisotropy order and lower spatio-angular flux development) so as to deal with a faster problem. The solution of this problem is then used to correct the last MOC iteration flux, both at the internal level and to the external fission one [5], thus speeding up the global convergence of the iterative algorithm. To define this low order operator, we mimic the transport approach and define the two following transport and balance equations in terms of low order polynomial expansion coefficients of fluxes and cross sections:

$$\text{Transmission} \quad \vec{j}^+ = \mathcal{T}^* \vec{j}^- + \varepsilon^* \vec{q}_V^{\text{ext}}$$

$$\text{Balance} \quad \vec{\Phi}_{V,r} = \tilde{\mathcal{C}}_r \vec{q}_{V,r}^{\text{ext}} + \sum_{\beta \in \partial r} I_\beta \vec{J}_\beta \quad \forall r. \quad 2.19$$

The first relation is a system implying the set of currents (that here are the polynomial components of surface fluxes) over all interfaces between regions: the exiting vector is expressed in function of the entering one and of the external emission densities including transfer from other groups and fission. Once the “currents” are found, their values are substituted back into Eq. 2.20 and this allows to retrieve fluxes and so to accelerate convergence.

A more detailed explication as well as a description of the set of coefficients (\mathcal{T}^* , \mathcal{E}^* , $\tilde{\mathcal{C}}_r$ et I_β), is given in [5] **Erreur ! Source du renvoi introuvable.**, which constitutes the main CAMIVVER contribution to the development of the 3D polynomial solver.

2.5 Depletion coupling

The main goal pursued in the 3D lattice calculations of APOLLO3[®] was to perform reference calculations for depletion. Since the main APOLLO3[®] functionalities suppose a representation of cross sections which is step-wise constant, we defined a coupling strategy with the depletion library of the MENDEL code [14] and the self-shielding component based on the possibility of interpolating two different fluxes that are supposed to be coherent with a polynomial and a step-wise constant flux (and cross section) representation. We suppose therefore that the APOLLO3[®] user has produced two such geometrical and material representations and it is up to the solver itself to interpolate the « step-wise » coherent representation at entry onto the polynomial flux, and then use the polynomial flux solution at exit to make a projection onto the step-wise mesh. In this framework, the entering interpolation phase has to include the treatment of the cross section. An important remark is that both depletion and self-shielding phases are based on “intensive” quantities. This means that the self-shielding and the depletion operator do not need to compute the flux integral volume but treat simply punctual quantities. This permits us to define the mesh for self-shielding and depletion as a “Gaussian” mesh, with computational points located in the privileged points of the well-known Gaussian quadrature formula (see [5] for details). This permits us to interpolate in an optimal way the entering flux onto the polynomial mesh for MOC calculation. Typically, we use a Gauss-Legendre formula of order 5 for the depletion and self-shielding calculations. Calling Φ_i the generic spatial moment in region i of the flux mesh, the flux over the self-shielding/depletion mesh is given by:

$$\Phi_i = \vec{P}(\tilde{z} = x_i) \cdot \vec{\Phi}_r = \Phi_{r,0} + x_i \Phi_{r,1} + x_i^2 \Phi_{r,2} + \dots + x_i^{N_p} \Phi_{r,N_p}, \quad 2.20$$

where x_i is the abscissa of the Gauss-Legendre mesh to which i belongs and $\vec{\Phi}_r$ is the vector moments to which r belongs, in the flux mesh to which i is associated. The flux computed on the Gaussian mesh will then be transferred to the depletion (resp. self-shielding) operators to update nuclide concentrations (resp. micro cross sections).

In the same manner at the beginning of the flux calculation, it is necessary to obtain the spatial component of the cross section, starting from the constant and self-shielded values

stored at the Gaussian points of the mesh. The polynomial coefficients $\vec{\Sigma}'_r$ for an arbitrary reaction in region r are obtained by preserving the moments $\vec{\Sigma}'_r = \{\Sigma'_{r,p}, p = 0, N_p\}$ starting from the N_G stored in the mesh $\{\Sigma_i, i = 1, N_G\}$, as follows :

$$\Sigma'_{r,p} = \frac{1}{V_r} \int_{V_r} d\vec{r} P_p(\vec{r}) \Sigma(\vec{r}) = \frac{1}{2} \int_{-1}^1 d\tilde{z} (\tilde{z})^p \Sigma(\tilde{z}) = \frac{1}{2} \sum_{i=1}^5 w_i (x_i)^p \Sigma_i$$

$$\vec{\Sigma}_r = \mathcal{P}_{\text{Sq}} \vec{\Sigma}'_r,$$

2.21

where w_i is the Gauss-Legendre weight associated to the i -th abscissa and \mathcal{P}_{Sq} is the square matrix associated to the minor of order $N_p + 1$ of \mathcal{P} . Since the evaluation of the moments needs to integrate the polynomials until the order $2N_p$ and that a Gauss quadrature of order m integrates exactly polynomials up to order $2m - 1$, it follows that $2m - 1 \geq 2N_p \Rightarrow m > N_p$. Hence, adopting for our calculations a quadrature of order 5, it is possible to expand exactly the effective cross sections until order 2. In Fig. 2.1, it is described schematically the interpolation and projection way between cross section (at enter) and fluxes (at exit) of each calculation along depletion.

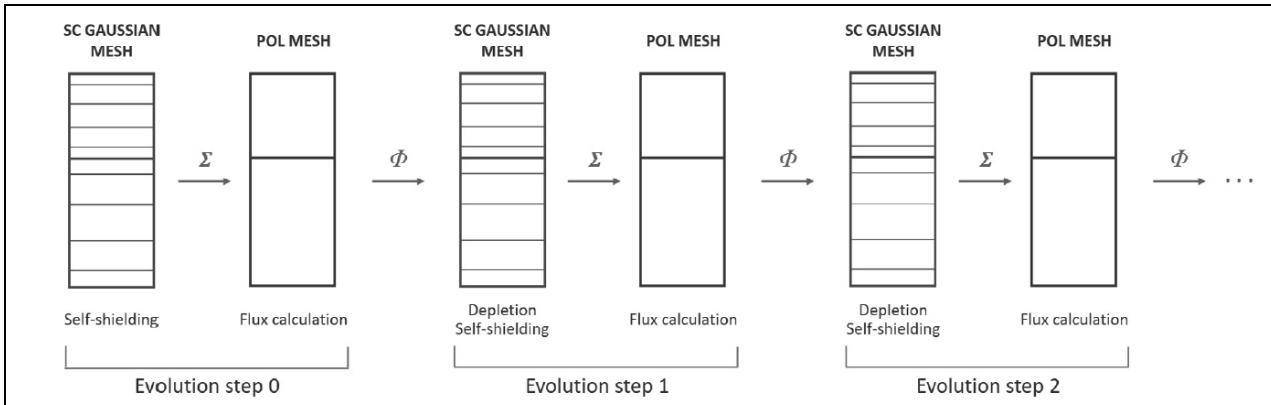


Figure 2.1: Coupling of cross sections and nuclide concentrations along depletion (from [5]).

2.5.1 3D case description and benchmarking

In the following Figs 2.2 and 2.3, we describe the radial and vertical layouts of the computational case we considered in our study. The case is a typical 17 by 17 UOX 3D assembly including the axial reflector. This last is modeled here by smearing its homogenously structure material into the moderator as it is typical done in Monte Carlo calculations for industrial benchmarks. The detailed geometrical description of the case can be found in [5]. To perform our reference Monte Carlo calculations, we used TRIPOLI-4[®] [22] and the Triage function of APOLLO3[®] to translate all APOLLO3[®] data into TRIPOLI-4[®] ones (e.g., geometry, material composition and temperatures, reaction rates to be scored). In the following Tables 2.1 and 2.2, we can find the main computational options adopted for the TRIPOLI-4[®] and APOLLO3[®] calculations.

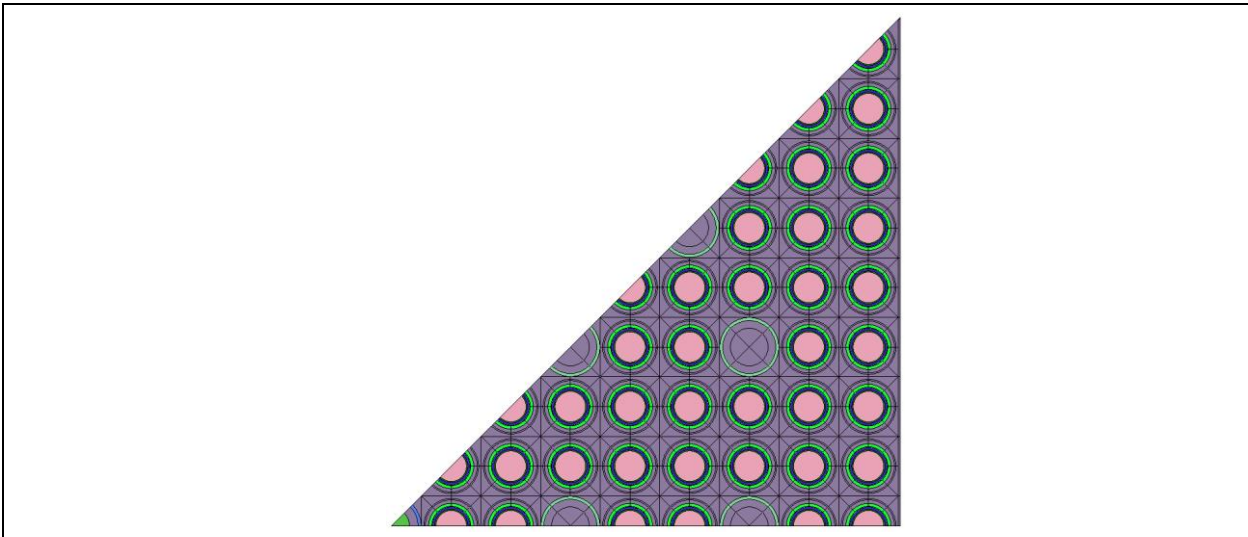


Figure 2.2: X-Y layout of the 3D assembly calculation.

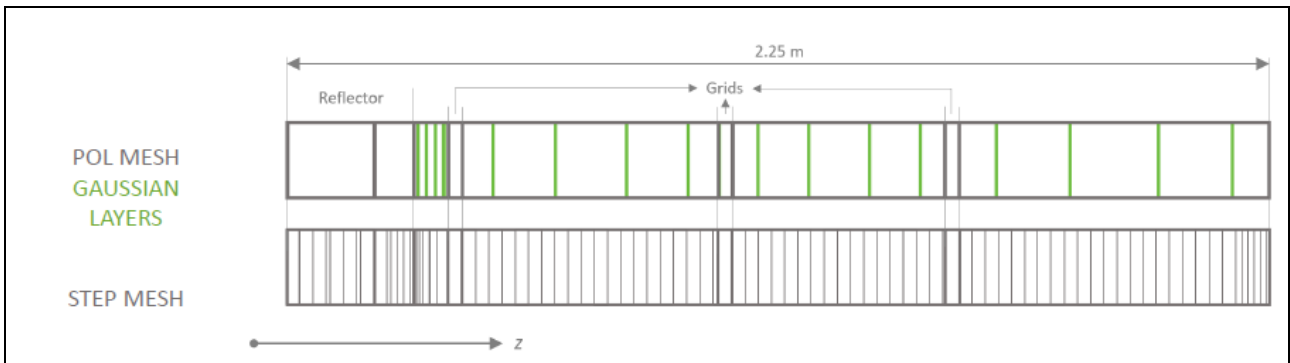


Figure 2.3: Axial (i.e., along Z) layout of the 3D assembly calculation.

To interpret the results (that we mostly relegated in Appendix B) it is important to note that the material meshes along the z axis are in number of 9 (see Fig. 2.3). The first two meshes correspond to the axial reflector. The third one is for the first active region at the interface with the reflector. The fourth one describes the first grid zone. And then we find alternatively active zones followed by grid zones until the last ninth layer, which ends on the axial plane of symmetry.

These calculations have been carried out using the AP3-2.3.r18530 revision of the APOLLO3[®] code and the 4.11.1 version of the Monte Carlo TRIPOLI-4[®] code.

Table 2.1 - Main calculation options adopted with the polynomial 3D MOC solver of APOLLO3[®].

AP3-XPOL	
Energy mesh	SHEM-281
Anisotropy	P3
SSH methods	Fine Structure (Pij exact) + Livolant-Jeanpierre for mixtures
Upscattering	No
Nuclear Data	JEFF3.1.1
Polar angles (0, π)	4

Azimuthal angles ($0, \frac{\pi}{2}$)	24
Order of the spatial polynomial development	2

Table 2.2 - Main calculation options adopted with TRIPOLI-4®.

TRIPOLI-4®	
Number batches	150000 (+200 discarded)
Batches size	20000
Doppler broadening method	SVT with $E_{threshold} = 4.95 \text{ eV}$
Nuclear Data	JEFF 3.1.1
TABPROB	Yes

2.5.2 Context for a correct comparison between Monte-Carlo and deterministic calculation along depletion

In order to compare correctly Monte-Carlo and deterministic calculations along depletion one must take into consideration that Monte-Carlo methods adopt a step-wise approximation for cross sections. This means that the Gaussian mesh adopted for the deterministic calculation to exchange with depletion and self-shielding is certainly too coarse to correctly capture the strong cross section gradients that appear especially at the interface with the axial reflector at high burnups [5]. We need therefore adding some supplementary axial layers to the Monte-Carlo simulation in order to be more accurate and have a fair comparison with APOLLO3®. We called this the “Step-Equivalent” Mesh (SEM), as it corresponds to the mesh one needs to adopt (even in deterministic calculations) to reproduce more accurately the cross section evolution along depletion with a step-wise axial approximation.

Derivation of an optimal “step-equivalent” mesh

In Fig. 2.4, we sketched the situation by plotting the total cross section along the z axis at a certain location on the 2D plane for a given energy group. This plot uses the polynomial functions used for the flux calculation¹. A step-wise approximation of the cross section can also be seen. The corresponding SEM mesh was derived by employing a Python script (developed during the CAMIVVER project) based on the following algorithm.

To correctly “follow” the spatial behavior of the polynomial total cross section (we considered the Σ_t gradients to be representative for the gradients of the other cross sections as well) in each 2D region and each energy group, we approximate it with a step-wise approximation that we require to match the reference at each interval within a given tolerance $\Delta\Sigma$. The resulting SEM meshes (one for each 2D region and energy group) are

¹ The coefficients of the polynomial expansion of the total cross sections are printed by APOLLO3® on text files and read with a Python script.

then merged to obtain a single mesh whose layers must be larger than a certain tolerance δz_{min} (i.e., while merging two SEM meshes, the algorithm checks that, the z-layer it is trying to insert, is sufficiently far from the neighboring ones, otherwise it rejects it and moves to the next). The final SEM mesh such derived is guaranteed to conserve the zero-th order moment of the reference polynomial total cross section but not its higher-order moments. Hence, *a posteriori* we verify that these moments are sufficiently accurate (i.e., within a tolerance $\Delta\zeta_p$). Otherwise, we reduce the tolerances $\Delta\Sigma$ and δz_{min} and restart the script.

The SEM mesh shown in Fig. 2.4 has 79 layers along z and it is the result of several iterations performed with the Python script to optimize its outcome, not only in terms of precision in the approximation of the higher order moments of the cross section, but also in terms of number of layers. In fact, the higher the number of z-layers in the z-mesh, the more expensive from the computational and memory points of view are the corresponding TRIPOLI-4[®] calculations. Hence, it was necessary to tune the tolerances $\Delta\Sigma$ and δz_{min} on each polynomial layer (i.e., the 3rd, the 5th, the 7th, and the 9th) independently, as reported in Table 2.3.

Table 2.3 – Parameters adopted in the Python script to derive the SEM mesh in Figure 2.4.

Parameter	Value
$\Delta\Sigma$ (%) (values in the [3 rd , 5 th , 7 th , 9 th] layer)	[3.8, 3.8, 3.5, 2.5]
δz_{min} (cm) (values in the [3 rd , 5 th , 7 th , 9 th] layer)	[0.38, 1.5, 2.0, 3.5]
$\Delta\zeta_1, \Delta\zeta_2$ (%)	[0.1, 0.1]

Once this SEM mesh is set up, we can use the APOLLO3[®] environment to produce a calculation where the previously described Gaussian mesh is substituted with this new SEM mesh. These new calculations are then used to produce the data (isotopic concentrations, etc.) suitable for the TRIPOLI-4[®] calculations that are to be compared with the “polynomial” calculations done with the Gaussian meshes. In principle, using “optimized” step-wise calculations instead of Gaussian ones is less precise. And in fact, we found that the two deterministic calculations (the Gaussian and the Step-optimized one) give different results starting from 10MWd/t and more strongly at the end of the cycle as the following Fig. 2.6 shows. This probably means that we need to squeeze our tolerances to allow them sticking. But for lack of time we did not pursue this in this work.

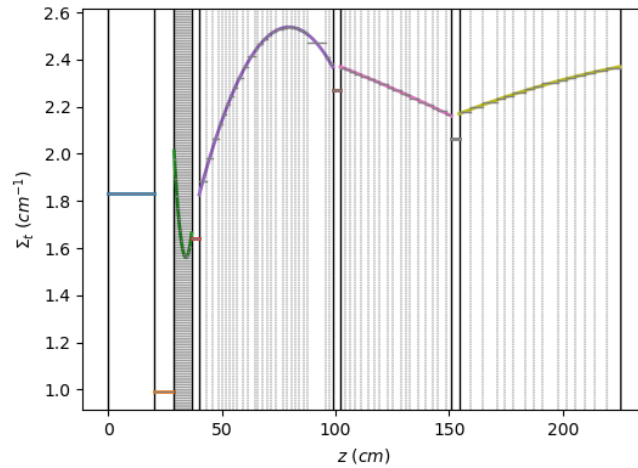


Figure 2.4: Example of the mesh generator outcome: each vertical line corresponds to an axial layer of the “step-equivalent” mesh.

2.5.3 Comparison of TRIPOLI-4[®] vs APOLLO-3[®] results

In Fig. 2.5 we give the error between the reference deterministic calculation done with the Gaussian mesh and the SEM computed by algorithm described in the previous sub-section.

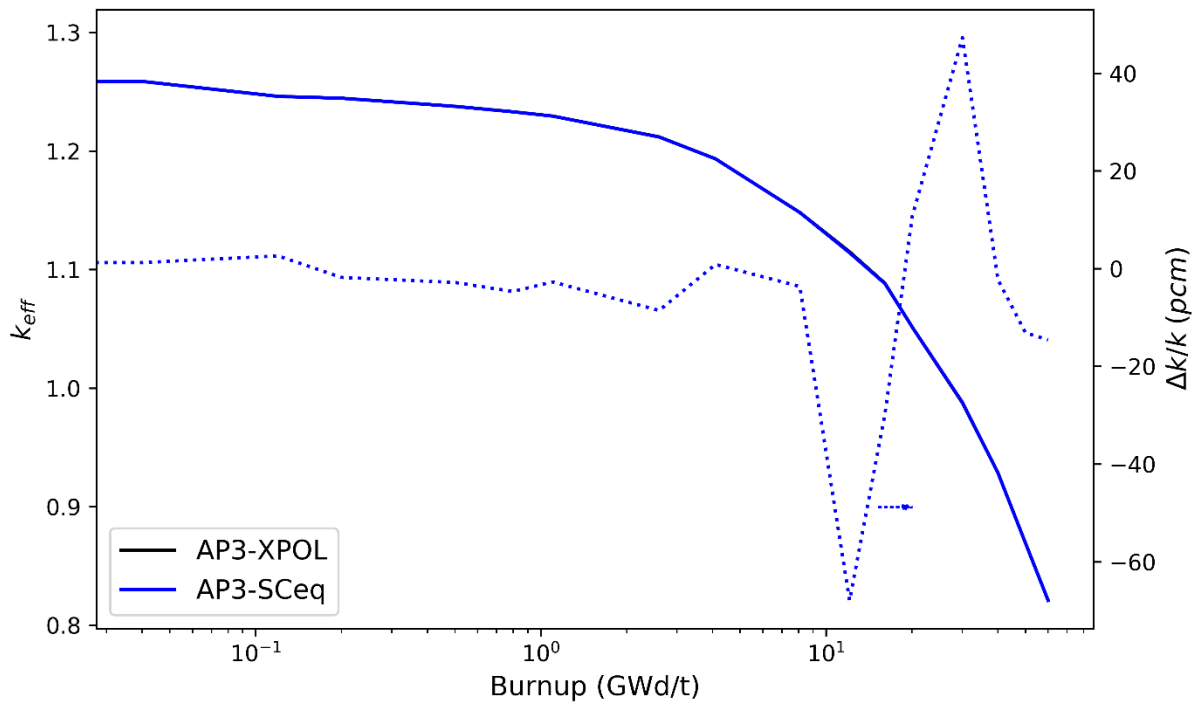


Figure 2.5: Reactivity swing along depletion computed with the reference deterministic method with Gaussian mesh, and the relative error with respect to the computed SEM derived with the strategy of sub-section 2.4.2.

The errors undergone with the SEM are quite low and we are well poised to use the SEM for further comparisons with TRIPOLI-4[®]. The following Fig. 2.6 depicts the obtained reactivity errors with respect to Monte Carlo calculations that have been produced with the SEM and with the concentrations extracted from the deterministic calculation at each depletion step. This figure shows that the deterministic reactivity is systematically

underestimated and that, apart from a maximum local error of about 230 pcm around 200MWd/t, there is drift in the error at the end of the cycle, conducting the maximum error to 340 pcm. As showed in [5], the gradients of the cross sections at the end of the cycle are very high. We can therefore suppose that our computational mesh is not fine enough (with an order of polynomial development of order 2) to give a correct result at the end of the cycle. We will address in next future further studies to improve this precision.

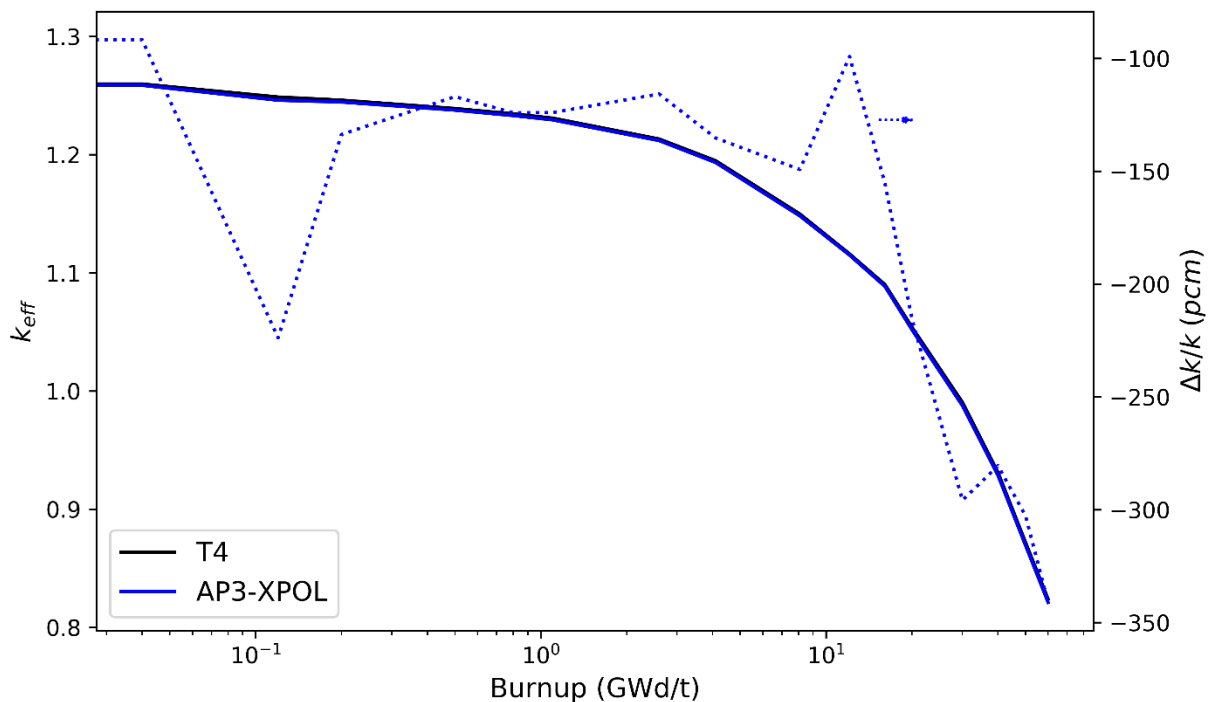


Figure 2.6: Reactivity swing along depletion computed with the reference deterministic method with Gaussian mesh, and the relative error with respect to the computed with TRIPOLI-4[®] calculations obtained with the concentration extracted onto the SEM obtained with the strategy of sub-section 2.4.2.

Before going on, we show in Figs. 2.7 and 2.8 the radially integrated reaction rates at 0 MWd/t, along each layer computed with the referential deterministic Gaussian method and its discrepancies with respect to the SEM calculation. It is apparent that our SEM is not completely converged from the spatial viewpoint and that a different converged mesh should probably reduce the following errors.

In Fig. 2.9, we plotted the radially integrated reaction rates at 0 MWd/t, along each layer. If results are good for most internal layers, a problem appears at the interface with the axial reflector where there is a relative maximal errors of 3%. This tendency is confirmed also in Appendix B with the analysis of pin-by-pin reaction rates errors. It is worth noting that in Ref. [5] a similar analysis was done but with lower errors. In that reference, a different mesh and different options were used in TRIPOLI-4[®] calculations, but the choice here should be a better one, and also an older version of APOLLO3[®] was used there. We need therefore more work to correctly interpret these discrepancies. Having said that, we believe that the present work is representative and interesting. It is in fact worth noting that, at the best of our knowledge, there is not any benchmark result for depletion calculation in literature. Even

customary Monte-Carlo calculations do not rigorously test the spatial convergence of the step-wise cross section approximation.

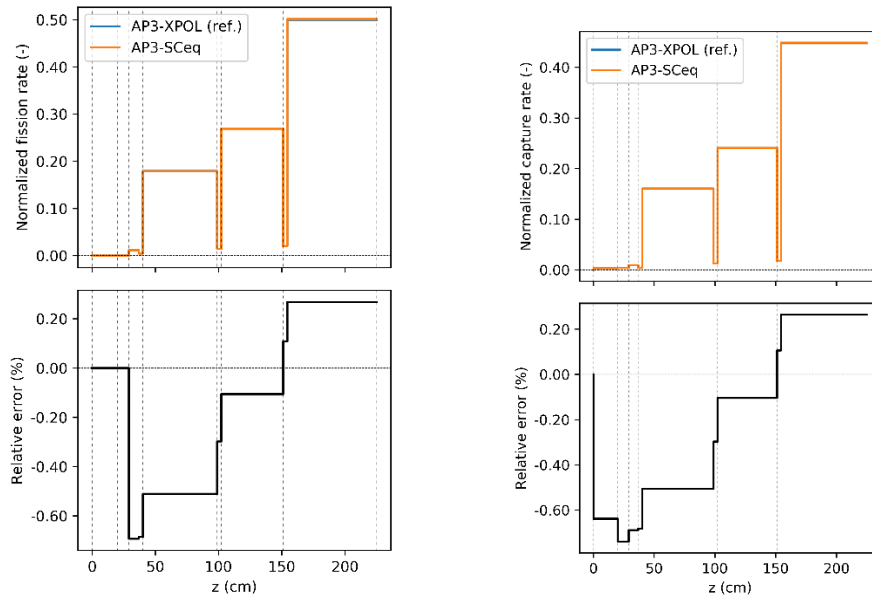


Figure 2.7: Radially integrated reaction rates (fission on the left, capture on the right) and discrepancies at 0 MWd/t between the reference deterministic calculation (with the Gaussian mesh) and the SEM one.

In Fig. 2.10, we plot a similar content of Fig. 2.9 but at the end of the cycle at 60 Gwd/t. Here, errors are a bit lower than at 0 MWd/t but of similar order. In Appendix B, the plot of the pin-by-pin reaction rates confirms this behavior.

As a general comment we can say that our higher order MOC method shows a good behavior during depletion, even if we still have some local errors (especially in the axial reflector) that have to be understood. Part of these errors certainly come from the self-shielding technique we have chosen. Another issue seems to be linked to the strong cross sections gradients present at the end of the cycle.

In conclusion of this section, we can say that during the CAMIVVER project we have adapted the higher 3D MOC scheme to take into account the spatial variation of nuclide concentrations and cross sections during depletion. We have also established a framework to undergo detailed comparisons for Monte-Carlo validation. Preliminary calculation have been done and encouraging results have been obtained. More work needs to be done to fully achieve this validation phases.

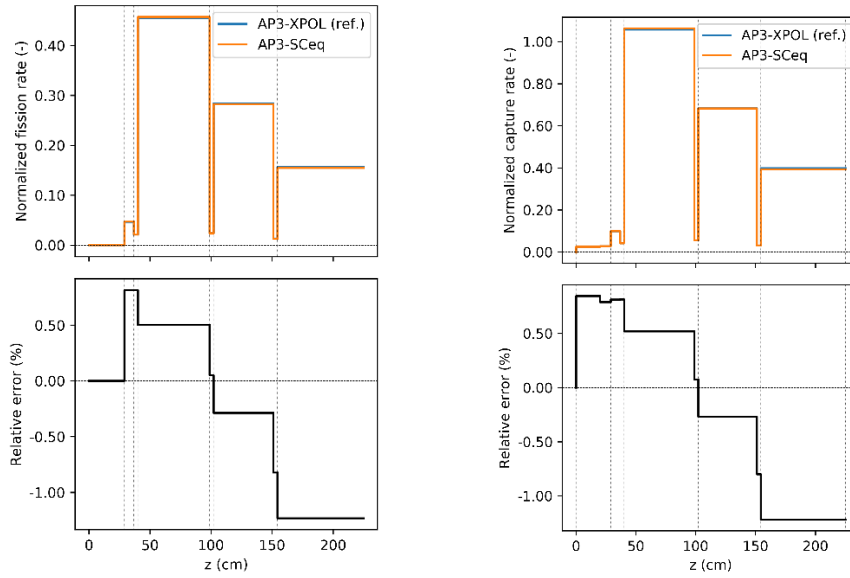


Figure 2.8: Radially integrated reaction rates (fission on the left, capture on the right) at 60 GWd/t between the reference deterministic calculation (with the Gaussian mesh) and the SEM one.

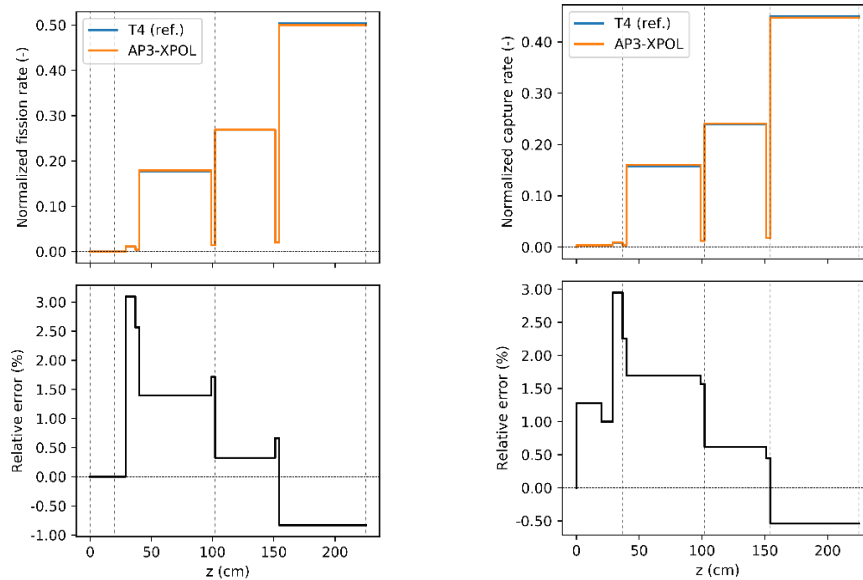


Figure 2.9: Radially integrated reaction rates at 0 MWd/t (fission on the left, capture on the right) and their respective relative errors with respect to Monte Carlo calculations.

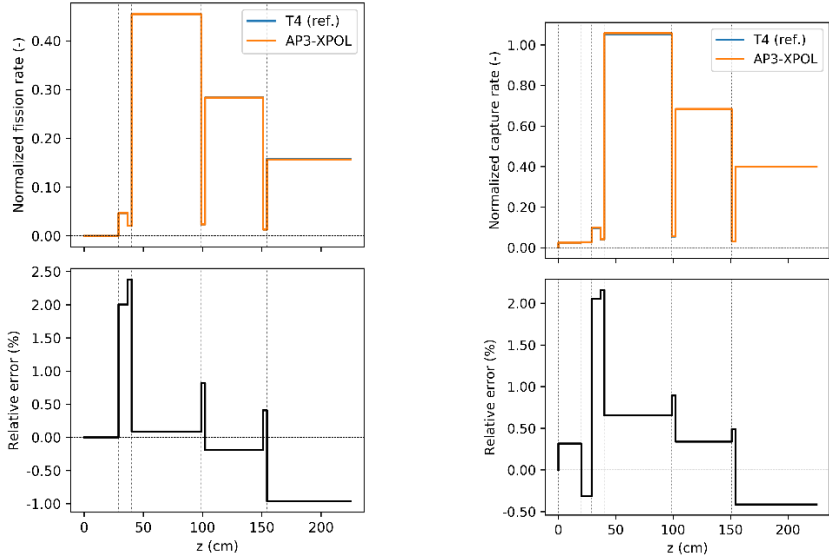


Figure 2.10: Radially integrated reaction rates at 60 GWd/t (fission on the left, capture on the right) and their respective relative errors with respect to Monte Carlo calculations.

3 Advanced reflector modeling with APOLLO3®

In this section, we discuss the work done in Task 4.4 for the improvement of the reflector modeling. To test our approaches, we used a modified version of the KAIST benchmark [12], that was defined specifically in task 4.4 in [13]. The main difference is in a curved heavy reflector instead of the original water Cartesian one, and introduced in it a set of water holes as well as the bypass, the barrel and the downcomer. This has the evident goal of being more in touch with the industrial context, being this reflector design conceptually similar to the one found in the EPR nuclear reactor or the SMR concepts under development. The detailed description of the reflector design adopted can be found in [13]. In Figs. 3.1 and Fig 3.2 we describe the general layout. The latter is simply a recall of the original benchmark [12] for what concerns the assembly location. In our calculations, the modeling was done by using native geometry capabilities of APOLLO3® to describe the assembly geometries, and the ALAMOS code [11] to model the reflector. In Appendix A, we show how the ALAMOS application can also be used to model the entire geometry of this test case. The reason why we did not use this last approach is because these capabilities were not available at the beginning of the project and they were developed to open the discussion for future industrial applications.

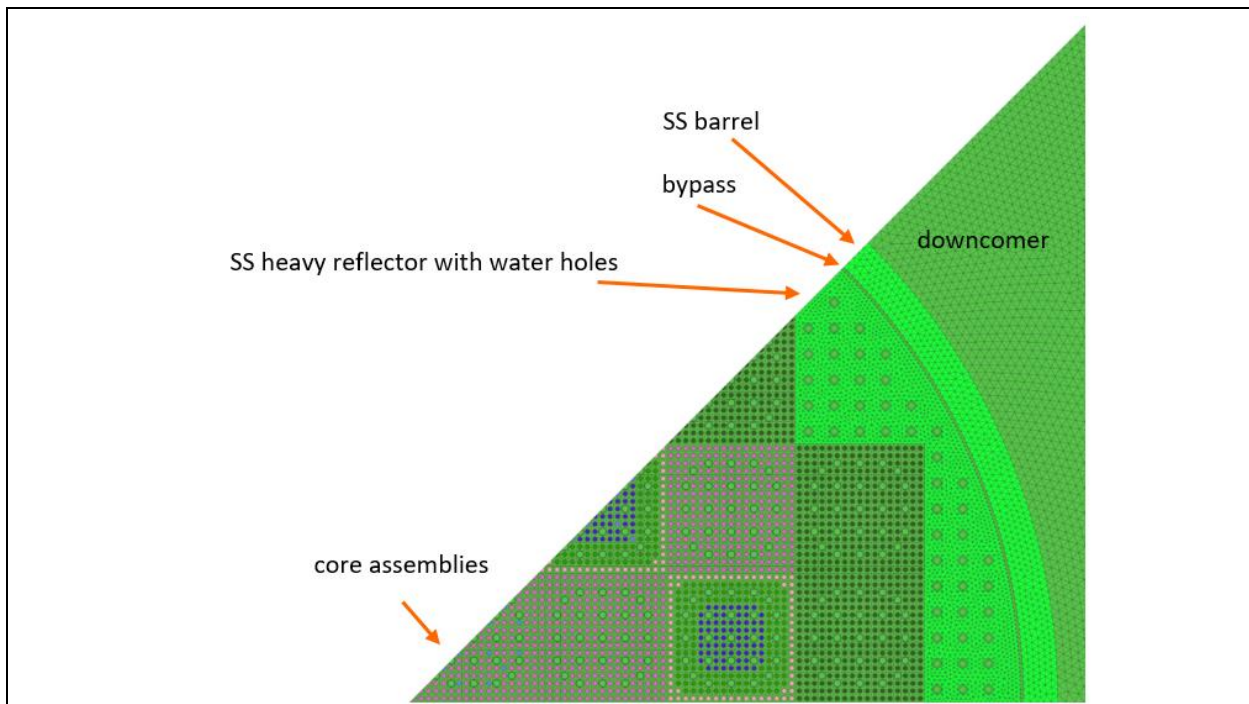


Figure 3.1: Modified KAIST CORE with heavy reflector generated with native plus ALAMOS geometries.

3.1 Geometrical and material description of the study cases

As depicted in Figs. 3.1 and 3.2 we took into consideration a quite heterogeneous core layout, including MOX assemblies. In the original benchmark, it was possible to substitute MOX assemblies with Control Rod ones. We did also run these calculations in 2D, but we did not fully benchmark them against Monte Carlo calculations. Hence, in this note we only present unrodded configurations.

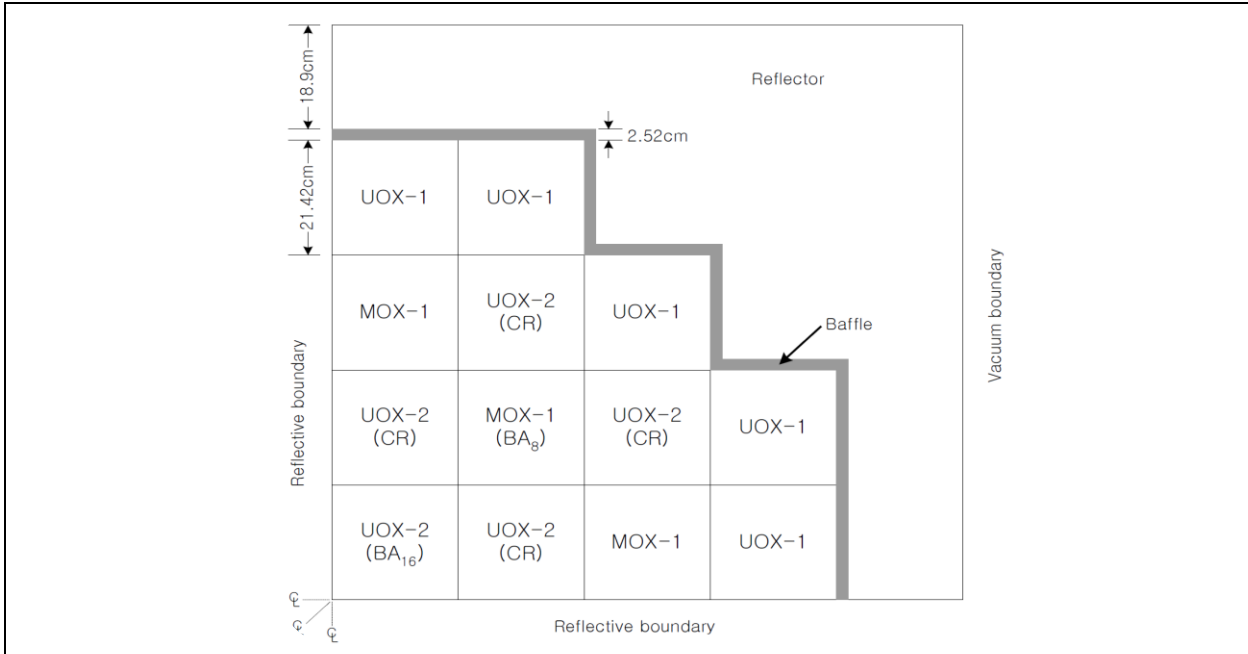


Figure 3.2: Assembly layout of KAIST CORE (from reference [12]).

In the following Tables 3.1 and 3.2, we reported the list of geometrical features concerning the core and the reflector layout, and in Table 3.3 the reactor operating conditions .

The pressure vessel is not represented in our calculations (because we are interested in analyzing perturbations in terms of k_{eff} and in-core reaction rates on which the explicit modeling of the vessel has no impact) and vacuum boundaries conditions are imposed outside the downcomer (i.e., at $x = x_{max}$).

Table 3.1: General reactor characteristics.

Cell pitch	1.26	cm
Assembly pitch	21,42	cm
Assemblies number	52	
Core length	171.36	cm
Reactor length	264.4672	cm
Water holes number (1/8 th)	48	

Table 3.2: Heavy reflector specifications.

	Material	inner radius (cm)	Thickness (cm)
baffle	stainless steel (SS-304)	85.68 (median)	16.036
waterhole	water (+ bore)	0.7	
bypass	water (+ bore)	101.716	0.5
barrel	stainless steel	102.216	5.715
downcomer	water (+ bore)	107.931	24.3026
outside	Void	132.2336 (median)	

Table 3.3: Reactor operating conditions.

Reactor power	900	MW _{th}
Fuel temperature	900	K
Cladding temperature	630	K
Moderator temperature	570	K
Water density	0.7295	g/cm ³
Boron concentration	800	ppm
Reflector temperature	570	K

The pressure vessel is not represented in our calculation and vacuum boundaries conditions are used outside the reflector.

3.2 Computational scheme and establishment of the reference deterministic result

In our deterministic calculations, we used the CEAV512 nuclear data library (based on the JEFF3.1.1 evaluation) with the 281 groups energy mesh SHEM [17]. Fuel self-shielding is performed by assembly in infinite space for uranium, plutonium, zirconium and gadolinium nuclides, using the prescribed option of Fine-Structure self-shielding method typical of APOLLO2/3[®] calculations.

The treatment of reflector self-shielding is based on a 1D slab with one UOX fuel assembly and a reflector slice for uranium, chrome, iron, nickel and manganese nuclides. In Fig. 3.3, the initial slab contains one slice of fuel assembly, one slice of stainless steel (2.52 cm with 7 meshes) and one slice of water (19 cm with 16 meshes). A more accurate slab was adopted to improve the reflector self-shielding model: alternating water and stainless steel according to the real geometry up to the downcomer (46.6 cm with 81 meshes). The last part of Fig. 3.3 describes the geometrical models for the self-shielding.

Self-shielding calculation uses the TDT-PIJ solver, with a transverse integration step of 0.05 cm and an angular quadrature formula of 24 uniform angle in $[0, 2\pi]$ and the mandatory anisotropy of P0 for collision probability methods.

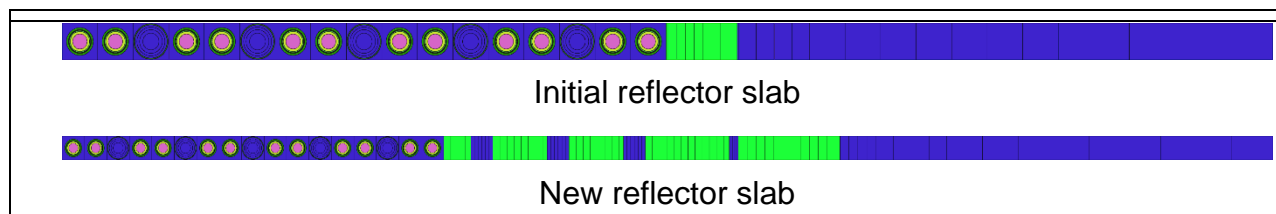


Figure 3.3: Initial and new reflector 1D model used for self-shielding calculations of the Kaist core.

In our calculations, we used an in-development version of the APOLLO3[®] code (rev xxx) as well as ALAMOS-v9.8.0. We compare results obtained in terms of 1 or 2 energy groups reaction rates with a pin by pin spatial resolution.

The reference TRIPOLI-4[®] calculation (input file computed through the Triage tool ²) was coherently set up to output cell-by-cell mono- and 2-groups total, capture and fission rates. We employed version 4.12 of the code and we simulated 200 000 batches with 25 000 neutrons/batch, on 36 parallel processes, discarding the first 200 batches per process before starting scoring. A square root temperature interpolation of nuclear data was adopted, as well as the SVT model for the Doppler broadening of elastic scattering.

As for the TDT-MOC solver, we tested the linear-surface (LS) characteristics method with DP1 acceleration (on a mesh with 37 323 regions and 105 076 surfaces) or the step characteristic method (SC) with the asymptotic synthetic accelerations DP1 with sector refinement (on a mesh with 195556 regions and 378459 surfaces). More details about these two options are given in the next paragraph where we discuss the LS-xy scheme. The MOC calculations of this paragraph were carried out with 360 discrete angles derived from a product quadrature formula constituted by 36 uniform angles in $[0, \pi]$ and 5 Bickley-Naylor polar angles in $[0, \frac{\pi}{2}]$. We adopted a transversal integration step of 0.02 cm and a maximum order of anisotropy for the scattering kernel equal to 3.

In the tables the reactivity error is calculated as follows: $\frac{k_{eff_{AP3}}}{k_{eff_{T4}}} - 1$. The reaction rates are energy integrated, pin by pin homogenization is used in the fuel assemblies but only one region is considered in the reflector. The TRIPOLI-4[®] reference solution presents a $k_{eff} = 1.13522$, with a statistical uncertainty $\sigma = 1.3$ pcm.

These calculations have been carried out using the AP3-2.3.r18432 revision of the APOLLO3[®] code, the 4.11.1 version of the Monte Carlo TRIPOLI-4[®] code and the 9.8 version of the ALAMOS tool.

Table 3.4: Reactivity, fission, capture and total reaction rates errors in one and two groups for the Kaist calculation in function of the two computational options SC or LS and the initial or new slab for reflector self-shielding.

APOLLO3 [®]		TDT-MOC-SC	TDT-MOC-LS	
			initial slab	new slab
Reactivity error (pcm)		-300	-220	-221
Fission rates error (%)	min	-2.71	-0.98	-0.97
	max	5.19	1.66	1.59
	RMS	1.30	0.41	0.40
Capture rates error (%)	min	-2.08	-0.89	-0.89
	max	3.16	1.65	1.58
	RMS	0.99	0.52	0.53
	reflector	7.37	3.60	3.31
Total rates error (%)	min	-1.05	-0.29	-0.28
	max	2.99	1.31	1.28
	RMS	0.71	0.25	0.24
	reflector	5.55	4.21	3.67

² APOLLO3[®] user manual associated to AP3-2.3 version.

In Table 3.4, we have a global sketch of the situation in terms of computational error between the deterministic and the stochastic calculation. We can remark that the LS scheme reduces the reactivity error of 80 pcm and the RMS errors on reaction rate of more than a factor 2. The maximum error per cell for LS is 1.6% in the active core part while is 5.1 % for the SC. This shows that the larger part of the fissile zones error is simply due to the lack of spatial convergence of the computational mesh, despite the fact the mesh adopted for calculations with the SC method was significantly more refined. For the reflector the maximum error is higher (3.6% for the capture rate in LS, and 7.3% for the SC). Using the refined slab model for the reflector SSH does not globally change the situation for the active core part, but slightly improves the results for the reflector, at least for the total rates.

Nevertheless, global errors in reflector remain quite important. Generally, people neglect the error in the reflector since in the industrial applications we are more interested in the response of the fissile zones. But looking at the following spatial distribution of the errors we find that the most important ones are located at the interface with the reflector (where the power remains generally low). The improvement of the reflector modeling could bring with itself a global improvement also of the fissile zone calculation. We believe therefore that the reduction of the global error in fissile zones under the level of the percent, could be obtained only after an improvement of the self-shielding model of the reflector part. Nevertheless, we can say that the errors obtained in this study are largely satisfying for industrial calculation and that this model can be used to benchmark depletion calculations, where the Monte-Carlo calculations are seldom affordable due their too important computational costs.

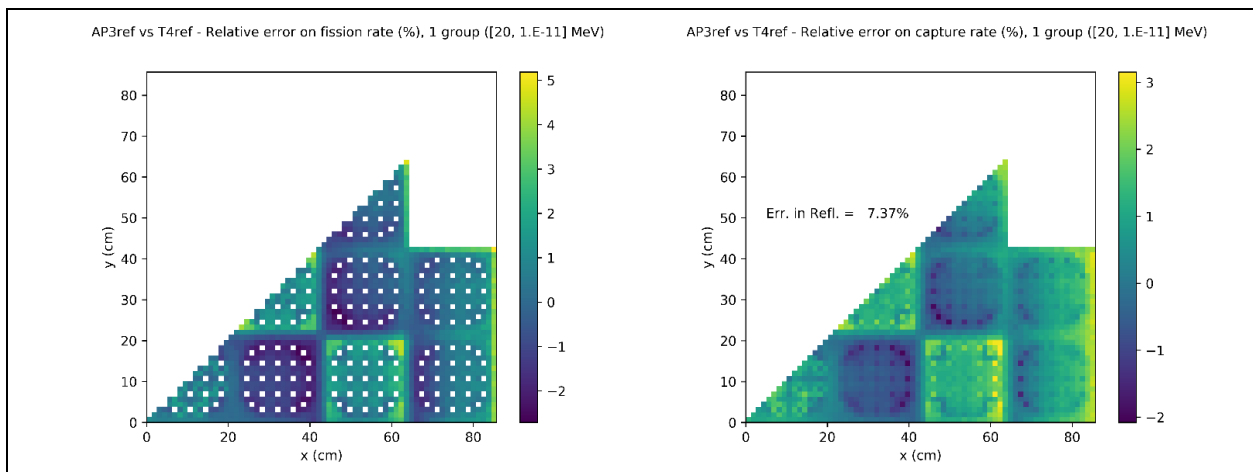


Figure 3.4: Spatial distributions of the fission and absorption reaction rates errors of the KAIST CORE against T4 results for the SC calculation.

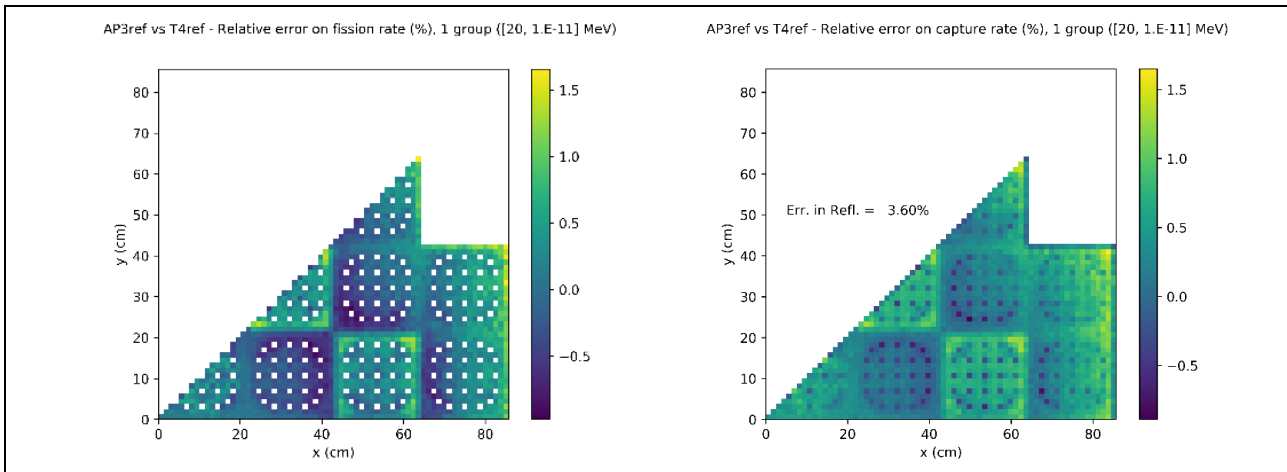


Figure 3.5: Spatial distributions of the fission and absorption reaction rates errors of the KAIST CORE against T4 results for the LS calculation with the new reflector slab.

In Figs. 3.4 and 3.5 we plotted the spatial distributions of the fission and capture reaction rate errors for, respectively, the SC and the LS calculations against the reference TRIPOLI-4[®] calculation (indicated with “T4”). For the LS scheme, the reflector was modeled with the new reflector slab. MOC-LS results are significantly better than MOC-SC results and the new slab modelling is slightly better than the initial slab. As it was expected the maximal errors are located at the interface between the reflector and the core. But, in the case of the LS calculation, the errors are quite tiny certainly permitting to use these calculations to benchmark depletion calculation of industrial schemes.

Before moving to the next section, we present some other results concerning the use of a SubGroup (SG) model for self-shielding. Since this method is only available with a 383-groups library, the following results were obtained by switching to a new nuclear data library available with JEFF-3.1.1 evaluation (CEAV512 nuclear data library).

Of course, it is then difficult to attribute the following improvements simply to the new method of self-shielding instead to the refined energy mesh. Unfortunately, it is not possible to use the FS method with the 383-groups energy mesh, nor the SG method with the SHEM library.

Table 3.5: Direct comparisons in reactivity and reaction rates error between the 383-groups cross section library with SG and the FS method with 281 SHEM library.

	$\Delta k/k$ (pcm)	MAX/MIN Fiss (%)	NRMS Fiss (%)	MAX/MIN Capt (%)	NRMS Capt (%)
MOC-LS FS	-220	+1.66/-0.98	0.41	+1.69/-0.83	0.52
MOC-LS SG	-71	+1.35/-0.90	0.41	+1.10/-0.82	0.32

Table 3.5 compares the FS and the SG LS calculations (with refined reflector model). We can see that we have an important reduction of the reactivity error and of the maximum error

in fission and capture. We have now maximum error only slightly greater than 1%. To complete the comparison, Fig. 3.5 shows the error spatial distribution. In Table 3.6 it can be found a more detailed information for the errors in reactions rates. Even if these results are of higher quality than those obtained with the SHEM MOC scheme, we pursued using this latter in the rest of this section, to maintain the computational costs at a reasonable level. In fact, we believe that previous results have already an acceptable level of precision and we preferred to have the possibility to run faster calculations to cover a larger portion of the possible field of investigation.

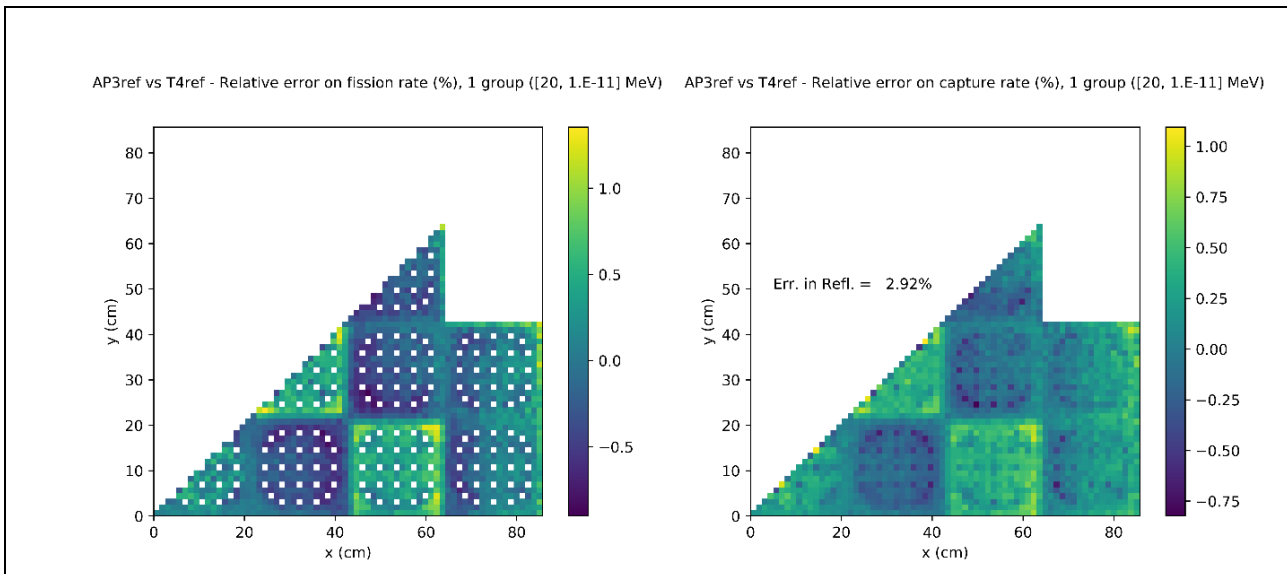


Figure 3.5: Spatial distributions of the fission and absorption reaction rates errors of the KAIST CORE against T4 results for the LS calculation with the new reflector slab and the SG self-shielding method.

3.2.1 Influence of a multi-zones self-shielding model

To improve the previous approaches in view of having a geometrical model that can be used in the core calculations, we inserted computational zones in the reflector by creating 4 areas passing through the middle of the water holes: this means that the meshes that we inserted inside the reflector do not intersect any water hole. Fig 3.6 gives the computational mesh, while Fig. 3.7 represents the distribution of spatial errors. Finally, Table 3.7 gives the general situation of the greatest errors in function of the type of the reaction rate and of the output energy mesh.

Table 3.6: Reactivity, fission, capture and total reaction rates errors in one and two groups for the Kaist calculation for the case with SG self-shielding option and the 383-groups cross section library.

Reference: TRIPOLI-4®		1 group	fast group	thermal group
Reactivity error (pcm)		-71		
Fission rates error (%)	min	-0.90	-0.69	-1.92
	max	1.35	1.12	1.73
	RMS	0.41	0.29	0.48
Capture rates error (%)	min	-0.82	-0.63	-1.29
	max	1.10	1.59	1.83
	RMS	0.32	0.28	0.43
	reflector	2.92	2.80	2.94
Total rates error (%)	min	-0.28	-0.20	-0.79
	max	0.90	0.74	2.24
	RMS	0.24	0.23	0.39
	reflector	2.78	2.76	2.64

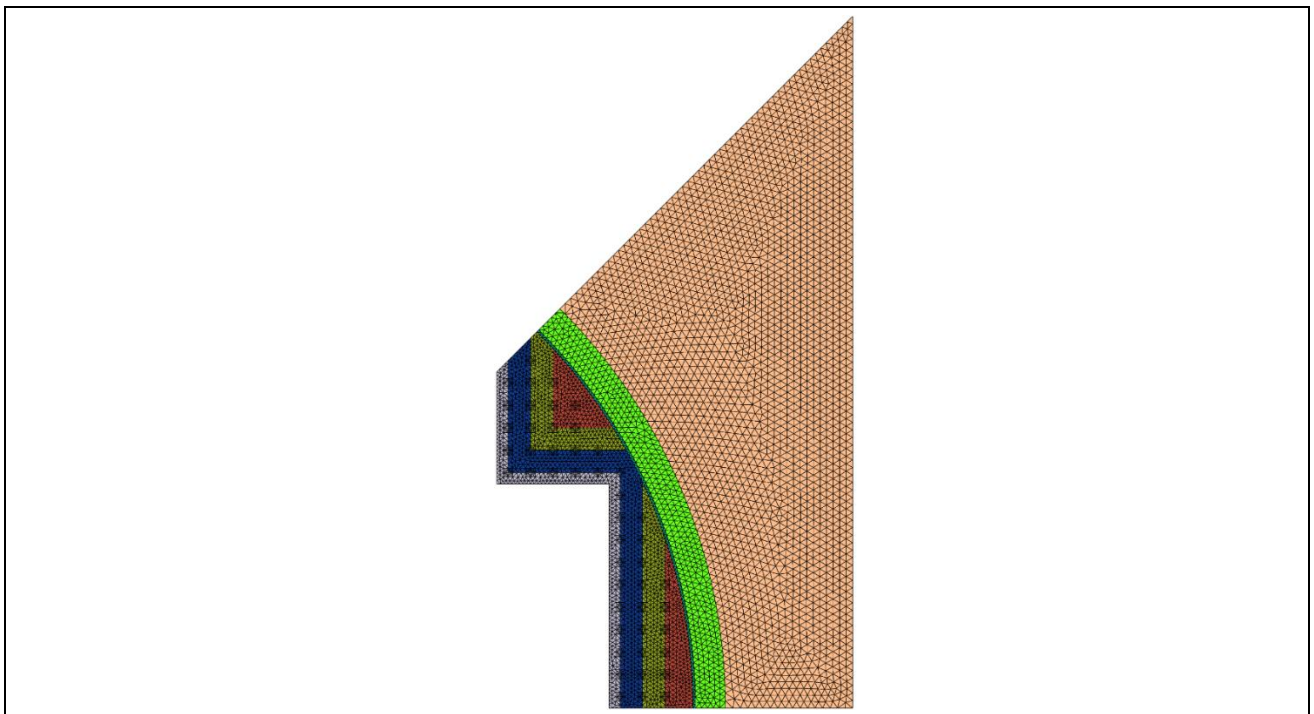


Figure 3.6: ALAMOS model of exact reflector geometry with layer media separately computed to separately compute some adapted self-shielded cross section in each reflector zone.

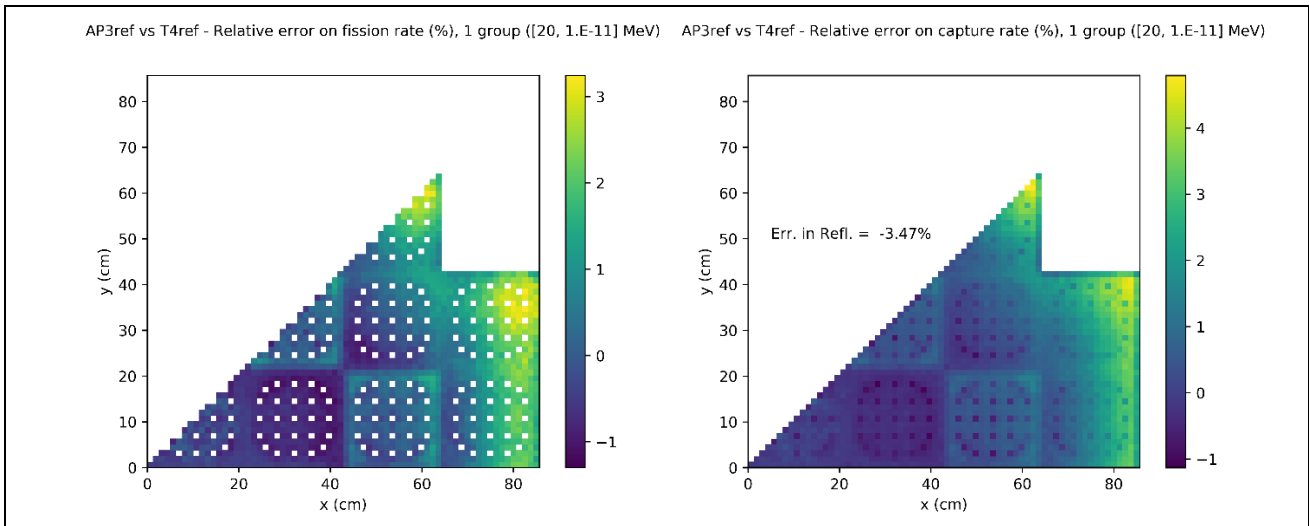


Figure 3.7: Spatial distribution of the pin-by-pin error on one group fission and capture rates with an exact reflector and multiple Self-Shielding zones.

Table 3.7: Reactivity, fission, capture and total reaction rates errors in one and two groups, for the case of exact reflector geometry with layer media separately computed to represent local shielding effects.

Reference: TRIPOLI-4®		1 group	fast group	thermal group
Reactivity error (pcm)		-187		
Fission rates error (%)	Min	-1.30	-0.91	-2.73
	Max	3.24	5.07	3.15
	RMS	0.67	0.69	0.75
Capture rates error (%)	Min	-1.13	-0.64	-1.88
	Max	4.79	6.71	3.33
	RMS	0.62	0.83	0.67
	Reflector	-3.47	9.96	-11.48
Total rates error (%)	Min	-0.63	-0.47	-1.19
	Max	5.56	6.94	3.35
	RMS	0.67	0.63	0.83
	Reflector	7.70	10.06	-12.26

The results of this case are degraded with respect to those of Case 1. This deceiving result is probably due to the fact that we removed some compensation of Case 1. Case 7 is more faithful to the true geometry, and the computational model also more realistic. It is worth noting anyway that, even if we don't have remarkable improvements in the active zone, this case gives a slight improvement in the capture rates of the reflector while total ones are worsened. This probably indicates that the previous Case 1 model is subjected to important compensation that are probably removed with a more detailed model. We suppose therefore that important progress should be done in the shielding model or computational options for the reflector.

3.3 Evaluating the reflector modelling

This part analyzes how simplifying the reflector description in terms of geometry and composition affects the k_{eff} and fission/capture reaction rates. The goal is to study the impact of those simplifying hypothesis usually adopted to model the heavy reflector at core level.

Several configurations are tested, the material balance of the reflector is preserved in any case. The APOLLO3® results are compared to the exact cylindrical reflector case with explicit water hole description of Fig. 3.1. As before, output reaction rates are given for one and two energy groups. Pin-by-pin homogenization is used in the fuel assemblies but only one region is considered in the reflector. Only the new slab modelling is used.

The conversion from a round to a Cartesian reflector studied in following sections is accomplished using the specialized functions `approximate_circle` and `sketcher` of ALAMOS tool³.

3.3.1 Case 1: Homogenized cylindrical reflector

In this first case, the reflector has the same dimensions and shape as the reference one, but no water channels. The water is homogeneously distributed over the entire reflector. Fig.3.8 describes the ALAMOS geometrical model for this test case.

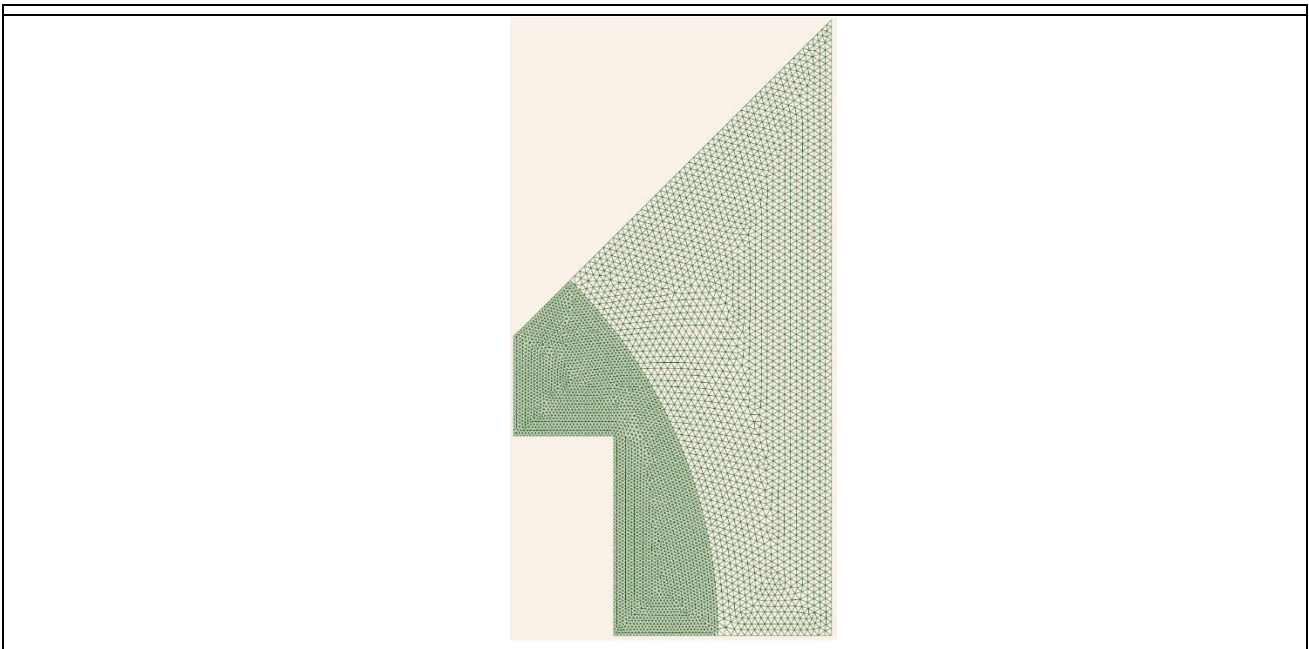


Figure 3.8: ALAMOS model of the curvilinear reflector model with smeared water holes.

In the following Fig. 3.9 we show the errors on fission and capture rates with respect to the reference APOLLO3® calculation. As for error on reactivity, only 17 pcm error is due to this approximation as it is shown in Table 3.8 where a general sketch of the situation is

³ For more details one can refer to the ALAMOS-9.8 documentation.

given. In particular, it is possible to remark that the maximal error on the fission, capture, and total rates due to the thermal flux grows up to 4.8%. As Fig. 3.9 shows, the maximum error in the fuel is located on the diagonal at the reflector interface. The absence in the reflector of water holes in this diagonal could be the reason: smearing the water uniformly creates in this region an undue moderation that is not present in the reference model. As a matter of fact, we believe this first simple calculation shows that the local-range moderation associated to water holes cannot be correctly approximated with smearing it, or alternatively, without applying an equivalence that *locally* prevents the smearing to erase heterogeneities. This may become more important in VVER cases where the holes dimensions are more variable. This is actually what is done in the industrial computational schemes, like for example in France. The errors induced by this procedure are probably negligible on global reactivity but can rise very fast to more than 4% on the pins at the interface with reflector. Even if these pins are usually not those with the highest power, they are nevertheless those that impact more the dose absorbed by the reflector. So that the classical calculation implies a strong overestimation.

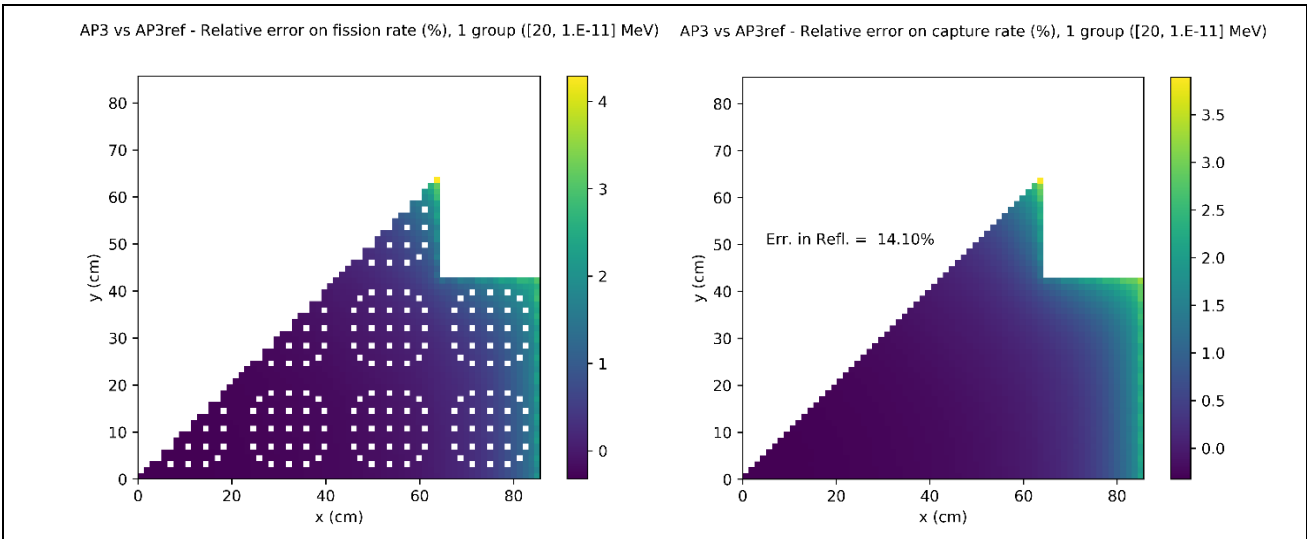


Figure 3.9: Spatial distribution of the pin-by-pin error on one group fission and capture rates due to the approximation of smearing water holes in the reflector.

Table 3.8: Reactivity, fission, capture and total reaction rates errors in one and two groups due to the smearing of the water holes in the reflector. Case 1.

Reference: APOLLO3®		1 group	fast group	thermal group
Reactivity error (pcm)		17		
Fission rates error (%)	min	-0.32	-0.33	-0.32
	max	4.29	2.98	4.83
	RMS	0.28	0.23	0.29
Capture rates error (%)	min	-0.32	-0.33	-0.32
	max	3.89	3.48	4.87
	RMS	0.28	0.26	0.31
	reflector	14.10	20.21	9.92
Total rates error (%)	min	-0.33	-0.33	-0.32
	max	2.97	2.87	4.84
	RMS	0.31	0.29	0.38
	reflector	17.90	19.59	2.87

3.3.2 Case 2: homogenized Cartesian reflector (1 assembly step)

The following cases 2, 3, 4 and 5 concern the evaluation of the impact of deforming the correct geometry of the reflector with a Cartesian segmentation. This is typically done in industrial calculations where the diffusion or SPn core solvers largely rely on Cartesian geometries (for which they can perform very fast calculations). In this Case 2, the cylindrical reflector is substituted by a Cartesian one, homogenized. The “cartesianization” step is equal to 1 assembly side length (i.e., 21.42 cm). Fig. 3.10 shows the computational mesh.

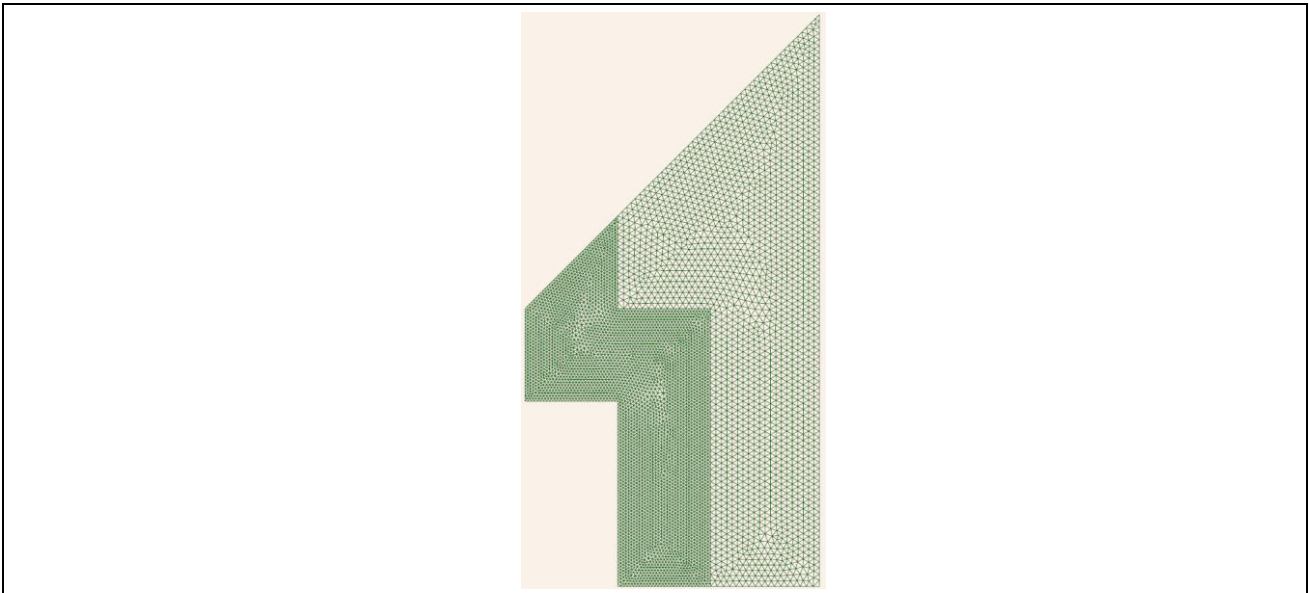


Figure 3.10: ALAMOS model of the Cartesian reflector geometry with a step of 1 assembly side length. Case 2.

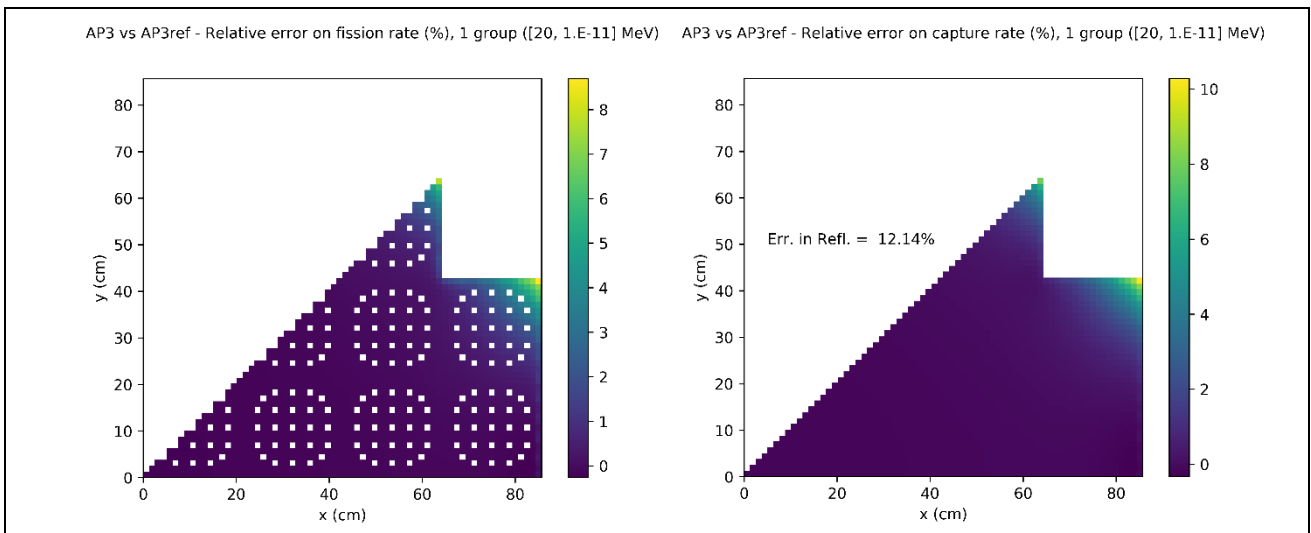


Figure 3.11: Spatial distribution of the pin-by-pin error on one group fission and capture rates due to the Cartesian approximation of the reflector with a side equal to one assembly length. Case 2.

The maximum error in the fuel is located at the outset corner, where the reflector thickness has changed the most between the two modellings. Maximum errors are higher, but RMS are similar to the homogenized cylindrical case. As before, the error in reactivity is negligible, but overestimations up to 10% are present in pins where the reflector capacity is

mostly changed. Our analysis here is that it is not possible to tolerate such errors without accepting strong biases throughout depletion and renouncing to have acceptable errors at the core-reflector interface. Figure 3.11 gives the errors spatial distribution while Table 3.9 gives information about the values of the largest errors in function of their type, with one or two output groups.

Table 3.8: Reactivity, fission, capture and total reaction rates errors in one and two groups, for the case of Cartesian reflector with a side of 1 assembly length. Case 2.

Reference: APOLLO3®		1 group	fast group	thermal group
Reactivity error (pcm)		9		
Fission rates error (%)	min	-0.26	-0.41	-0.26
	max	8.69	9.64	8.31
	RMS	0.24	0.19	0.25
Capture rates error (%)	min	-0.33	-0.46	-0.26
	max	10.28	11.10	8.40
	RMS	0.25	0.24	0.26
	reflector	12.14	13.87	10.56
Total rates error (%)	min	-0.38	-0.57	-0.26
	max	10.36	10.90	8.45
	RMS	0.29	0.27	0.36
	reflector	11.95	13.01	2.64

3.3.3 Case 3: homogenized Cartesian reflector (0.5 assembly step)

This case is an improvement of the previous one since we divided the step of the segmentation of the reflector by two. Fig. 3.12 depicts the computational mesh while Fig. 3.13 gives the spatial error distribution. The maximum errors in the fuel are located at the corners, in this case they are negative. Detailed information about the values of strongest errors in function of their type and of the output mesh (one or two groups) is given in Table 3.9.

As for their order of magnitude, they remain similar to those of Case 2, more or less close to 10%. It is important here to remark that Cases 2 and 3 are the reflector geometry approximations adopted in industrial calculation schemes and that no direct equivalence is done to reduce the biases that we have described here. In fact, the only equivalence adopted is that of preserving mono-dimensional albedos that cannot reduce any of the errors described here.

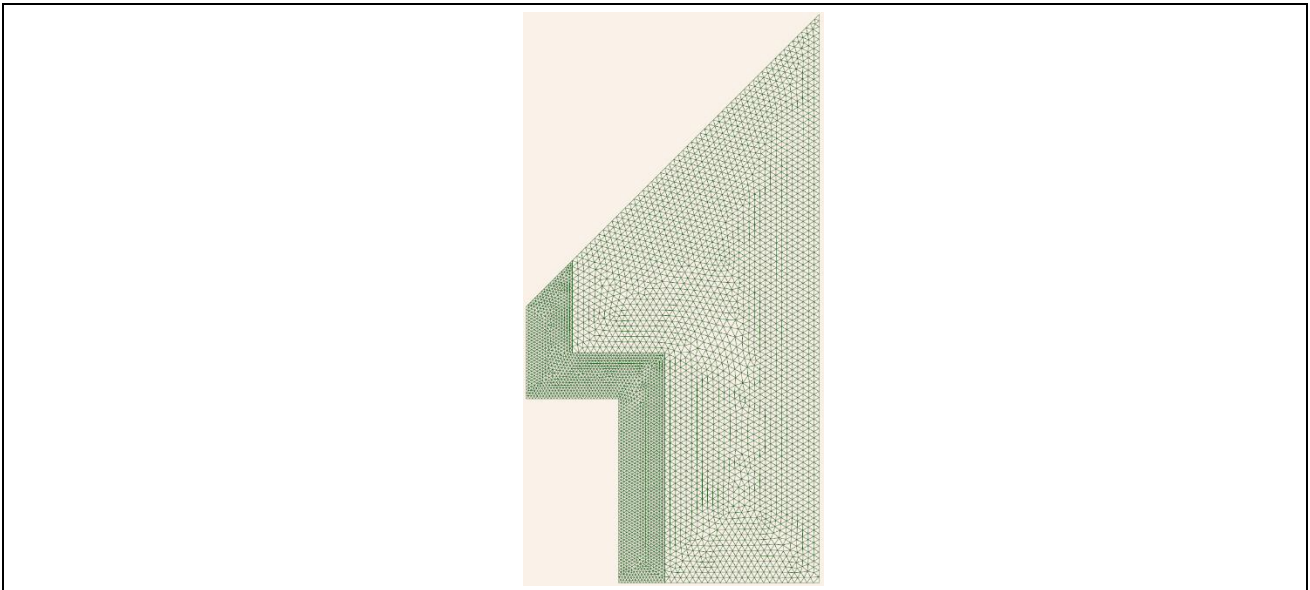


Figure 3.12: ALAMOS model of the Cartesian reflector geometry with a step of 1/2 assembly side length. Case 3.

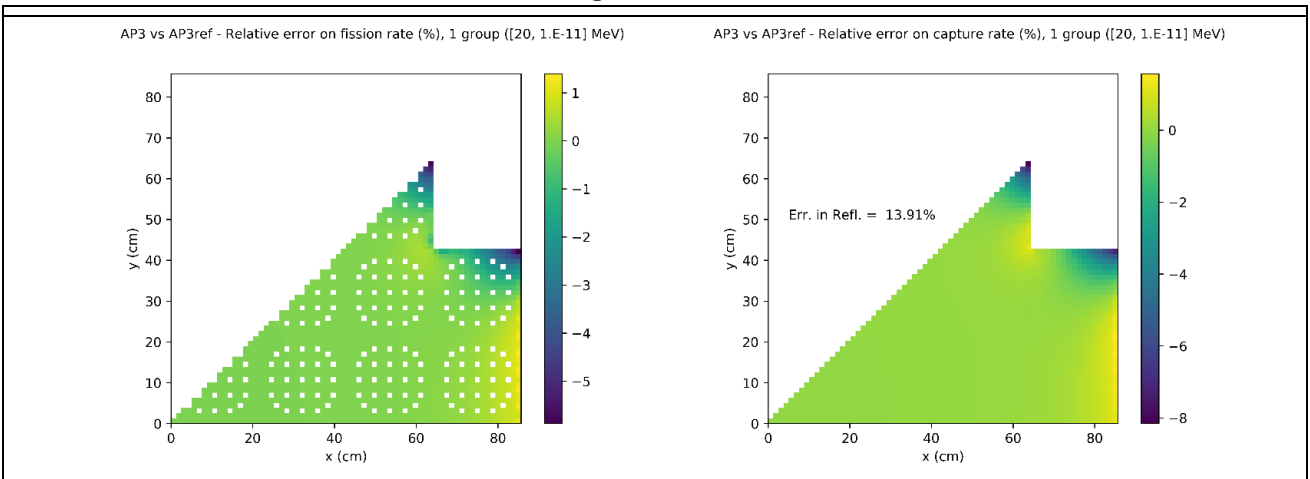


Figure 3.13: Spatial distribution of the pin-by-pin error on one group fission and capture rates due to the Cartesian approximation of the reflector with a side equal to 1/2 assembly length. Case 3.

Table 3.9: Reactivity, fission, capture and total reaction rates errors in one and two groups, for the case of Cartesian reflector with a side of 1/2 assembly length. Case 3.

Reference: APOLLO3®		1 group	fast group	thermal group
Reactivity error (pcm)		4		
Fission rates error (%)	Min	-5.88	-8.43	-5.32
	Max	1.39	1.26	1.44
	RMS	0.14	0.12	0.15
Capture rates error (%)	Min	-8.16	-9.62	-5.34
	Max	1.56	2.39	1.43
	RMS	0.16	0.19	0.14
	reflector	13.91	16.93	12.03
Total rates error (%)	Min	-9.55	-10.82	-5.50
	Max	1.46	2.16	1.37
	RMS	0.22	0.22	0.23
	Reflector	14.88	16.14	4.35

3.3.4 Case 4: homogenized Cartesian reflector (0.5 assembly step + square)

In this case, we tried to approximate the reflector with a more representative segmentation curve, including an inset corner, and maintaining a $\frac{1}{2}$ assembly (i.e., 10.21 cm) length side. The maximum errors in the fuel are halved with respect to the previous case. Detailed information about the values of strongest errors in function of their type and of the output mesh (one or two groups) is given in Table 3.10. In Fig. 3.15 the spatial distribution of the errors can be found, while in Fig. 3.14 we depict the computational mesh.

This geometrical model proves therefore to be more acceptable in practical cases without implying any overcharge. Having said that, it is evident anyway that a 5% error on reaction rates can entail important biases along depletion.

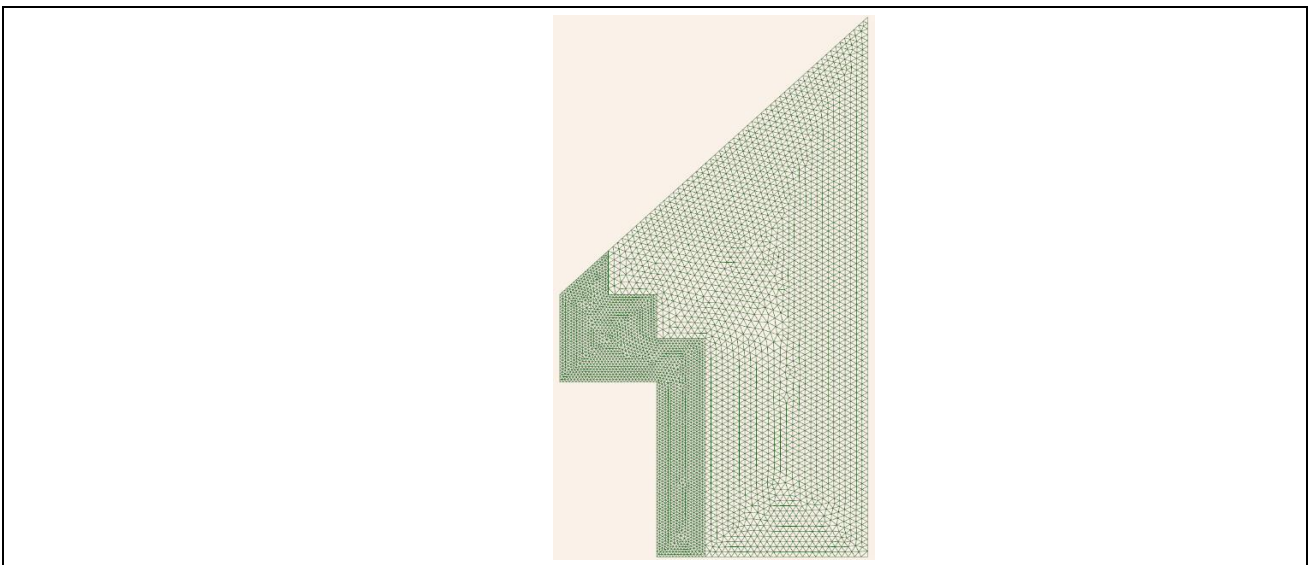


Figure 3.14: ALAMOS model of the Cartesian reflector geometry with a step of 1/2 assembly side length including an inset corner. Case 4.

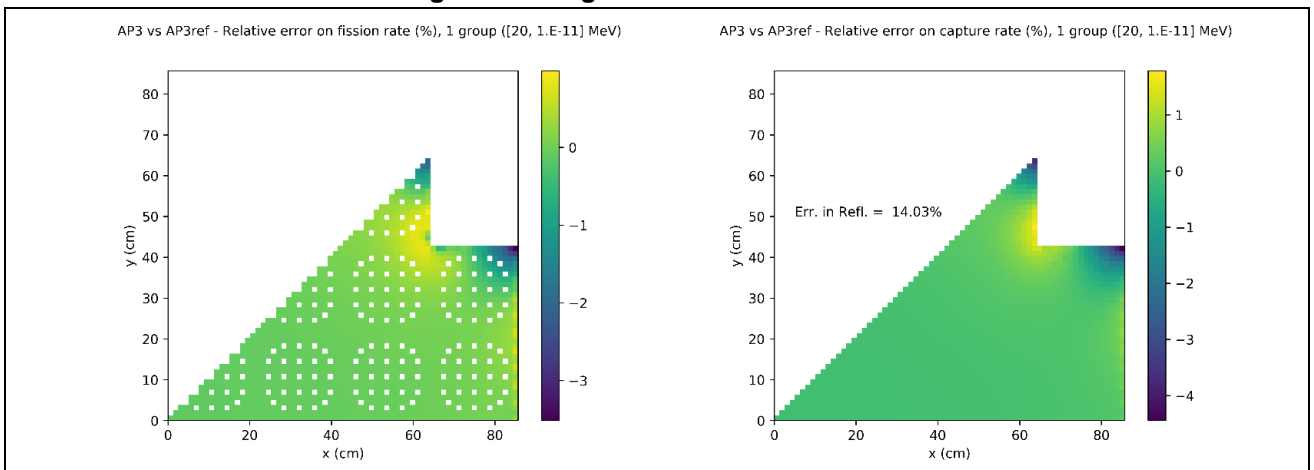


Figure 3.15: Spatial distribution of the pin-by-pin error on one group fission and capture rates due to the Cartesian approximation of the reflector with a side equal to 1/2 assembly length with an inset corner. Case 4.

Table 3.10: Reactivity, fission, capture and total reaction rates errors in one and two groups, for the case of Cartesian reflector with a side of 1 assembly length with an inset core. Case 4.

Reference: APOLLO3®		1 group	fast group	thermal group
Reactivity error (pcm)		8		
Fission rates error (%)	min	-3.51	-4.71	-3.03
	max	0.99	1.55	1.09
	RMS	0.12	0.11	0.13
Capture rates error (%)	min	-4.45	-5.06	-3.03
	max	1.78	2.63	1.10
	RMS	0.13	0.15	0.12
	reflector	14.03	18.48	11.32
Total rates error (%)	min	-5.29	-6.33	-3.16
	max	1.78	2.40	1.05
	RMS	0.16	0.17	0.16
	reflector	16.08	17.52	3.94

3.3.5 Case 5: homogenized Cartesian reflector (preserved volume)

In this case, we considered an approximation where the Cartesian reflector is obtained by preserving the original volume. Hence, the Cartesianization step is equal to 16.915 cm. The computational mesh is shown in Fig. 3.16. As shown in the following, this model works quite better than the previous ones but suffers from the fact that the “core” solver should be able to treat non-conformal meshes. In the case of the MINOS solver of the APOLLO3® code this is possible but at the price of renouncing to use pure conformal Cartesian meshes that are much faster. As for nodal methods, the same could be said: using non conformal meshes is in the range of possibilities but it implies longer computational times. Here we study therefore this possibility in order to evaluate the biases, but to evaluate the break-even between a strong precision and a longer computational time this case should be studied at the core level. The final results are similar to those of Case 1.

This could be considered quite surprising in fact, since the local geometry of the reflector is quite dissimilar to the correct one. But looking at Fig. 3.17 and Table 3.12, one finds that the errors are really similar to those of Case1.

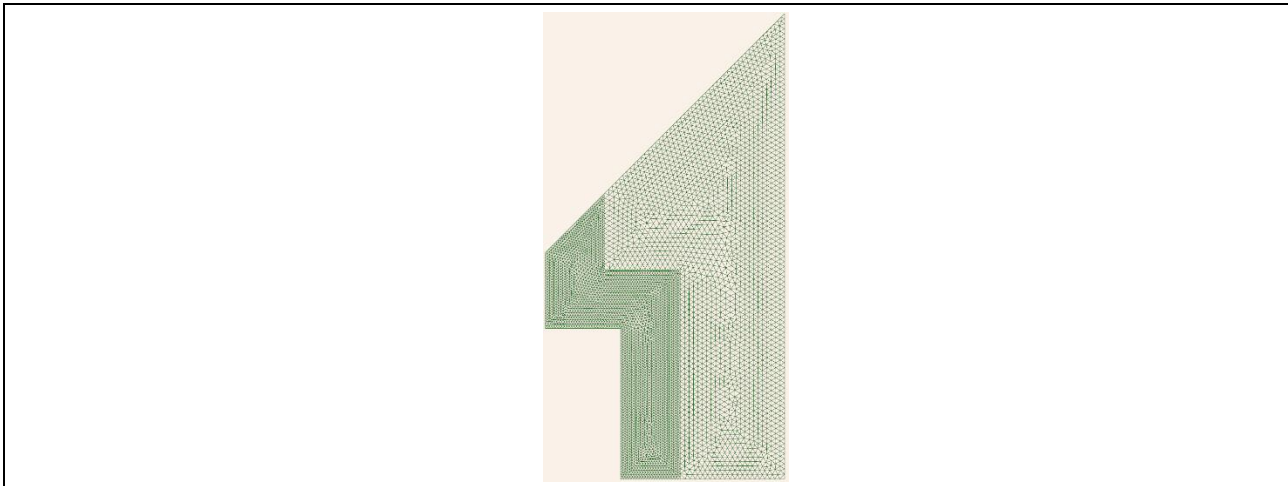


Figure 3.16: ALAMOS model of the Cartesian reflector geometry with a step that preserves the volume. Case 5.

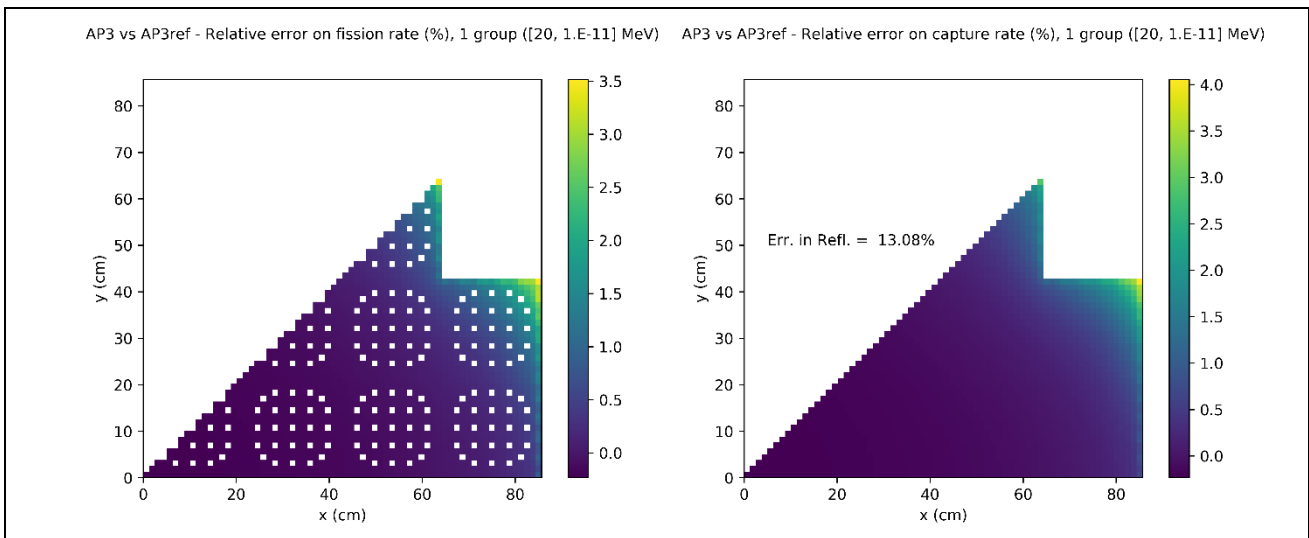


Figure 3.17: Spatial distribution of the pin by pin error on one group fission and capture rates due to the Cartesian approximation of the reflector of the same volume as the reference one. Case 5.

Table 3.11: Reactivity, fission, capture and total reaction rates errors in one and two groups, for the case of Cartesian reflector by preserving reflector volume. Case 5.

Reference: APOLLO3®		1 group	fast group	thermal group
Reactivity error (pcm)		12		
Fission rates error (%)	min	-0.23	-0.24	-0.23
	max	3.52	3.44	4.03
	RMS	0.21	0.17	0.22
Capture rates error (%)	min	-0.23	-0.24	-0.23
	max	4.05	4.25	4.07
	RMS	0.21	0.20	0.23
	reflector	13.08	15.44	11.10
Total rates error (%)	min	-0.24	-0.24	-0.23
	max	3.70	3.74	4.03
	RMS	0.23	0.21	0.29
	reflector	13.47	14.62	3.30

3.3.6 Case 6: homogenized Cartesian reflector (cell step)

This case treats a computational mesh where the size of the reflector segmentation is that of the cell length (i.e., 1.26 cm). This limit case is that of the highest possible precision in core calculations. Figs 3.18 and 3.19 describe the computational mesh and the error spatial distribution, while Table 3.13 gives the values of strongest errors per type of reaction rate and in function of output energy mesh.

As expected, with this mesh the errors are of the same order of those of Case 1 (where only the smearing of water holes was done).

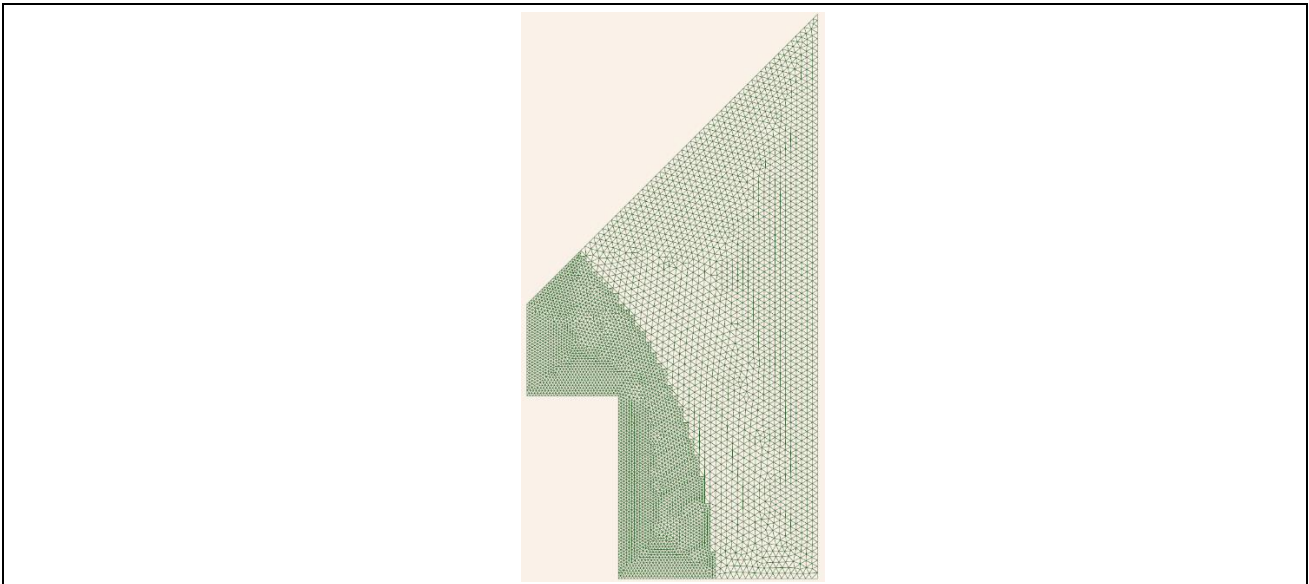


Figure 3.18: ALAMOS model of the Cartesian reflector geometry with a segmentation step equal to the cell side length. Case 6.

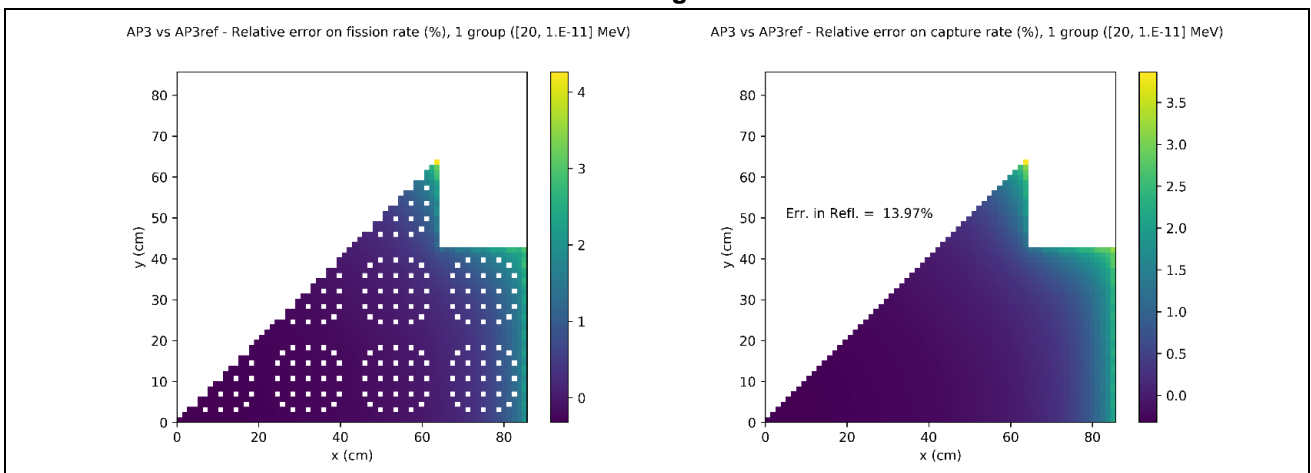


Figure 3.19: Spatial distribution of the pin-by-pin error on one group fission and capture rates due to the Cartesian approximation of the reflector of the same volume as the reference one. Case 6.

Table 3.13: Reactivity, fission, capture and total reaction rates errors in one and two groups, for the case of Cartesian reflector with a segmentation length equal to the cell side. Case 6.

Reference: APOLLO3®		1 group	fast group	thermal group
Reactivity error (pcm)		17		
Fission rates error (%)	min	-0.32	-0.33	-0.32
	max	4.26	2.96	4.80
	RMS	0.28	0.23	0.29
Capture rates error (%)	min	-0.32	-0.32	-0.32
	max	3.86	3.45	4.84
	RMS	0.28	0.26	0.31
	reflector	13.97	19.92	10.18
Total rates error (%)	min	-0.32	-0.33	-0.32
	max	2.94	2.77	4.81
	RMS	0.31	0.28	0.38
	reflector	17.56	19.26	3.06

3.3.7 Case 7: exact cylindrical reflector + multi-zone + octagonal water holes

In the actual version of APOLLO3®, when an external geometry (reflector meshed with ALAMOS) is imported and merged with native geometry, the arcs included into the external geometry are transformed into segments. This anomaly was present in our initial Case 1 in the deterministic calculation but was correctly represented (with arc of circles) in the TRIPOLI-4® calculation. To avoid volume difference of material (with respect to the initial benchmark specification), a solution is to add an extra circle or a polygonal mesh. This case is here studied to verify that the previously defined Case 1 is coherent and that we have not introduced any error due to this geometrical approximation. It is worth noting that in future version of APOLLO3®, taking advantage of the work described in Appendix A, such problem will be overcome.

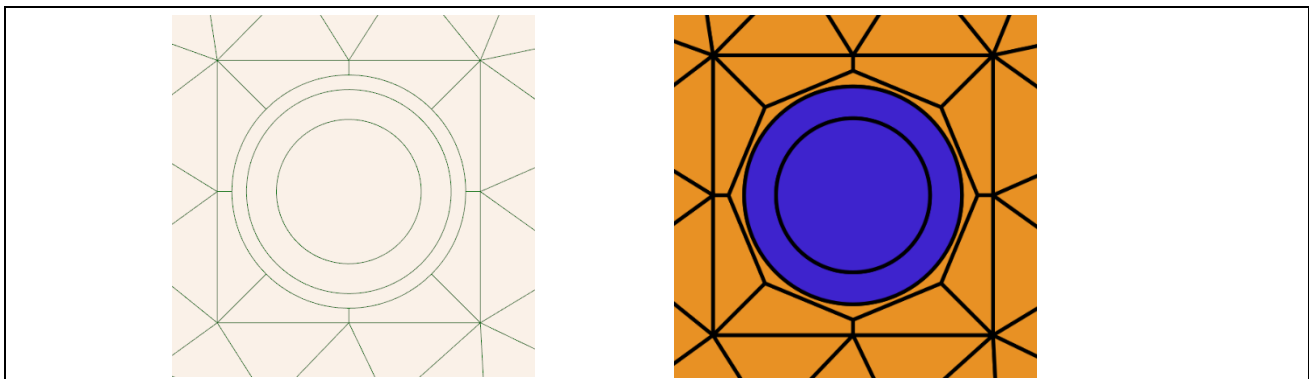


Figure 3.19a: From ALAMOS to APOLLO3® with extra circle. Case of multizoning in subsection 3.2.1.

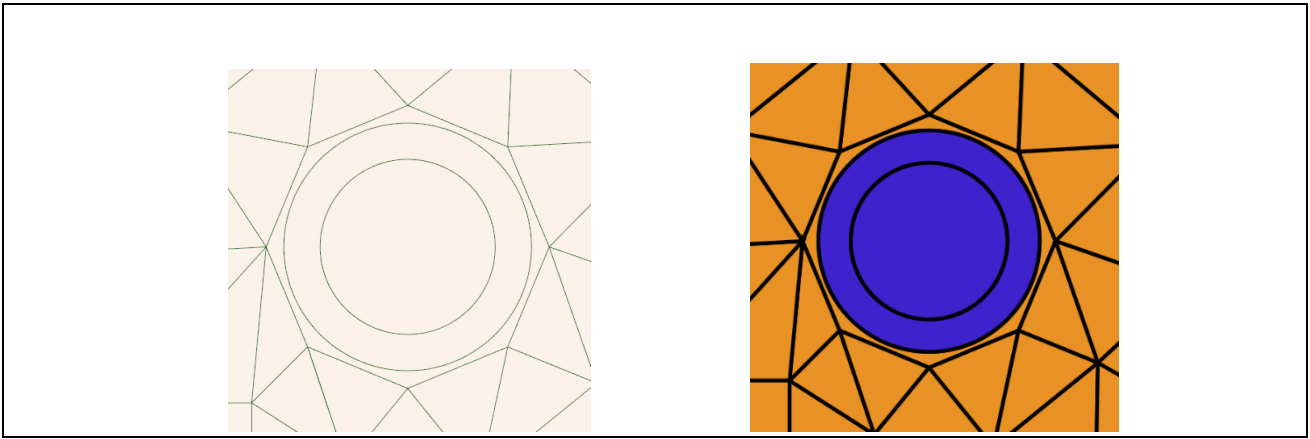


Figure 3.19b: From ALAMOS to APOLLO3® with polygonal mesh. Case 7.

An important point anyway is the fact that when using the native geometrical capabilities one can easily define shielding and depletion schemes onto different geometries and, if these geometries are built in a hierarchical way, the code itself can reconstruct the geometrical links between the different models. When using an external geometry, it is up to the external code (in this case ALAMOS) to provide the geometrical equivalence data.

Figure 3.19a describes all the cases (2 extra segments in case of sub-section 3.2.1 for the multizoning) except case 8 which is described in the added figure (Fig.3.19b) with octagonal mesh in Alamos instead of extra circle. Moreover, material properties in the reflector are also divide into 4 zones passing to the side of the water holes (Fig.3.21) but in the middle in the case of sub-section 3.2.1.

Figs 3.19 and 3.20 and Table 3.14 describe the situation. They confirm that the previous Case 1 is correct and that the previous analyses are coherent with the geometrical and material description of the reference case.

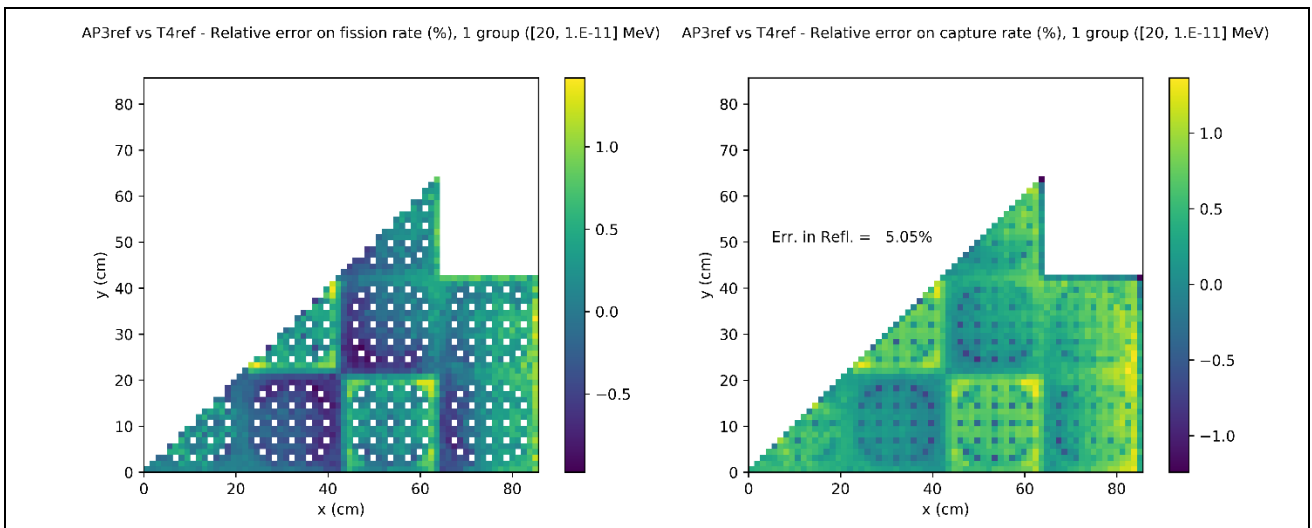


Figure 3.20: From ALAMOS to APOLLO3® with extra circle. Case 7.

Table 3.14: Fission, capture and total errors on one and two groups, for the case of exact reflector geometry with explicit water holes with polygonal meshes. Comparisons with respect to TRIPOLI-4® results. Case 7.

Reference: TRIPOLI-4®		1 group	fast group	thermal group
Reactivity error (pcm)		-219		
Fission rates error (%)	min	-0.97	-0.55	-2.36
	max	1.42	1.39	1.66
	RMS	0.41	0.68	0.45
Capture rates error (%)	min	-1.24	-2.11	-1.71
	max	1.36	2.21	1.60
	RMS	0.52	0.85	0.38
	reflector	5.05	9.70	2.27
Total rates error (%)	min	-0.29	-0.06	-0.89
	max	1.23	1.24	2.03
	RMS	0.25	0.26	0.40
	reflector	4.81	5.15	1.92

3.3.8 Case 8: exact cylindrical reflector + extended fuel slice

In this last case, we increased the active fissile part in the reflector model of Fig. 3.3 and included in it up to 5 fissile assemblies. The rationale behind this is to improve the neutron spectrum used to homogenize the reflector cross sections, having a global reactivity for the reflector model which is closer to the critical value. As shown in Table 3.15, there is not clear improvement, probably because the residual error remaining is due to reflector self-shielding or peripheral treatment of fissile assemblies.

Table 3.15: Reactivity, fission, capture and total reaction rates errors in one and two groups, for the case of exact reflector and extended reflector self-shielding model (with 5 fissile assemblies). Case 8.

Reference: TRIPOLI-4®		1 group	fast group	thermal group
Reactivity error (pcm)		-221		
Fission rates error (%)	min	-0.97	0.54	-2.33
	max	1.59	1.41	1.85
	RMS	0.40	0.69	0.44
Capture rates error (%)	min	-0.89	-1.11	-1.71
	max	1.58	2.02	1.70
	RMS	0.53	0.86	0.38
	reflector	3.32	3.22	3.34
Total rates error (%)	min	-0.28	-0.03	-0.89
	max	1.27	1.22	2.03
	RMS	0.24	0.25	0.39
	reflector	3.69	3.75	3.06

4 The new LS-xy method

In this section, we explain the basics of the LS-xy scheme newly developed in the TDT lattice solver of APOLLO3[®]. It is an enhanced methodology with respect to the standard SC or of the alternative higher order LS method. The section is a synthetic version of the paper [16] to which we refer the interested reader for a complete description.

4.1 The LS scheme

The basic SC transmission equation can be written as:

$$\psi^+ = \beta(q - \psi^-) + \psi^-, \quad 4.1$$

which is simply a rewritten form of Eq. 4.2 for the case of constant emission density per computational region. In Eq. 4.1, $\beta = 1 - e^{-\tau}$ and we used the same notation as in Eqs. 4.4 and in the following ones. The numerical approximation used in Eq. 4.1 is quite rude and can be improved by allowing a linear emission density representation. To this aim, in the LS scheme of APOLLO2 (and then APOLLO3[®]) it has been envisaged to interpolate linearly among surface values [15].

To explain this approach, let us suppose that the boundary of a computational region D_i (∂D_i) is divided in N_s surfaces⁴ as illustrated in Fig 4.1. Within D_i , the flux angular moments are interpolated along each trajectory according to

$$\vec{\phi}_t(s) = \frac{1}{2}(\vec{\phi}_{\alpha^{out},t} + \vec{\phi}_{\alpha^{in},t}) + \frac{s}{l_t}(\vec{\phi}_{\alpha^{out},t} - \vec{\phi}_{\alpha^{in},t}) + \vec{\delta\phi}, \quad 4.2$$

where $\vec{\delta\phi}$ is a free volumetric parameter, while $\vec{\phi}_{\alpha^{in},t}$ and $\vec{\phi}_{\alpha^{out},t}$ are the surface-averaged flux angular moments at the entering and exiting points of the trajectory. These averages are calculated as

$$\vec{\phi}_{\alpha} = \frac{1}{4\pi S_{\alpha}} \int_{4\pi} d\Omega \int_{\alpha} dS \vec{A}(\Omega) \psi(\mathbf{r}_S, \Omega) \approx \frac{1}{S_{\alpha}} \sum_n \omega_n \vec{A}(\Omega_n) \sum_{t \parallel \Omega_n, t \cap \alpha} \frac{\omega_{t,\alpha}^{\perp}}{|\Omega_n \cdot \mathbf{n}|} \psi_{t,\alpha}(\Omega_n), \quad 4.3$$

where \vec{A} is the set of real spherical harmonics⁵ (defined in [16]), Ω_n and ω_n the angular quadrature abscissas and weights, $\omega_{t,\alpha}^{\perp}$ is the portion of cross sectional area affected by the trajectory, and S_{α} is the area of surface α evaluated as follows according to the trajectory-based discretization:

$$S_{\alpha} = \frac{1}{4\pi} \int_{4\pi} d\Omega \int_{\alpha} dS \approx \sum_n \omega_n \sum_{t \parallel \Omega_n, t \cap \alpha} \frac{\omega_{t,\alpha}^{\perp}}{|\Omega_n \cdot \mathbf{n}|}$$

⁴ In TDT, the number of surfaces in which each boundary is divided is calculated as $N_s = \min(\frac{\Lambda}{\lambda^{\min}}, N_s^{\max})$, where Λ is the length of the boundary element and N_s^{\max} and λ^{\min} are two user-defined constants representing the maximum number of divisions requested and the minimum acceptable length of each resulting surface.

⁵ We adopt the vector notation $\vec{A}(\Omega) := \{A_{\rho}(\Omega), \rho = 1, \dots, N_m\}$, where $N_m = [(L+1)(L+2)]/2$, L being the maximum anisotropy order.

Eq. 4.2 enforces the implicit dependence of $\vec{\phi}$ within a region on the direction Ω , thus making the approximation not coherent⁶. Moreover, the flux moments are discontinuous across region interfaces, and this is necessary for a conservative scheme. In fact, particle conservation is enforced by suitable definition of $\overline{\delta\vec{\phi}}$ in each region, as showed in the following.

4.1.1 Transmission equation

After introducing an LS approximation of the external source coherent to Eq. 4.2, we can plug it into the following integral transport equation

$$\psi_t(s) = \psi_t^{in} e^{-\Sigma(s+\frac{l_t}{2})} + \int_{-l_t/2}^s ds' q_t(\mathbf{r}_t^m + s'\Omega) e^{-\Sigma(s-s')}, \quad 4.4$$

from which the transmission equation is derived:

$$\psi_t^{out} = \psi_t^{in} e^{-\Sigma l_t} + \int_{-l_t/2}^{l_t/2} ds q_t(\mathbf{r}_t^m + s\Omega) e^{-\Sigma(\frac{l_t}{2}-s)}. \quad 4.5$$

Here, $\psi_t^{in/out}$ are the angular fluxes at the entering/exiting point of the trajectory, whose midpoint is $\mathbf{r}_t^m = (\mathbf{r}_t^{in} + \mathbf{r}_t^{out})/2$; l_t is the chord length within D_i , whose half and optical counterpart are respectively indicated with $\Delta_t = -l_t/2$ and $\tau_t = \Sigma l_t$ in the remainder for the sake of conciseness. A sketch of the situation is depicted in Fig. 4.1. Finally, $s \in [-\Delta_t, \Delta_t]$ is a local coordinate along the trajectory.

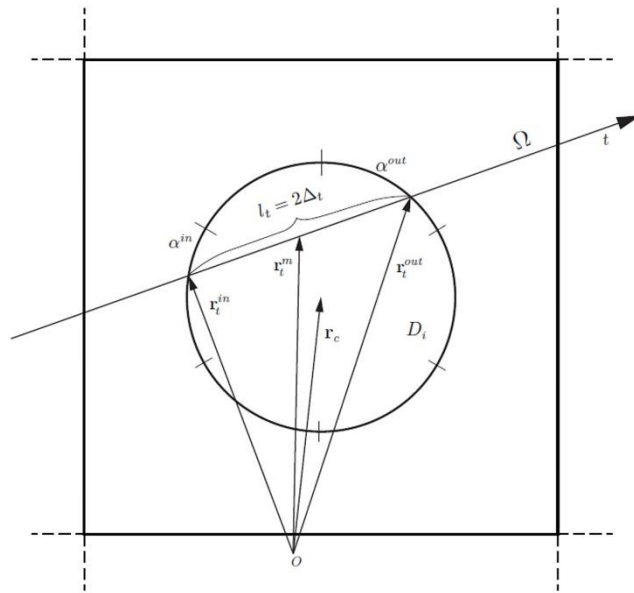


Figure 4.1 : Sketch of the transmission equation over a trajectory cutting a computational region D_i . Note the middle point in chord, and the input/output chord position and the presence of the barycenter in the region.

⁶ In the sense that, at a certain location within D_i , it can predict different values of $\vec{\phi}$ for different directions Ω .

The transmission integral can then be evaluated analytically, resulting into the LS transmission equation:

$$\psi_t^{out} = \psi_t^{in}(1 - \beta_0(\tau_t)) + (\tilde{q}_{\alpha^{in},t} + \delta\tilde{q})\beta_0(\tau_t) + (\tilde{q}_{\alpha^{out},t} - \tilde{q}_{\alpha^{in},t})\beta_1(\tau_t), \quad 4.6$$

where

$$\begin{aligned} \tilde{q}_{\alpha^{in}/\alpha^{out},t} &= \frac{q_{\alpha^{in}/\alpha^{out},t}}{\Sigma}, \\ \delta\tilde{q} &= \frac{\delta q}{\Sigma}, \end{aligned} \quad 4.7$$

and the β_m are spectral factors defined by

$$\beta_0(\tau) = 1 - e^{-\tau}, \quad \beta_1(\tau) = 1 - \frac{1}{\tau}(1 - e^{-\tau}). \quad 4.8$$

4.1.2 Geometric average

Let \mathcal{G} be a *geometric average* operator over region D_i . According to the trajectory-based discretization, it is defined as

$$\begin{aligned} \mathcal{G}(f(\mathbf{r})) = f_G &= \frac{1}{4\pi V_N} \int_{4\pi} d\mathbf{\Omega} \int_{D_i} d\mathbf{r} f(\mathbf{r}) = \frac{1}{4\pi V_N} \int_{4\pi} d\mathbf{\Omega} \int_{\partial D_{i,\perp}} dS_{\perp} \int_{-\Delta t}^{\Delta t} ds f(\mathbf{r}_t^m + s\mathbf{\Omega}) \\ &\approx \frac{1}{4\pi V_N} \int_{4\pi} d\mathbf{\Omega} \sum_{\alpha \in \partial D_i} \sum_{t \parallel \mathbf{\Omega}, t \cap \alpha} \omega_{t,\alpha}^{\perp} l_t \langle f \rangle, \end{aligned} \quad 4.9$$

where $\partial D_{i,\perp}$ is the projection of ∂D_i on the plane perpendicular to $\mathbf{\Omega}$, $dS_{\perp} = dS|\mathbf{\Omega} \cdot \mathbf{n}|$, $\langle f \rangle$ is the average of function f along the chord, and V_N is the numerical volume of region D_i :

$$V_N = \frac{1}{4\pi} \int_{4\pi} d\mathbf{\Omega} V(\mathbf{\Omega}) = \frac{1}{4\pi} \int_{4\pi} d\mathbf{\Omega} \sum_{\alpha,t} \omega_{t,\alpha}^{\perp} l_t. \quad 4.10$$

Here, we introduced the short hand notation $\sum_{\alpha,t} = \sum_{\alpha \in \partial D_i} \sum_{t \parallel \mathbf{\Omega}, t \cap \alpha}$ that we will use for commodity throughout the rest of the section.

We can calculate the geometric average of the flux angular moments by plugging their LS approximation into Eq. 4.9:

$$\vec{\phi}_G = \frac{1}{4\pi V_N} \int_{4\pi} d\mathbf{\Omega} \sum_{\alpha,t} \omega_{t,\alpha}^{\perp} l_t \frac{\vec{\phi}_{\alpha^{in},t} + \vec{\phi}_{\alpha^{out},t}}{2} + \frac{1}{4\pi V_N} \int_{4\pi} d\mathbf{\Omega} \sum_{\alpha,t} \omega_{t,\alpha}^{\perp} l_t \delta\vec{\phi} = \sum_{\alpha \in \partial D_i} \mathbb{M}_{\alpha} \vec{\phi}_{\alpha} + \overline{\delta\vec{\phi}}, \quad 4.11$$

where we introduced \mathbb{M}_{α} , which is a matrix operator to be applied to surface-averaged values whose expression can be found in [16].

4.1.3 Balance equation

By projecting the mono-group transport equation onto the set of spherical harmonics $\vec{A}(\Omega)$ and integrating over in angle and over region D_i , we obtain a balance equation for the flux angular moments:

$$V\Sigma\vec{\phi}_C = V\mathbb{A}\vec{Q}_C - \Delta\vec{J}, \quad 4.12$$

where

$$\vec{\phi}_C = \frac{1}{V} \int_{D_i} d\mathbf{r} \vec{\phi}(\mathbf{r}),$$

are the region-averaged⁷ flux angular moments⁸, and \mathbb{A} is the matrix resulting from the integral of the harmonics tensor product,

$$\mathbb{A} = \frac{1}{4\pi} \int_{4\pi} d\Omega \vec{A}(\Omega) \otimes \vec{A}(\Omega) = \text{diag}\left(\frac{1}{2k+1}\right).$$

The streaming term is evaluated according to

$$\begin{aligned} -\Delta\vec{J} = \vec{J}_- - \vec{J}_+ &= \frac{1}{4\pi} \int_{4\pi} d\Omega \vec{A}(\Omega) \int_{\partial D_{i,\perp}} dS_{\perp} (\psi_t^{in} - \psi_t^{out}) \\ &\approx \sum_n \omega_n \vec{A}(\Omega_n) \sum_{t \parallel \Omega_n, t \cap D_i} \omega_t^{\perp} (\psi_t^{in} - \psi_t^{out}), \end{aligned}$$

where the term in brackets is directly computed from the transmission equation 4.6. Finally, the region-averaged emission density angular moments \vec{Q}_C are calculated with the region-averaged flux angular moments from the previous inner iteration,

$$\vec{Q}_C = \frac{1}{V} \int_{D_i} d\mathbf{r} \vec{q} = \Sigma_s \vec{\phi}_C + \vec{q}_{\text{ext},C} \approx \Sigma_s \vec{\phi}_G + \vec{q}_{\text{ext},G} = \vec{Q}_G.$$

Eq. 4.12 gives a conservative average flux in D_i that is coherent with the computed currents, but it is not numerically coherent with the transmission equation, in the sense that it cannot be derived from it. This matter is discussed in detail in [16].

4.1.4 Enforce conservation

Eq. 4.12 is an approximation because, even at convergence, there is no guarantee that the computed region-averaged flux angular moments coincide with those computed with operator of Eq. 4.11. Therefore, in order to have a conservative method, we must impose that in all regions

⁷ Note that here we use the analytical volume of region D_i and not its numerically evaluated counterpart V_N . This is to ensure numerical robustness even when the trajectory-based discretization is coarse.

⁸ The subscript C indicates that the region-averaged flux angular moments satisfy particle balance (i.e., they are *conservative*)

$$\vec{\phi}_G = \vec{\phi}_C ,$$

4.13

which leads to the criterion necessary to fix the free parameter $\overrightarrow{\delta\phi}$:

$$\overrightarrow{\delta\phi} = \vec{\phi}_C - \sum_{\alpha \in \partial D_i} \mathbb{M}_\alpha \vec{\phi}_\alpha .$$

4.14

This makes the LS scheme non-positive, even though negative values of the surface-averaged flux angular moments can appear only with very coarse discretizations.

4.2 The LS-xy method

The LS scheme can only preserve the constant flux spatial moment. To overcome this limitation, we propose here a more advanced surface-based MOC scheme named *LS-xy*.

4.2.1 Source approximation

The flux angular moments are interpolated along each trajectory crossing region D_i according to

$$\vec{\phi}_t(s) = \frac{1}{2} (\vec{\phi}_{\alpha^{out},t} + \vec{\phi}_{\alpha^{in},t}) + \frac{s}{l_t} (\vec{\phi}_{\alpha^{out},t} - \vec{\phi}_{\alpha^{in},t}) + \overrightarrow{\delta\phi}(s) ,$$

4.15

with

$$\overrightarrow{\delta\phi}(s) = \overrightarrow{\delta\phi}^1 + \overrightarrow{\delta\phi}^{xy} \cdot ((\mathbf{r} - \mathbf{r}_c) \oslash \mathbf{r}^*) = \overrightarrow{\delta\phi}^1 + \overrightarrow{\delta\phi}^{xy} \cdot ((\mathbf{r}_t^m - \mathbf{r}_c) \oslash \mathbf{r}^*) + s \overrightarrow{\delta\phi}^{xy} \cdot (\boldsymbol{\Omega} \oslash \mathbf{r}^*) ,$$

where \oslash is used to indicate the vector element-wise division, and \mathbf{r}^* is the vector whose components are the characteristic dimensions of region D_i in each direction⁹. Similarly to what done by [5] for the polynomial expansion of the flux in the z direction, we choose

$$\mathbf{r}^* := [x^*, y^*]^T = \left[\frac{\Delta x}{2}, \frac{\Delta y}{2} \right]^T = \left[\frac{x_{max} - x_{min}}{2}, \frac{y_{max} - y_{min}}{2} \right]^T .$$

Hence, we can rewrite Eq. 4.15 as

⁹ Note that here and in the rest of the section we adopted a double vector notation. The arrow in $\overrightarrow{\delta\phi}^{xy}$ indicates multiple angular moments, while the boldface font stands for multiple spatial components. Hence, for example, must be read as a compact way of writing N_m equations (one for each angular moment) in each of which the scalar product operator acts only on the spatial components of $\overrightarrow{\delta\phi}^{xy}$.

$$\begin{aligned}\vec{\phi}_t(s) = & \frac{1}{2}(\vec{\phi}_{\alpha^{out},t} + \vec{\phi}_{\alpha^{in},t}) + \overline{\delta\phi^1} + \overline{\delta\phi^{xy}} \cdot ((\mathbf{r}_t^m - \mathbf{r}_c) \otimes \mathbf{r}^*) \\ & + [\vec{\phi}_{\alpha^{out},t} - \vec{\phi}_{\alpha^{in},t} + \overline{\delta\phi^{xy}} \cdot (\boldsymbol{\Omega} \otimes \mathbf{r}^*)l_t] \frac{S}{l_t}.\end{aligned}$$

4.16

Here, $\overline{\delta\phi^1}$ is a constant component as the one in Eq 4.2 valid for the basic LS method, while $\overline{\delta\phi^{xy}} = [\overline{\delta\phi^x}, \overline{\delta\phi^y}]^T$ is the variation of $\overline{\delta\phi}(s)$ in D_i (i.e., $\overline{\delta\phi^{xy}} \otimes \mathbf{r}^*$ is representative of the gradient of $\overline{\delta\phi}(s)$ in D_i). In the LS-xy therefore, the flux correction term is allowed to vary in space, thus improving the flux description within the region. In fact, it is the higher number of free parameters with respect to the classic LS model that allows for imposing the conservation of the x - y spatial moments of the flux. Finally, \mathbf{r}_c is a reference point within D_i (see [16] for the explicit choice of it as the barycenter of the computational region) and it is another free parameter of the problem. Note that also with this approximation $\vec{\phi}$ depends on the direction $\boldsymbol{\Omega}$ and so it is not coherent.

Introducing an LS-xy approximation of the external source coherent to Eq. 4.15, the emission density can be evaluated according to

$$q_t(s) = \frac{1}{2}(q_{\alpha^{out},t} + q_{\alpha^{in},t}) + \frac{S}{l_t}(q_{\alpha^{out},t} - q_{\alpha^{in},t}) + \delta q(s),$$

where $\delta q(s)$ can be expressed as $\overline{\delta\phi}(s)$.

4.2.2 Transmission equation

By substituting Eq. 4.15 in Eq 4.5 and by calculating the transmission integral analytically, we find

$$\begin{aligned}\psi_t^{out} = \psi_t^{in}(1 - \beta_0(\tau_t)) + & \underbrace{\left(\frac{\tilde{q}_{\alpha^{in},t} + \tilde{q}_{\alpha^{out},t}}{2} + \delta\tilde{q}^1 + \delta\tilde{\mathbf{q}}^{xy} \cdot ((\mathbf{r}_t^m - \mathbf{r}_c) \otimes \mathbf{r}^*) \right)}_{\mathcal{A}_t} \beta_0(\tau_t) \\ & + \underbrace{\left(\tilde{q}_{\alpha^{out},t} - \tilde{q}_{\alpha^{in},t} + \delta\tilde{\mathbf{q}}^{xy} \cdot \left(\frac{l_t \boldsymbol{\Omega}}{\mathbf{r}^*} \right) \right)}_{\mathcal{B}_t} \xi(\tau_t),\end{aligned}$$

4.17

where the \sim indicates that the corresponding source term was divided by Σ , and \mathcal{A}_t and \mathcal{B}_t are two trajectory functions. The spectral factor ξ is defined as

$$\xi(\tau) = \left[\frac{1}{2}(1 + e^{-\tau}) - \frac{1}{\tau}(1 - e^{-\tau}) \right] = 1 - \left(\frac{1}{2} + \frac{1}{\tau} \right) \beta_0(\tau)$$

4.17b

and is tabulated, together with β_0 . We notice that only a few more operations have to be performed compared to Eq. 4.6, thus guaranteeing a minimal increase of computational cost with respect to the classic LS scheme.

4.2.3 Geometric averages

The terms $\overline{\delta\phi^1}$ and $\overline{\delta\phi^{xy}}$ are calculated in order to ensure that the approximation is conservative. This is done following the same principle as in Section 4.1.4, that is, by imposing that the geometrical average must be equal to the conservative average coming from the balance equation. However, the presence of extra unknowns (the components of $\overline{\delta\phi^{xy}}$) requires writing three balance equations, which are found by projecting on the spatial bases functions $\left\{1, \frac{x-x_c}{x^*}, \frac{y-y_c}{y^*}\right\}^T$, where $(x_c, y_c)^T$ are the components of \mathbf{r}_c . As a consequence, three geometrical averages must be defined (after introducing a proper expression for \mathbf{r}_c , see [16]).

Constant average

For the constant spatial component, we can use the same geometric average operator defined in for the classic LS scheme. By plugging-in the LS-xy flux interpolation along a chord (Eq. 4.16), one finds

$$\begin{aligned}\vec{\phi}_G^1 &= \frac{1}{4\pi V_N} \int_{4\pi} d\Omega \sum_{\alpha,t} \omega_{t,\alpha}^\perp \left\{ \frac{l_t}{2} (\vec{\phi}_{\alpha}^{in,t} + \vec{\phi}_{\alpha}^{out,t}) + l_t \left[\overline{\delta\phi^1} + \overline{\delta\phi^{xy}} \cdot ((\mathbf{r}_t^m - \mathbf{r}_c) \otimes \mathbf{r}^*) \right] \right\} \\ &= \sum_{\alpha} \mathbb{M}_{\alpha} \vec{\phi}_{\alpha} + \overline{\delta\phi^1},\end{aligned}\tag{4.18}$$

where we used the definitions of V_N (Eq. 4.10) and \mathbf{r}_c . Note that, unsurprisingly, we obtained a constant flux average very similar to Eq. 4.11.

Linear averages

Let $\mathcal{G}^{xy} = [\mathcal{G}^x, \mathcal{G}^y]^T$ be a vector operator returning the x - y geometrical averages of a function $f(\mathbf{r})$. According to the trajectory-based discretization, it is defined as follows:

$$\begin{aligned}\mathcal{G}^{xy}(f(\mathbf{r})) &= \mathbf{f}_G^{xy} = \frac{1}{4\pi V_N} \int_{4\pi} d\Omega \int_{D_i} d\mathbf{r} ((\mathbf{r} - \mathbf{r}_c) \otimes \mathbf{r}^*) f(\mathbf{r}) \\ &= \frac{1}{4\pi V_N} \int_{4\pi} d\Omega \int_{\partial D_{i,\perp}} dS_{\perp} \int_{-\Delta t}^{\Delta t} ds \left[(\mathbf{r}_t^m - \mathbf{r}_c) \otimes \mathbf{r}^* + l_t (\boldsymbol{\Omega} \otimes \mathbf{r}^*) \frac{s}{l_t} \right] f(\mathbf{r}_t^m + s\boldsymbol{\Omega}) \\ &= \frac{1}{4\pi V_N} \int_{4\pi} d\Omega \sum_{\alpha,t} \omega_{t,\alpha}^\perp ((\mathbf{r}_t^m - \mathbf{r}_c) \otimes \mathbf{r}^*) l_t \langle f \rangle \\ &\quad + \frac{1}{4\pi V_N} \int_{4\pi} d\Omega \sum_{\alpha,t} \omega_{t,\alpha}^\perp (\boldsymbol{\Omega} \otimes \mathbf{r}^*) l_t^2 \left\langle \frac{s}{l_t} f \right\rangle.\end{aligned}\tag{4.19}$$

By plugging the flux LS-xy approximation given by Eq. 4.16 into the last two integrals (i.e., we apply the averaging operator \mathcal{G}^{xy} to each flux angular moment separately), after some algebra, and exploiting the definition of \mathbf{r}_c , one can find the linear averages of the neutron flux angular moments:

$$\begin{aligned}
 \vec{\Phi}_G^{xy} = & \frac{1}{4\pi V_N} \int_{4\pi} d\Omega \sum_{\alpha,t} \omega_{t,\alpha}^\perp ((\mathbf{r}_t^m - \mathbf{r}_c) \otimes \mathbf{r}^*) \frac{l_t}{2} (\vec{\phi}_{\alpha^{in},t} + \vec{\phi}_{\alpha^{out},t}) \\
 & + \frac{1}{4\pi V_N} \int_{4\pi} d\Omega \sum_{\alpha,t} \omega_{t,\alpha}^\perp (\Omega \otimes \mathbf{r}^*) \frac{l_t^2}{12} (\vec{\phi}_{\alpha^{out},t} - \vec{\phi}_{\alpha^{in},t}) \\
 & + \frac{\overrightarrow{\delta\Phi}^{xy}}{4\pi V_N} \cdot \left\{ \int_{4\pi} d\Omega \sum_{\alpha,t} \omega_{t,\alpha}^\perp l_t [((\mathbf{r}_t^m - \mathbf{r}_c) \otimes \mathbf{r}^*) \otimes ((\mathbf{r}_t^m - \mathbf{r}_c) \otimes \mathbf{r}^*)] \right. \\
 & \quad \left. + \int_{4\pi} d\Omega \sum_{\alpha,t} \omega_{t,\alpha}^\perp \frac{l_t^3}{12} [(\Omega \otimes \mathbf{r}^*) \otimes (\Omega \otimes \mathbf{r}^*)] \right\}.
 \end{aligned}$$

By switching to a notation where we leave the spatial moments explicit, we can rewrite it in matrix form as

$$\begin{bmatrix} \vec{\phi}_G^x \\ \vec{\phi}_G^y \end{bmatrix} = \sum_{\alpha} \begin{bmatrix} \mathbb{M}_{\alpha}^x \vec{\phi}_{\alpha} \\ \mathbb{M}_{\alpha}^y \vec{\phi}_{\alpha} \end{bmatrix} + \begin{bmatrix} \mathbb{M}_V^{x,x} & \mathbb{M}_V^{x,y} \\ \mathbb{M}_V^{y,x} & \mathbb{M}_V^{y,y} \end{bmatrix} \begin{bmatrix} \overrightarrow{\delta\phi}^x \\ \overrightarrow{\delta\phi}^y \end{bmatrix},$$

4.20

where we have introduced new surface geometrical factors, \mathbb{M}_{α}^x and \mathbb{M}_{α}^y (they are the extension of \mathbb{M}_{α} to the x - y equations) and the volumetric geometrical factor \mathbb{M}_V . In [16], we demonstrate that \mathbb{M}_V has the following corresponding analytical expression:

$$\mathbb{M}_V = \frac{1}{V} \int d\mathbf{r} ((\mathbf{r} - \mathbf{r}_c) \otimes \mathbf{r}^*) \otimes ((\mathbf{r} - \mathbf{r}_c) \otimes \mathbf{r}^*).$$

This operator is symmetric but diagonal only in those regions where the x - y basis functions are orthogonal. Unfortunately, the unstructured meshes used in TDT include regions that do not satisfy this condition, so system Eq. 4.20 must be solved entirely.

4.2.4 Constant balance

By projecting the mono-group transport equation onto the set of spherical harmonics $\vec{A}(\Omega)$ and integrating over region D_i , we can write the constant balance equation for the flux angular moments over region D_i :

$$V\Sigma\vec{\phi}_C^1 = V\Lambda\vec{Q}_C^1 - \Delta\vec{J}^1,$$

4.21

where $\vec{\phi}_C^1$ is defined as in and \vec{Q}_C^1 is calculated as in for the classic LS scheme. Finally,

$$-\Delta\vec{J}^1 = \vec{J}_-^1 - \vec{J}_+^1 \approx \sum_n \omega_n \vec{A}(\Omega_n) \sum_{t \parallel \Omega_n, t \cap D_i} \omega_t^\perp (\psi_t^{in} - \psi_t^{out}),$$

4.22

with $(\psi_t^{in} - \psi_t^{out})$ computed from Eq. 4.17.

4.2.5 Linear balance

For conciseness and to lighten the notation, we treat only the x balance equation. The extension of the following reasoning to the y -equation is straightforward.

We multiply the mono-group transport equation by $\frac{\vec{A}(\Omega) x - x_c}{4\pi x^*}$ and then integrate over angles and region D_i . The following x balance equation for the angular flux moments can thus be obtained (omitting dependencies):

$$\Sigma \int_{D_i} d\mathbf{r} \left(\frac{x - x_c}{x^*} \right) \vec{\phi} = -\frac{1}{4\pi} \int_{4\pi} d\Omega \vec{A} \int_{D_i} d\mathbf{r} \left(\frac{x - x_c}{x^*} \right) (\Omega \cdot \nabla \psi) + \mathbb{A} \int_{D_i} d\mathbf{r} \left(\frac{x - x_c}{x^*} \right) \vec{q}.$$

We can then introduce the first-order conservative average of the flux,

$$\vec{\phi}_C^x = \frac{1}{V} \int_{D_i} d\mathbf{r} \left(\frac{x - x_c}{x^*} \right) \vec{\phi},$$

and of the emission density, which is again calculated with the x -averaged fluxes from the previous inner iteration:

$$\vec{Q}_C^x = \frac{1}{V} \int_{D_i} d\mathbf{r} \left(\frac{x - x_c}{x^*} \right) \vec{q} = \vec{Q}_G^x = \Sigma_s \vec{\phi}_C^x + \vec{q}_{\text{ext},G}^x.$$

The integral of the streaming term can be rewritten as:

$$-\frac{1}{4\pi} \int_{4\pi} d\Omega \vec{A} \int_{D_i} d\mathbf{r} \left(\frac{x - x_c}{x^*} \right) (\Omega \cdot \nabla \psi) = -\frac{1}{4\pi} \int_{4\pi} d\Omega \vec{A} \int_{\partial D_i} dS (\Omega \cdot \mathbf{n}) \psi \left(\frac{x - x_c}{x^*} \right) + \frac{1}{4\pi} \int_{4\pi} d\Omega \vec{A} \frac{\Omega_x}{x^*} \int_{D_i} d\mathbf{r} \psi,$$

which we compactly rewrite as

$$-\Delta \vec{J}^x = -\Delta \vec{J}_1^x + \Delta \vec{J}_2^x.$$

4.23

From here, we could proceed in two ways, described in [16] as Approach A and B. While Approach A is simpler, it is unstable and therefore we do not report here. This matter is discussed in [16]. Here instead we describe only the stable approach.

Approach B

To enforce stability in the LS-xy scheme we rewrite the two terms in Eq 4.23 as:

$$\begin{aligned} -\Delta \vec{J}_1^x &\approx \sum_n \omega_n \vec{A}(\Omega_n) \sum_{t \parallel \Omega_n, t \cap D_i} \omega_t^\perp \left[\psi_t^{\text{in}} \left(\frac{x_t^m - \Delta_t \Omega_{x,n} - x_c}{x^*} \right) - \psi_t^{\text{out}} \left(\frac{x_t^m + \Delta_t \Omega_{x,n} - x_c}{x^*} \right) \right] \\ &= \sum_n \omega_n \vec{A}(\Omega_n) \sum_{t \parallel \Omega_n, t \cap D_i} \omega_t^\perp \left[\frac{x_t^m - x_c}{x^*} (\psi_t^{\text{in}} - \psi_t^{\text{out}}) - \frac{l_t \Omega_{x,n}}{x^*} \left(\frac{\psi_t^{\text{in}} + \psi_t^{\text{out}}}{2} \right) \right], \end{aligned}$$

and

$$\begin{aligned} \Delta \vec{J}_2^x &= \frac{1}{4\pi} \int_{4\pi} d\Omega \vec{A} \frac{\Omega_x}{x^*} \int_{D_i} d\mathbf{r} \psi \approx \frac{1}{4\pi} \int_{4\pi} d\Omega \vec{A} \frac{\Omega_x}{x^*} \int_{\partial D_{i,\perp}} dS_\perp \int_{-\Delta_t}^{\Delta_t} ds \psi_t(s) \\ &\approx \sum_n \omega_n \vec{A}(\Omega_n) \frac{\Omega_{x,n}}{x^*} \sum_t \omega_t^\perp l_t \langle \psi \rangle_t. \end{aligned}$$

Here, $\langle \psi \rangle_t$ is the average flux along the chord which can be evaluated using Eq 4.4:

$$\langle \psi \rangle_t = \frac{1}{l_t} \int_{-\Delta_t}^{\Delta_t} ds \psi_t(s) = \frac{\psi_t^{\text{in}} - \psi_t^{\text{out}}}{\tau_t} + \mathcal{A}_t,$$

where the definition of \mathcal{A}_t was used. Therefore, by summing the two terms, we find that

$$-\Delta\vec{J}^x \approx \sum_n \omega_n \vec{A}(\Omega_n) \sum_t \omega_t^\perp \left[\frac{x_t^m - x_c}{x^*} (\psi_t^{in} - \psi_t^{out}) - \frac{l_t \Omega_{x,n}}{x^*} \underbrace{\left(\frac{\psi_t^{in} + \psi_t^{out}}{2} - \langle \psi \rangle_t \right)}_{\Delta\psi_t} \right].$$

The $\Delta\psi_t$ is the difference between a sort of flux geometrical average and a physical one (i.e., which satisfies the neutron balance) along the chord. It can be written as follows using Eq. 4.17:

$$\begin{aligned} \Delta\psi_t &= \left(\frac{1}{2} - \frac{1}{\tau_t} \right) \psi_t^{in} + \left(\frac{1}{2} + \frac{1}{\tau_t} \right) \psi_t^{out} - \mathcal{A}_t \\ &= \left(\frac{1}{2} - \frac{1}{\tau_t} \right) \psi_t^{in} + \left(\frac{1}{2} + \frac{1}{\tau_t} \right) [\psi_t^{in}(1 - \beta_0(\tau_t)) + \mathcal{A}_t \beta_0(\tau_t) + \mathcal{B}_t \xi(\tau_t)] - \mathcal{A}_t \\ &= \left[1 - \left(\frac{1}{2} + \frac{1}{\tau_t} \right) \beta_0(\tau_t) \right] \psi_t^{in} + \left[\left(\frac{1}{2} + \frac{1}{\tau_t} \right) \beta_0(\tau_t) - 1 \right] \mathcal{A}_t + \left(\frac{1}{2} + \frac{1}{\tau_t} \right) \xi(\tau_t) \mathcal{B}_t \\ &= \xi(\tau_t) \psi_t^{in} - \xi(\tau_t) \mathcal{A}_t + \left(\frac{1}{2} + \frac{1}{\tau_t} \right) \xi(\tau_t) \mathcal{B}_t, \end{aligned}$$

4.24

where we used the definitions of $\xi(\tau_t)$, \mathcal{A}_t , and \mathcal{B}_t .

In practice, the linear streaming term is not assembled chord-by-chord. Instead, we rewrite it as

$$-\Delta\vec{J}^x \approx \underbrace{\sum_n \omega_n \vec{A}(\Omega_n) \sum_t \omega_t^\perp \left[\frac{x_t^m - x_c}{x^*} (\psi_t^{in} - \psi_t^{out}) \right]}_{-\Delta\vec{J}_{1b}^x} - \underbrace{\sum_n \omega_n \vec{A}(\Omega_n) \sum_t \omega_t^\perp \frac{l_t \Omega_{x,n}}{x^*} \Delta\psi_t}_{\Delta\vec{J}_{2b}^x},$$

and we note that only $\Delta\vec{J}_{1b}^x$ contains chord terms that are dependent on x . Therefore, $\Delta\vec{J}_{2b}^x$ can be computed more cheaply by expanding the product $\vec{A}\Omega_x$ in terms of spherical harmonics (see [16] for more details):

$$\Delta\vec{J}_{2b}^x = -\frac{\mathbb{Z}^x}{x^*} \Delta\vec{\Psi},$$

where $\Delta\vec{\Psi}$ is the array of moments of the angular discrete function $\sum_t \omega_t^\perp l_t \Delta\psi_t$ up to order $N'_m = N_m + L + 2$, while \mathbb{Z}^x is the matrix of the coefficients of the linear expansion in terms of spherical harmonics **Erreur ! Source du renvoi introuvable..**

To summarize, the linear balance equations can be therefore written as follows:

$$\begin{aligned} \vec{\phi}_C^x &= \frac{1}{\Sigma} \mathbb{A} \vec{Q}_C^x - \frac{1}{\Sigma V} \Delta\vec{J}_{1b}^x - \frac{1}{\Sigma V} \frac{\mathbb{Z}^x}{x^*} \Delta\vec{\Psi}, \\ \vec{\phi}_C^y &= \frac{1}{\Sigma} \mathbb{A} \vec{Q}_C^y - \frac{1}{\Sigma V} \Delta\vec{J}_{1b}^y - \frac{1}{\Sigma V} \frac{\mathbb{Z}^y}{y^*} \Delta\vec{\Psi}. \end{aligned}$$

4.25

We conclude this theoretical presentation by noticing that both Eqs. 4.21 and 4.25 give conservative averages of the flux spatial moments that are coherent with the computed currents but that are not numerically coherent with the transmission equation. This matter is discussed in detail in [16].

4.2.6 Enforce conservation in LSxy

Similarly to what is done in the classic LS scheme, the free parameters $\overline{\delta\phi^1}$ and $\overline{\delta\phi}^{xy}$ must be defined in such a way that the LS-xy scheme is conservative.

Constant moments

It must be $\vec{\phi}_G^1 = \vec{\phi}_C^1$ in all regions, so from Eq. 4.18 it is

$$\overline{\delta\phi^1} = \vec{\phi}_C^1 - \sum_{\alpha \in \partial D_i} \mathbb{M}_\alpha \vec{\phi}_\alpha.$$

Note that, unsurprisingly, the constant flux correction is very similar to the one found for the standard LS scheme.

Linear moments

It must be $\vec{\phi}_G^x = \vec{\phi}_C^x$ and $\vec{\phi}_G^y = \vec{\phi}_C^y$ in all regions, so from Eq. 4.20 it is

$$\begin{bmatrix} \overline{\delta\phi^x} \\ \overline{\delta\phi^y} \end{bmatrix} = \begin{bmatrix} \mathbb{M}_V^{x,x} & \mathbb{M}_V^{x,y} \\ \mathbb{M}_V^{y,x} & \mathbb{M}_V^{y,y} \end{bmatrix}^{-1} \left(\begin{bmatrix} \vec{\phi}_C^x \\ \vec{\phi}_C^y \end{bmatrix} - \sum_\alpha \begin{bmatrix} \mathbb{M}_\alpha^x \vec{\phi}_\alpha \\ \mathbb{M}_\alpha^y \vec{\phi}_\alpha \end{bmatrix} \right).$$

Note that \mathbb{M}_V does not depend on the iteration index, so it can be inverted (i.e., LU-factorized) once at initialization and then reused.

4.3 Some selected results

We validated and benchmarked the newly developed LS-xy method on different test cases. While a more extended discussion of the obtained results is given in [16], we limit here our presentation to only one significant case.

The layout of this case is given in Fig. 4.2 and it is a typical 17 by 17 UOX assembly with B₄C control rods inserted. It is known for being a challenging test case as it is characterized by strong local flux gradients. We ran for this case a reference Monte Carlo calculation with TRIPOLI-4[®] adopting the CEAV512 nuclear data library (JEFF3.1.1) and obtained a $k_{eff} = 0.65359 \pm 1.7$ pcm (1 σ). Statistical errors for pinwise one group reaction rates are well below 1%, and we used in the following these results to benchmark our deterministic calculations.

Regarding the TDT calculations, we used the 281 groups energy mesh SHEM library (based on JEFF3.1.1), an anisotropy order of 3, a number of azimuthal angles equal to 36 (uniformly distributed), and 5 (Bickley-Naylor) polar angles, with a transversal integration step equal to 0.01 cm (quite refined indeed). The rest of computational or material data necessary to reproduce these calculations can be found in [16].

These calculations have been carried out using the AP3-2.2.r17497 revision of the APOLLO3[®] code and the 4.11.1 version of the Monte Carlo TRIPOLI-4^s code.

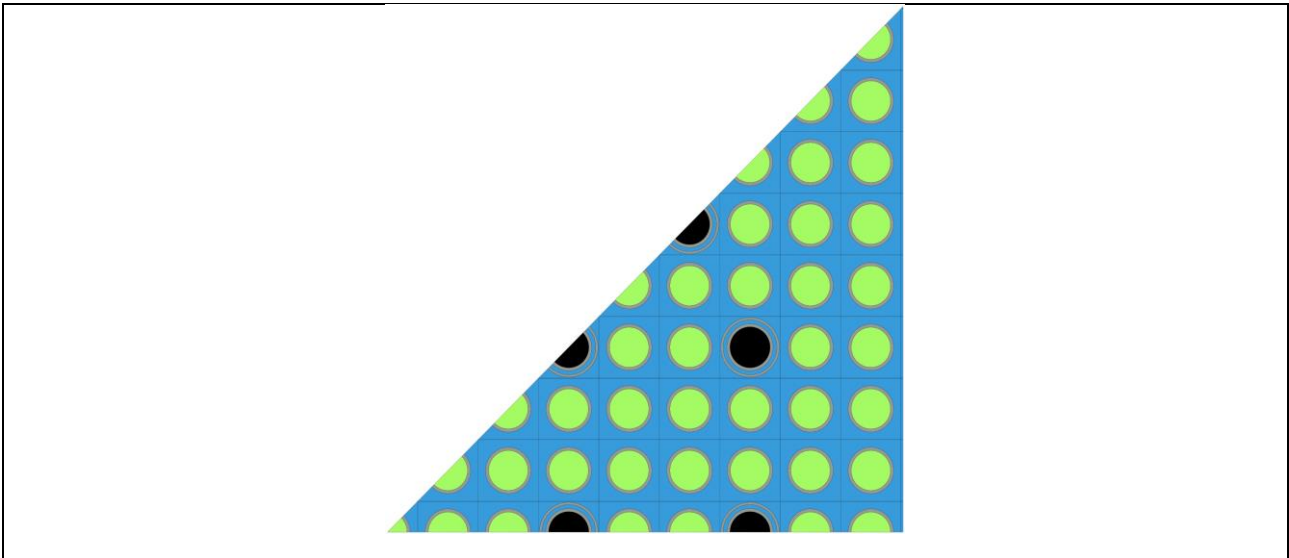


Figure 4.2: UOX assembly - Problem domain: UOX fuel pins in green; fuel clads and guide tubes in dark gray; B₄C control rods in black; and borated water in blue.

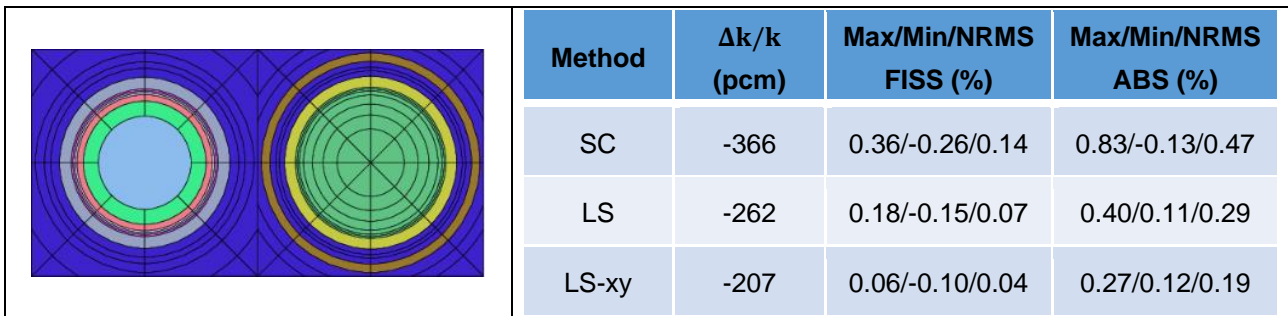


Figure 4.3: First set of calculations with a mesh constituted by 3325 computational regions. Reference calculation is a TRIPOLI-4[®] continuous energy calculation. This is a less refined mesh necessary to obtain a maximal error for SC inferior to 1%.

In Fig. 4.3 we reported the mesh (for the fuel and the rod pin) adopted for the first set of calculations and a synthetic sketch of the results. This mesh consists of a global number of computational regions equal to 3325, and it is the coarsest mesh we found that is able to reduce the SC maximal error to less than 1%. Note that even that, with this mesh the error on the reactivity remains of 366 pcm, quite larger than those obtained with both the LS and (even better) the LS-xy methods. Remark that the required memory for the SC method is 37Mbytes and the computational time is of 1154 s.

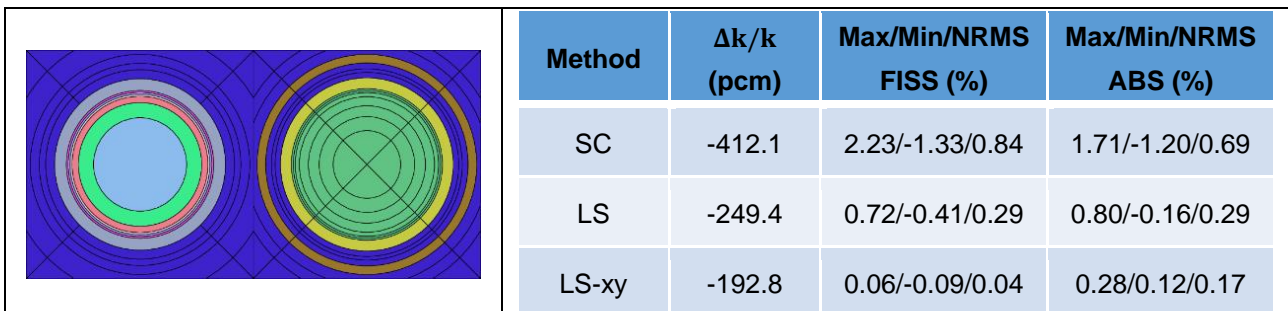


Figure 4.4: Second set of calculations with a mesh constituted by 1195 computational regions. Reference calculation is a TRIPOLI-4[®] continuous energy calculation. This is a less refined mesh necessary to obtain a maximal error for LS inferior to 1%.

In a second batch of results we present, we adopted a computational mesh constituted by 1195 whose plot is in the Fig. 4.4. This mesh is the coarsest one we found that is able to maintain the computational pin-wise maximal error of the LS method lower than 1%. Note that the computational time necessary to run this LS calculation is of 3730 s. So quite superior to the previous SC one, but the case of Fig. 4.4 still has a lower error on reactivity (130pcm better) and a Normalized Root Mean Square (NRMS) error significantly lower (0.29 against 0.47).

Finally, we present in Fig. 4.5 a computational mesh of only 565 regions that is well adapted to the LS-xy scheme. Note before all that the maximum computational error per pin is still well below 1% (equal in fact to 0.33% that is largely better than that of the previous optimal meshes for SC and LS methods). Moreover, the error on reactivity is only slightly degraded with respect to the reference LS-xy, since we have here an error of only 20 pcm. Note also that the memory necessary to this calculation is of 38 Mbytes (so very similar to the one of the Fig. 4.3) and the computational time is only of 690 s.

In conclusion, this case shows very encouraging results since the LS-xy method is able to maintain a strong precision even with almost “material” meshes. Looking to an optimal choice between costs and precision, it seems a very competitive choice. We think also that for all these kinds of studies where the engineers do not seek to optimize computational times but need to correctly predict the neutronic behavior of some innovative system, with great precision, but would like to reduce the time needed to validate their results, the choice of the LS-xy is to be recommended since it does not need to tune aggressively the computational mesh as it is the case of the standard SC, or in minor measure of the LS.

In the next future we plan to implement an acceleration technique to permit the full industrial deployment of this new approach.

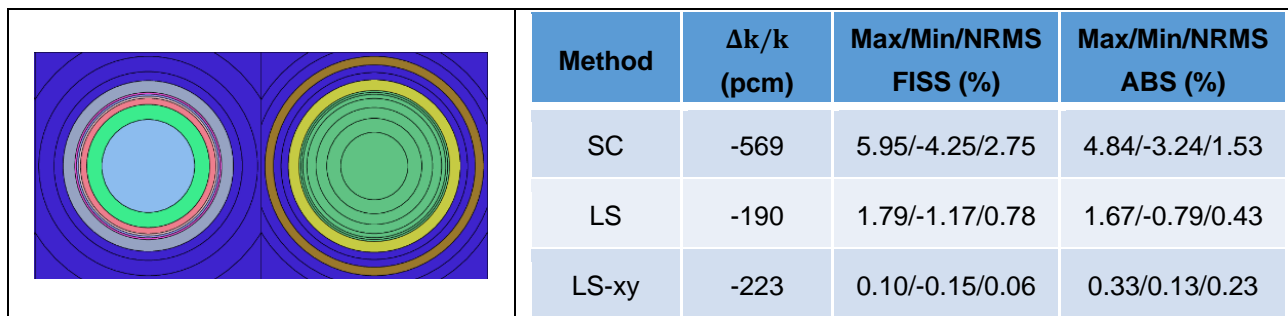


Figure 4.5: Second set of calculations with a mesh constituted by 565 computational regions. Reference calculation is a TRIPOLI-4[®] continuous energy calculation. This is a less refined mesh necessary to obtain a maximal error for LS-xy inferior to 1%.

5 Conclusions

In Task 4.4 of the CAMIVVER project, we have developed new computational methods and implemented advanced modeling using the lattice part of the APOLLO3[®] code.

The first subject we have faced is the improvement of the axial reflector modeling along depletion. This item demands the development of a 3D computational method to correctly represent the flux in the case of interest. To follow the behavior of the nuclide density during depletion, we have enhanced the previously developed polynomial flux method to include also the spatial variation of the cross sections [5]. Since the depletion calculation is organized as a coupling between different methods (i.e., the self-shielding and the depletion with the flux calculation) we have organized a framework to exchange the information between the “polynomial” MOC solver and the “Step-based” basic APOLLO3[®] functionalities (in particular self-shielding and depletion). Here, we have shown that, in spite of a supposed “step-wise” representation, a Gaussian representation can be used to optimally exchange. Moreover, we have established a method to validate our approach against Monte-Carlo calculation during depletion. We have in fact avoided to perform Monte-Carlo depletion calculations due to excessive computational costs. We have therefore preferred to use the APOLLO3[®] function called Triage to “translate” the set of nuclide concentrations at each burnup step and then verify the coherence between the Monte-Carlo calculation and the deterministic one. Nevertheless, we still have had to manage the fact that at every depletion snapshot the deterministic Gaussian mesh cannot be directly translate for the TRIPOLI-4[®] calculation. Therefore, a new tool to build an optimal Step Equivalent Mesh (SEM) has been conceived. We have then run a complete validation scenario. Our results are encouraging even if some discrepancies are still to be analyzed and resolved. In particular, our SEM is certainly too large and demands to be tuned. This setup will be addressed in next future.

Another important topic we have addressed in this task, is to build some advanced reflector models in order to analyze some approximations of classical schemes. Therefore, after having established a referential APOLLO3[®] calculation of the KAIST-derived benchmark with curve reflector and tested it against TRIPOLI-4[®] calculations, we have quantified the errors that affect some of the typical approaches in the computational model of the reflector. In particular, we have examined the weight of the smearing of water holes into a homogeneous reflector medium, the geometrical deformation of the correct reflector model into a segmented Cartesian or the use of enhanced self-shielded models. Our conclusion is that, even if these approximations do not entail strong errors in the global reactivity, they cause important local errors (up to 4%) in pin-by-pin reaction rates at the interface between the core and the reflector. We suggest therefore the improvement of classical models by using local equivalence techniques (like discontinuity factors based on peripheral cluster calculation as it is done in literature) or by a strong improvement of the geometrical model. This last possibility has of course as a consequence to accept a higher computational cost. We remark also that using the LS scheme in the APOLLO3[®] MOC solver has been the only operative option to assess our reference calculation. This has permitted us to eliminate the lack of spatial convergence in the computational mesh that we otherwise had with the standard SC scheme.

Finally, the last subject we have tackled is the development of an enhanced numerical scheme for neutron transport. The goal of this sub-task was to improve the pre-existing LS

scheme to allow using even coarser computational meshes. This could be profitable for industrial applications for two main reasons. On one side, we expect the new scheme to be faster (for a given precision) of the previous LS one. On the other hand, higher order schemes are largely easier to handle to the users since they permit to obtain converged results without the need to do tedious convergence studies. This new scheme inserts into the previous LS one the concept of interpolating not only by conserving surface quantities but also volume-based ones. We have largely compared this method to the LS and the SC schemes in a rodged assembly case test and our tests show the large superiority of this new scheme with respect to the already available ones. To complete the development and allow to use it in industrial applications, we still need to implement an acceleration scheme. Thing that we plan to do in the next future.

6 References

- [1] D. Verrier et al., "Codes and Methods Improvements for VVER Comprehensive Safety Assessment: The CAMIVVER H2020 Project," in Proceedings of the ICONE-28 International Conference on Nuclear Engineering, Online, 2021.
- [2] P. Mosca, L. Bourhrara, A. Calloo, A. Gammicchia, F. Goubioud, L. Lei-Mao, F. Madiot, F. Malouch, E. Masiello, F. Moreau, S. Santandrea, D. Sciannandrone, I. Zmijarevic, E. Garcias-Cervantes, G. Valocchi, J. Vidal, F. Damian, P. Laurent, A. Willien, A. Brighenti, L. Graziano and B. Vezzoni, "APOLLO3®: Overview of the new code capabilities for reactor physics analysis," in Int. Proc. M&C 2023 Conference, Niagara Falls, Ontario, Canada, August 13-17, 2023.
- [3] S. Santandrea, D. Sciannandrone, R. Sanchez, L. Mao, L. Graziano, , « A Neutron Transport Characteristics Method for 3D Axially Extruded Geometries Coupled with a Fine Group Self-Shielding Environment », Nuclear Science and Engineering, 186, pp. 239-276, 2017.
- [4] S. Santandrea L. Graziano, D. Sciannandrone, "Accelerated polynomial axial expansions for full 3D neutron transport MOC in the APOLLO3® code system as applied to the ASTRID fast breeder reactor », Annals of Nuclear Energy, 113, pp. 194-236, 2017.
- [5] A. Gammicchia, S. Santandrea, S. Dulla, "Cross sections polynomial axial expansion within the APOLLO3® 3D characteristics method" , Annals of Nuclear Energy, 165, 2022
- [6] A. Gammicchia, P Mosca, S. Santandrea "Calcul déterministe direct d'un cœur REL en fonctionnement avec le code APOLLO3® utilisant plusieurs techniques d'accélération du calcul", DES/ISAS/DM2S/SERMA/LLPR/NT/2022-70634/A.
- [7] G.I. Bell, S. Glasstone, Nuclear Reactor Theory, Van Nostrand Reinhold, New York USA,1970.
- [8] D. Sciannandrone, S. Santandrea, R. Sanchez, « Optimized tracking strategies for step MOC calculations in extruded 3D axial geometries ».
- [9] S. Santandrea, « An Integral Multidomain DPN Operator as Acceleration Tool for the Method of Characteristics in Unstructured Meshes », Nuclear Science and Engineering, 155, pp. 223-235, 2007.
- [10] Willien, A. and Vezzoni, B. 11/02/2021. D4.3 – Definitions of tests cases for the verification phases of the multi-parametric library generator. Version 1. CAMIVVER. H2020.
- [11] D. Tomatis et al. (2022), "Overview of SERMA's Graphical User Interfaces for Lattice Transport Calculations", Energies 2022, 15, 1417.
- [12] Nam Zhi Cho, Benchmark Problem 1A: MOX Fuel-Loaded Small PWR Core (MOX Fuel with Zoning), <http://nurapt.kaist.ac.kr/benchmark>.
- [13] Igor Zmijarevic, Two-dimensional PWR minicore model for transport calculations, Revision 1, 2020.
- [14] « Implementation of a CRAM solver in MENDEL Depletion Code System», S. Lahaye, et al., M&C – 2017, Apr 2017, Jeju, South Korea.
- [15] S. Santandrea and P. Mosca, « Linear surface characteristic scheme for the neutron transport equation in unstructured geometries », Physor2006, Vancouver, Canada.

- [16] M. Tiberghien and S. Santandrea " A Novel High-Order Surface Characteristics Scheme for the Neutron Transport Equation in 2D Unstructured Meshes", accepted for publication in Nuclear Science and Engineering.
- [17] Santamarina, A., Hfaiedh, N., 2007. The SHEM energy mesh for accurate fuel depletion and BUC calculation. In: Proc. Int Conf. Nuclear Criticality Safety ICNC” 2007, Saint Petersburg, Russia.
- [18] Cheng Zhang, Chenghui Wan, Liangzhi Cao, Yunzhao Li, Ning Xu, Hongchun Wu, Method research and engineering validation of the improved homogenization for the heavy reflector in VVER, Annals of Nuclear Energy, Volume 173, 2022, <https://doi.org/10.1016/j.anucene.2022.109119>.
- [19] Ville Valtavirta, Antti Rintala, Unna Lauranto, Pin power reconstruction for hexagonal geometry in nodal neutronics program Ants, Annals of Nuclear Energy, Volume 179, 2022, <https://doi.org/10.1016/j.anucene.2022.109384>.
- [20] Julien Taforeau, Marc Muller, Vivian Salino, Modeling of heavy reflectors using DONJON-5, Annals of Nuclear Energy, Volume 127, 2019, Pages 319-325, <https://doi.org/10.1016/j.anucene.2018.12.017>.
- [21] CASMO presentation in CAMIVVER seminary, 3-5 July 2023, Karlsruhe, Germany.
- [22] E. Brun et al., TRIPOLI-4®, CEA, EDF and AREVA reference Monte Carlo code, Annals of Nuclear Energy, Volume 82, 2015, Pages 151-160.

7 Appendix A: Contribution to KAIST-like core preliminary analyses using newly developed Python libraries for automatize ALAMOS use

To improve the model used for reflectors in preparation to the CAMIVVER follow-up project, several activities were carried out at Framatome using the tools and the approaches implemented in CAMIVVER WP4 and WP5.

Two internships' projects started in 2023 aiming at automatizing the creation of geometries for lattice calculations based on the ALAMOS tool [11] using Python libraries. The outcomes of these works may be used to support reference studies (R&D actions in Framatome) and to produce advanced geometry configurations (2D reflectors vs. typical 1D models) to generate improved cross-section data for core calculations.

The two internships' projects focus on the development of different Python libraries wrapping the ALAMOS tool to:

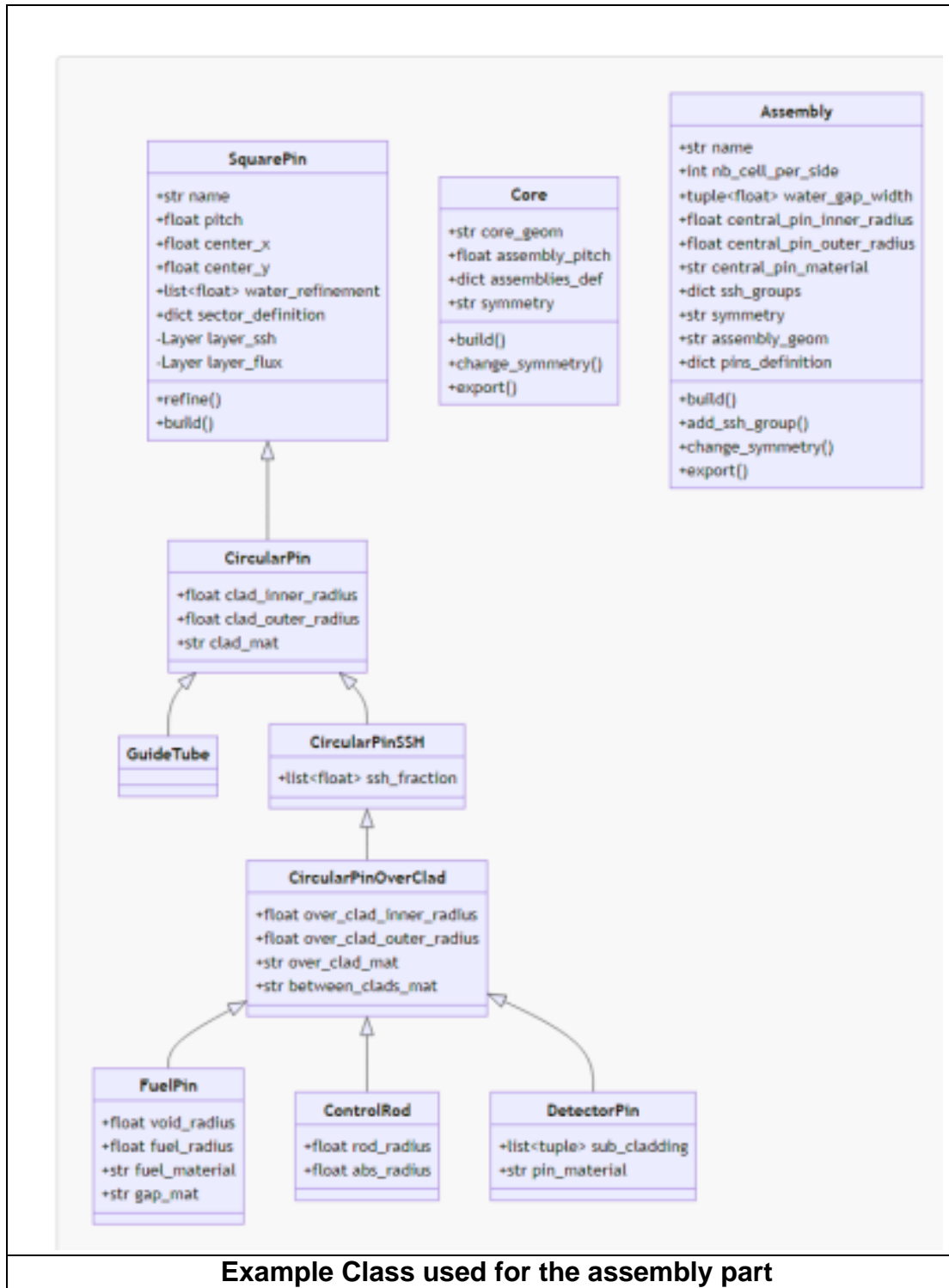
1. generate PWR Cartesian unstructured Fuel Assembly (FA) geometries. The idea is to produce, as for the VVER cases, external geometries for PWR FA to be used in the NEMESI environment (work done by Mathieu Robin in collaboration with Université de Grenoble – PHELMA - France).
2. generate PWR and VVER unstructured reflectors (mainly radial) geometries as first step to prepare improved reflector cross-sections to be used at core level and feeding reference 2D calculations (work done by Fabio Inzirillo in collaboration with Politecnico di Milano - Italy and Polytechnique Montreal - Canada).

In this appendix, only few elements concerning these works are presented to open the discussion in preparation of the CAMIVVER project follow-up. The activities are still ongoing.

In both activities, the choice of developing high-level Python based libraries, to generate unstructured geometries (Cartesian and Hexagonal assembly and reflectors geometries), were carried out by considering since the beginning several needs, such as

- automatization to produce all geometry types in the framework of the development and extension of the multiparameter platform (NEMESI),
- applications to improve existing modeling (e.g., for reflectors going from 1D to 2D) and support V&V actions (e.g., via the setup of 2D reference core calculations for the different reactor types).

To achieve these goals, considerations over the architectural choice and the User Interface were considered and several generic classes were created as shown, for instance, in Figure A.2 for the assembly and reflector parts, respectively.



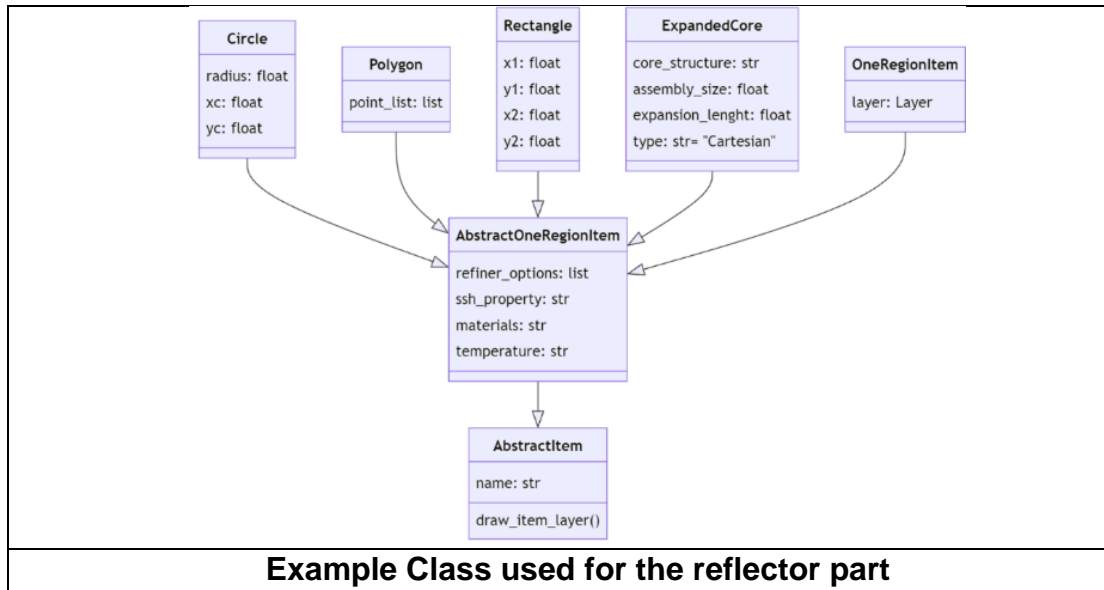


Figure A.2: Example classes organization (Activity still ongoing)

The Python libraries developed during the internships allowed to start the automatization of the generation of the PWR assembly geometry (i.e., the ones composing the KAIST core, see Figure A.3) and for any type of reflector geometries.

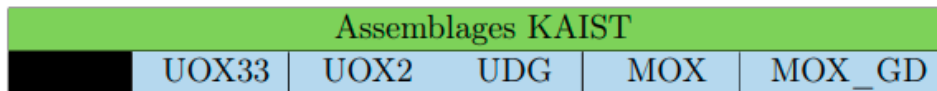


Figure A.3: KAIST FA TYPES

In order to create a full core model, the two Python libraries were combined and a first application to the KAIST-like core described in [12] was performed as indicated in the example shown in Figure A.4.

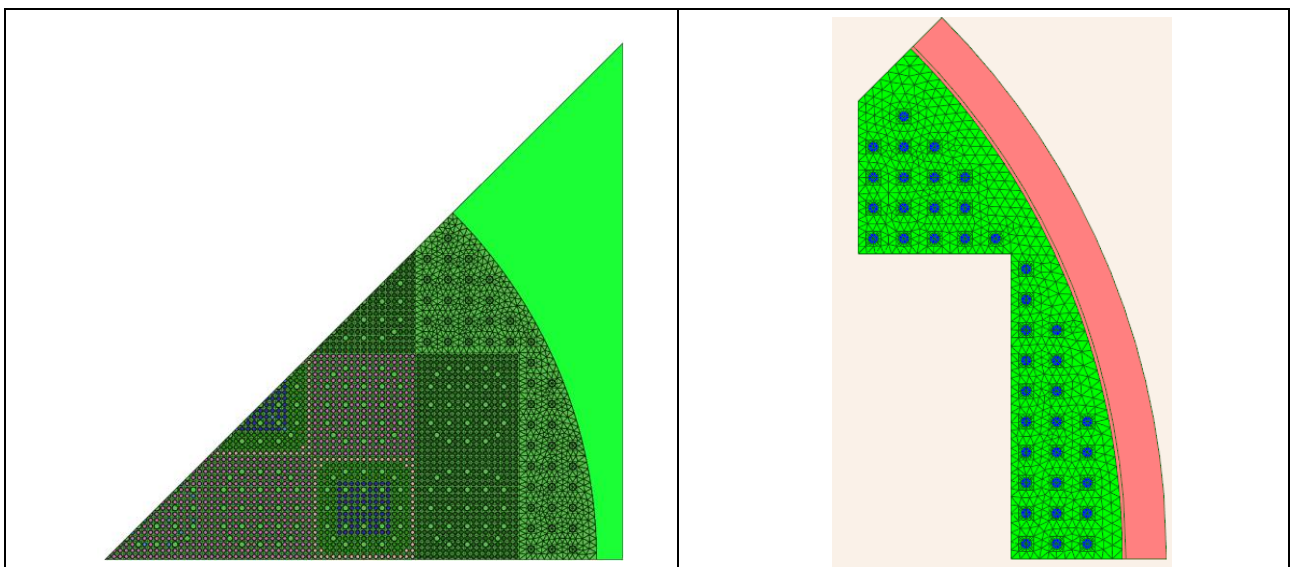


Figure A.4: Example KAIST-like core generated with Python library – ongoing work.

Preliminary results obtained are encouraging. A comparison with the results described in Section 0 is provided in Figure A.5.

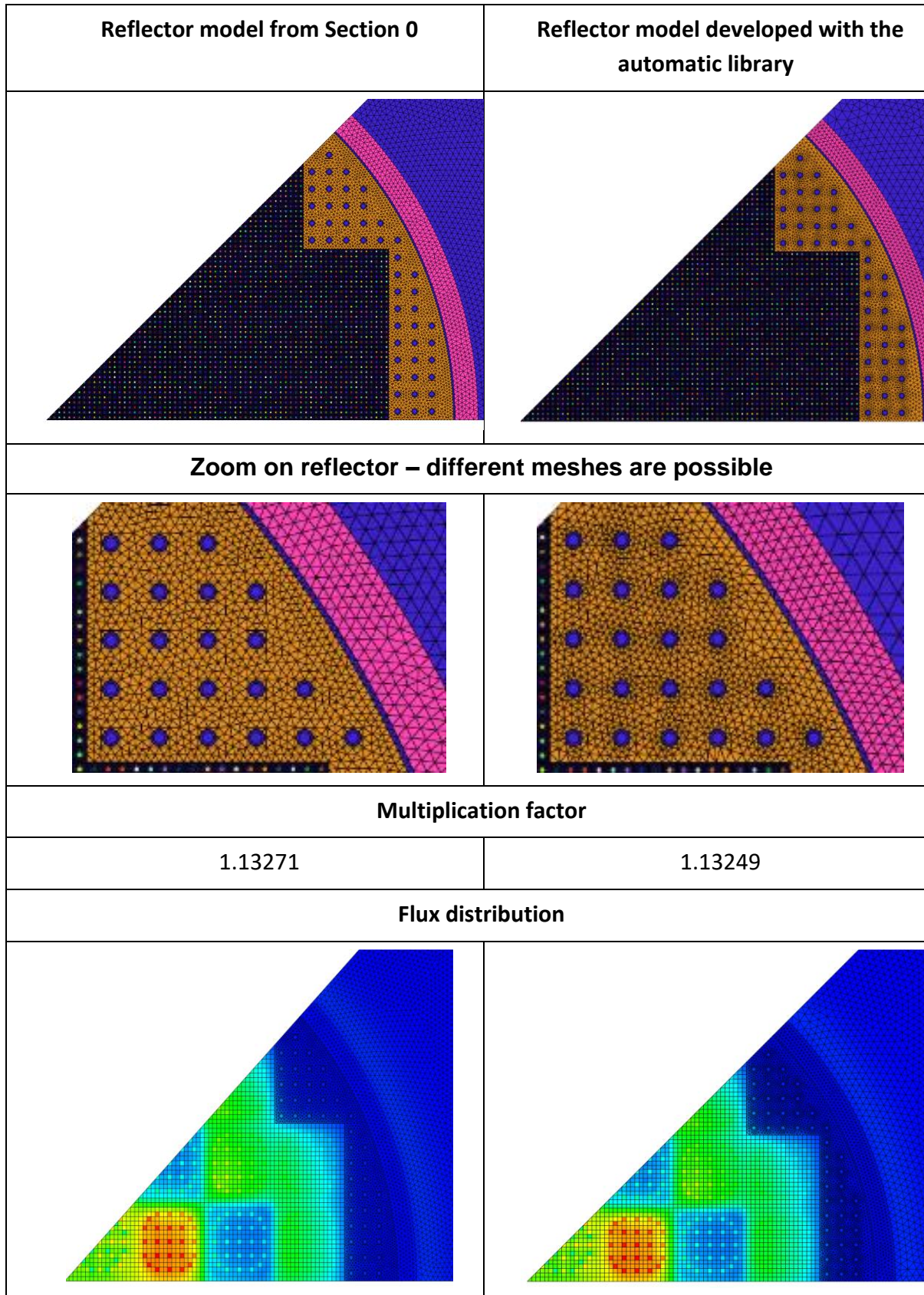


Figure A.5: Kaist-like preliminary results

8 APPENDIX B – Validation MOC3D: pin by pin reaction rates

Here, we put all 2D plots with the pin by pin distribution of reaction rates: for both fission and capture, for all BU steps and all layers (except the non-fissile layers where the fission rates are absent of course).

12.1 Burnup = 0 MWd/t

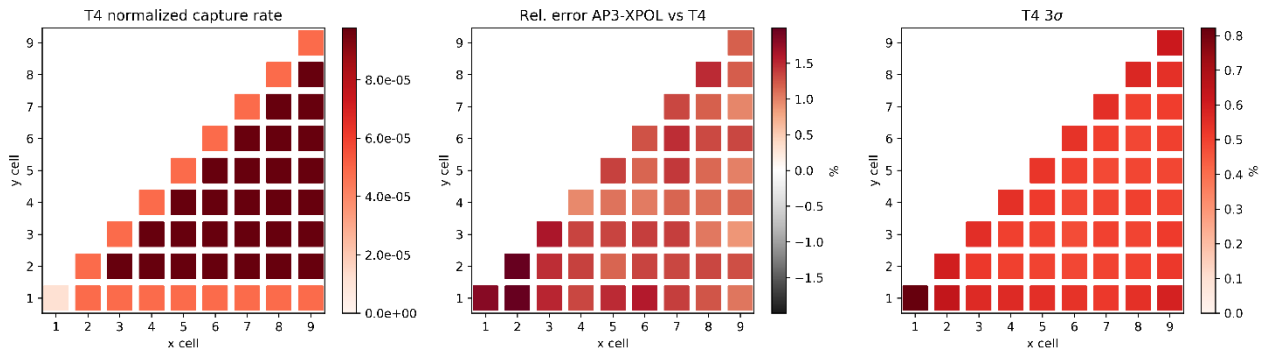


Figure B.1: Layer 1 comparison with TRIPOLI-4® for the capture rate

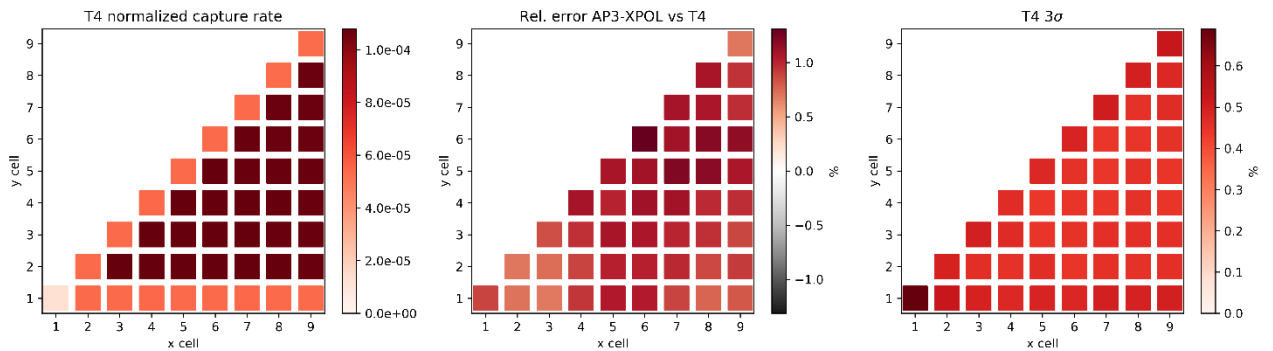


Figure B.2: Layer 2 comparison with TRIPOLI-4® for the capture rate

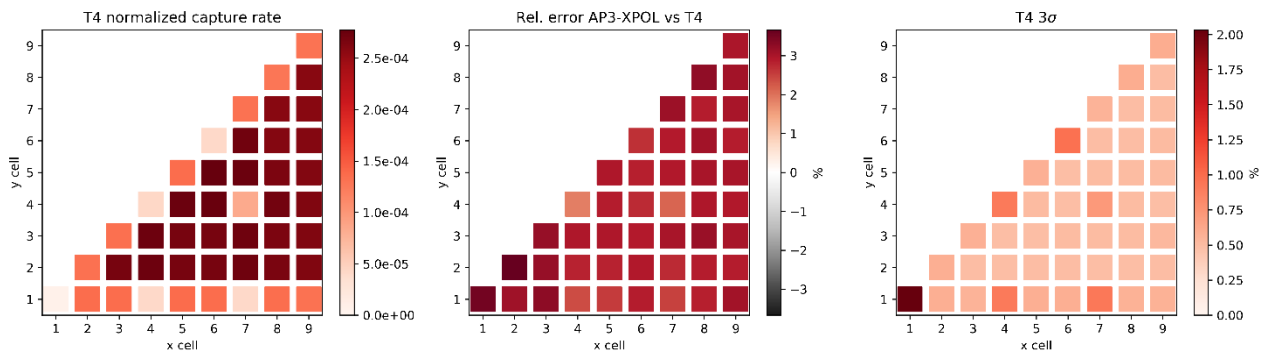


Figure B.3: Layer 3 comparison with TRIPOLI-4® for the capture rate

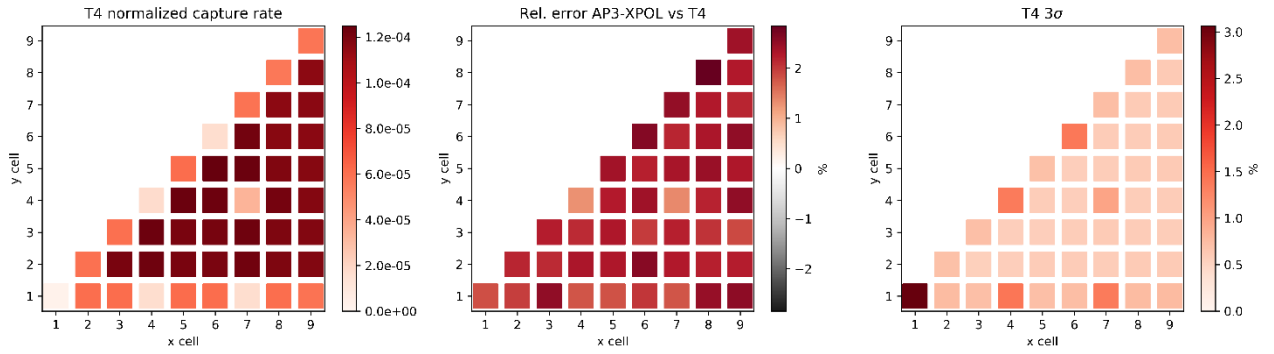


Figure B.4: Layer 4 comparison with TRIPOLI-4® for the capture rate

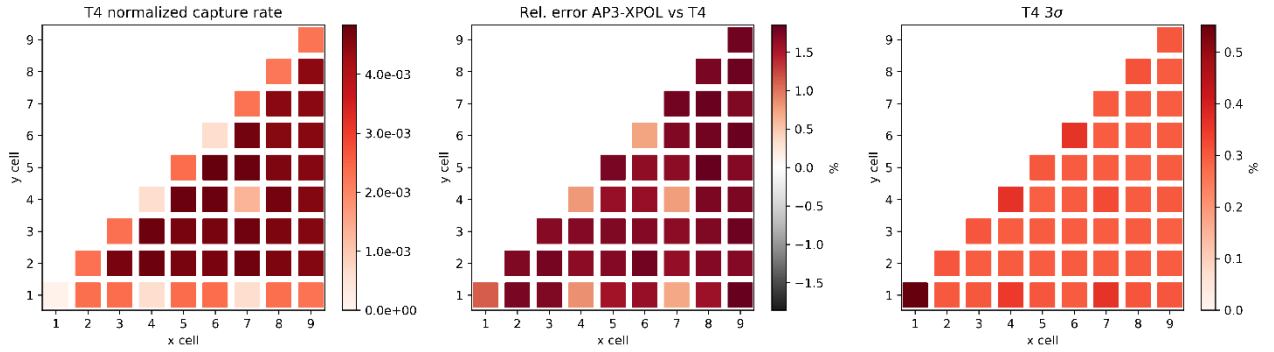


Figure B.5: Layer 5 comparison with TRIPOLI-4® for the capture rate

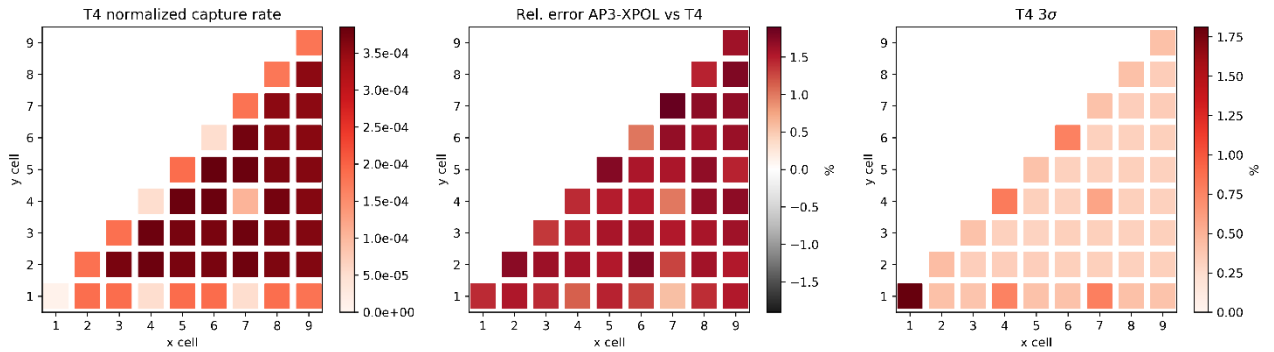


Figure B.6: Layer 6 comparison with TRIPOLI-4® for the capture rate

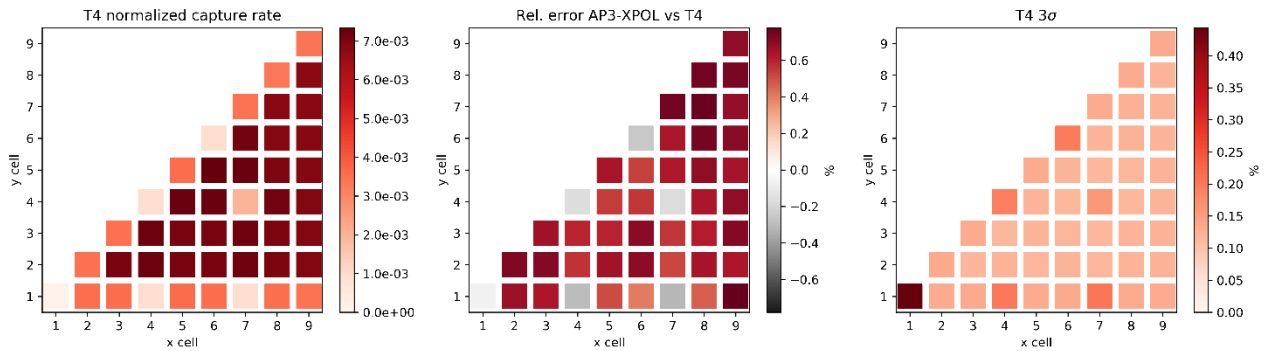


Figure B.7: Layer 7 comparison with TRIPOLI-4® for the capture rate



Figure B.8: Layer 8 comparison with TRIPOLI-4[®] for the capture rate

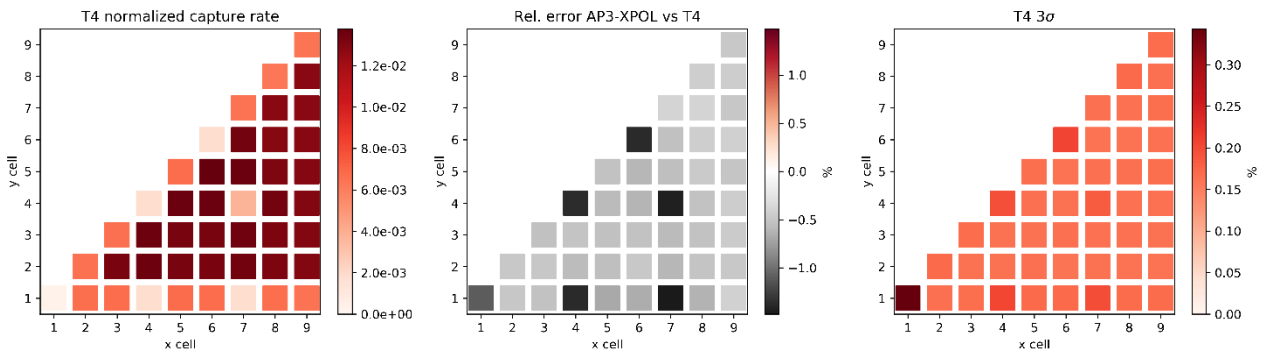


Figure B.9: Layer 9 comparison with TRIPOLI-4[®] for the capture rate

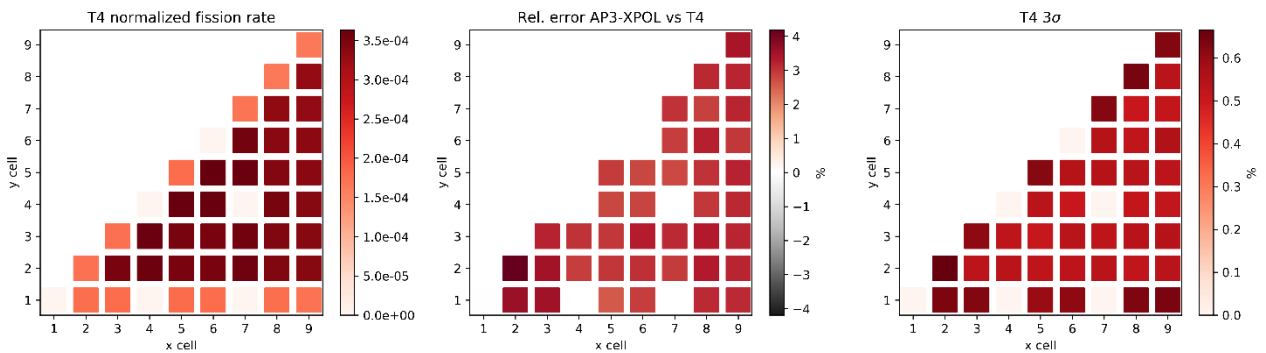


Figure B.10: Layer 3 comparison with TRIPOLI-4[®] for the fission rate

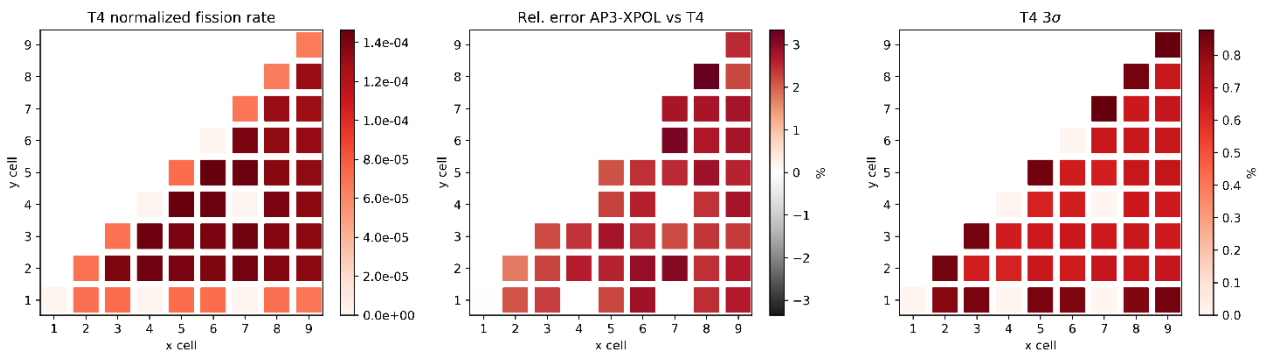


Figure B.11: Layer 4 comparison with TRIPOLI-4[®] for the fission rate

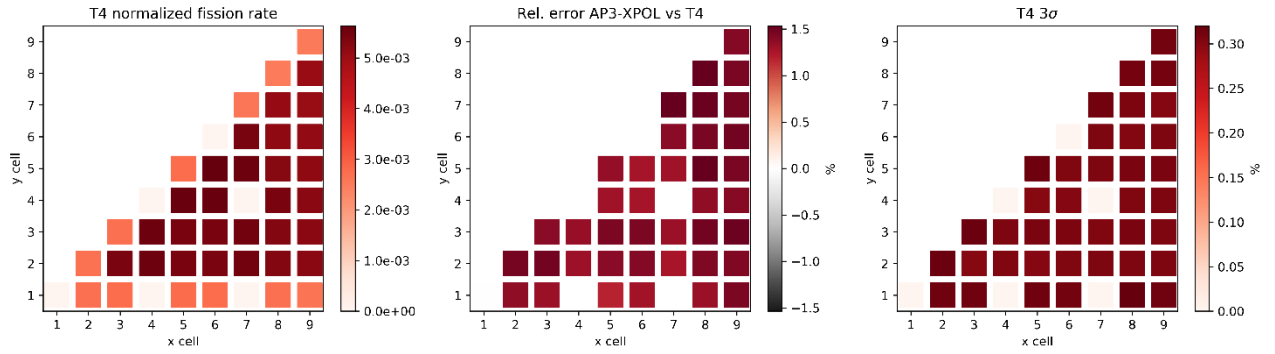


Figure B.12: Layer 5 comparison with TRIPOLI-4® for the fission rate

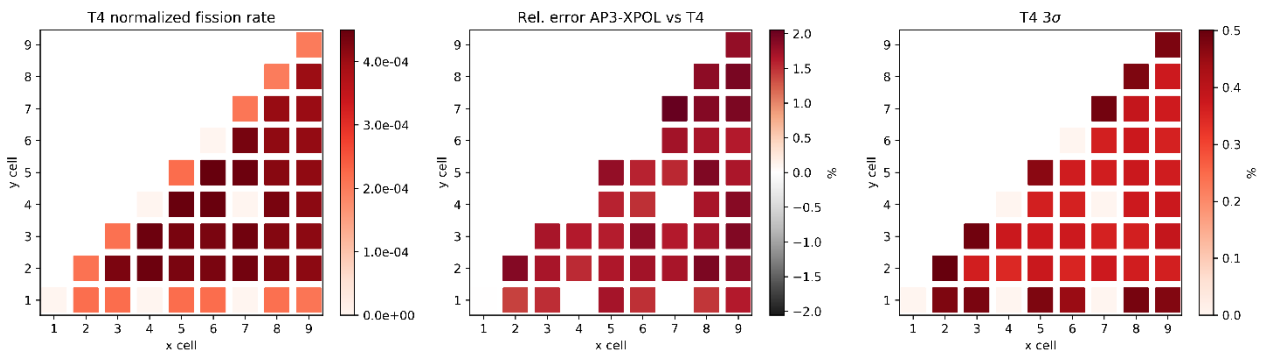


Figure B.13: Layer 6 comparison with TRIPOLI-4® for the fission rate

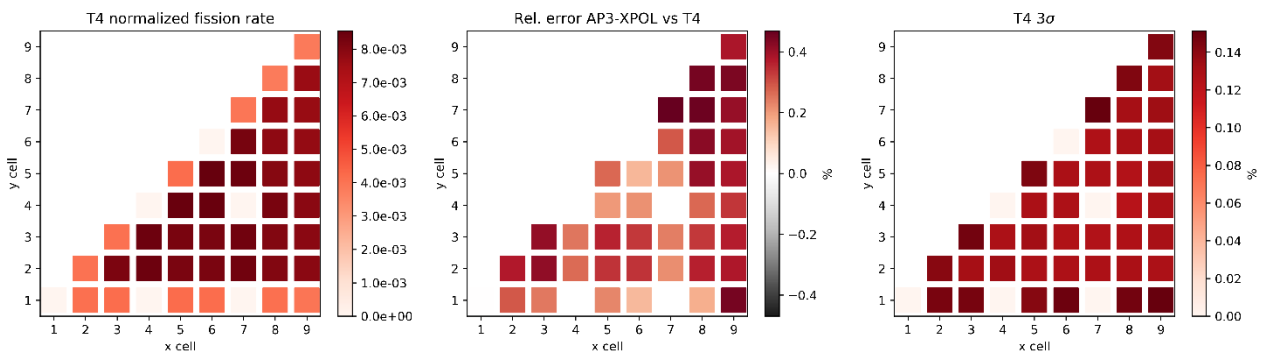


Figure B.14: Layer 7 comparison with TRIPOLI-4® for the fission rate

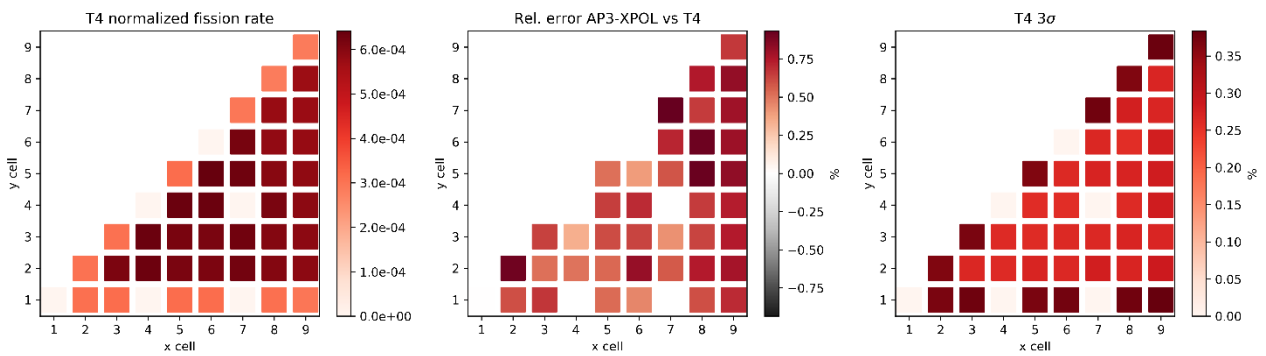


Figure B.15: Layer 8 comparison with TRIPOLI-4® for the fission rate

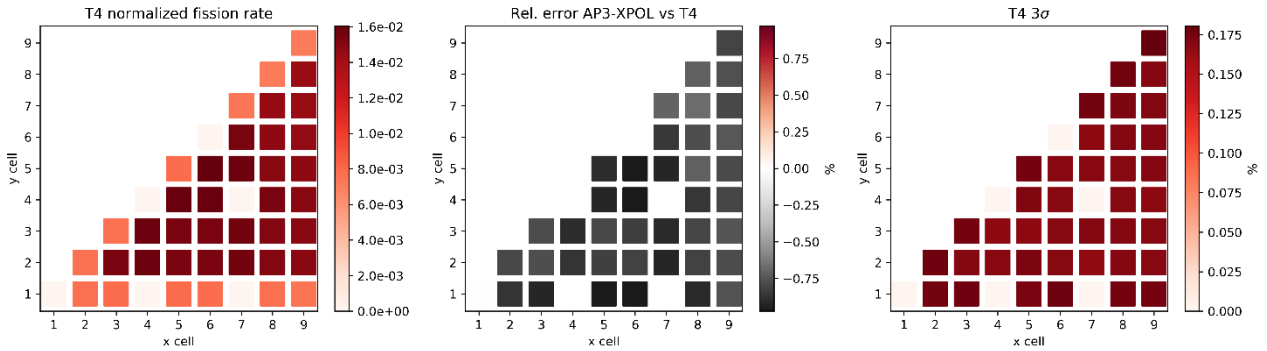


Figure B.16: Layer 9 comparison with TRIPOLI-4® for the fission rate

12.2 Burnup = 60 GWd/t

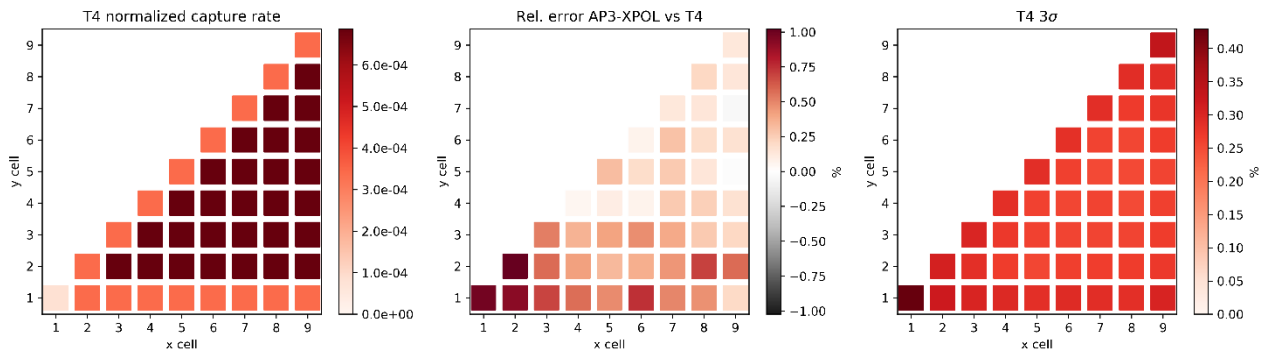


Figure B.17: Layer 1 comparison with TRIPOLI-4® for the capture rate

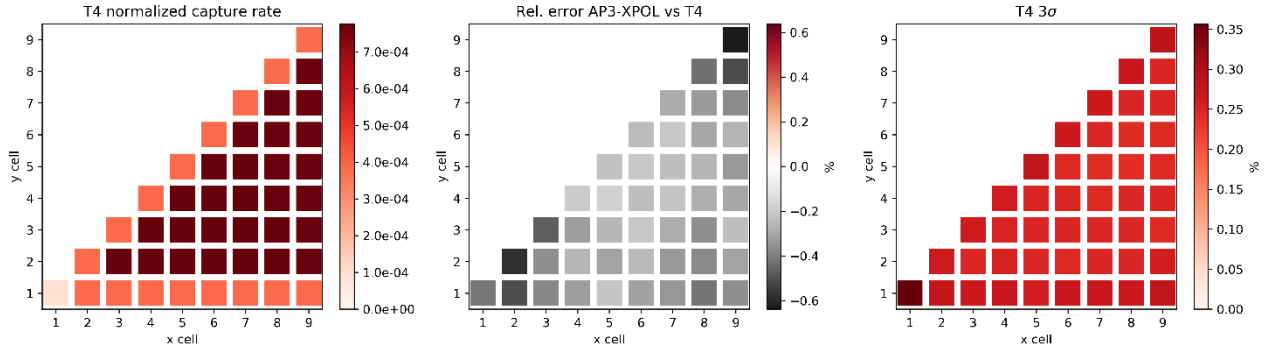


Figure B.18: Layer 2 comparison with TRIPOLI-4® for the capture rate

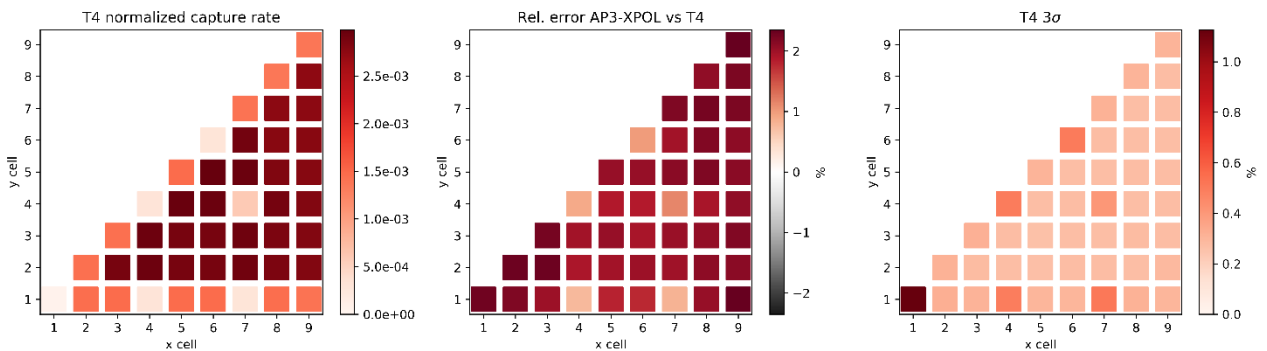


Figure B.19: Layer 3 comparison with TRIPOLI-4® for the capture rate

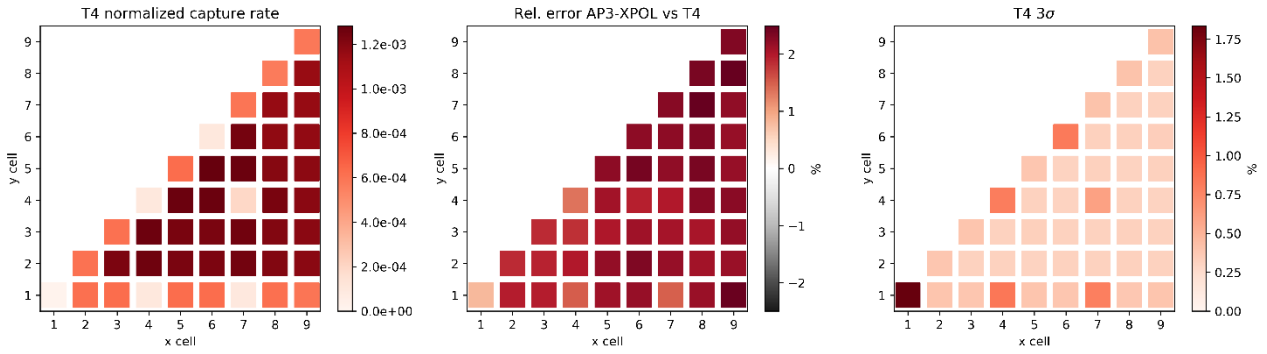


Figure B.20: Layer 4 comparison with TRIPOLI-4® for the capture rate

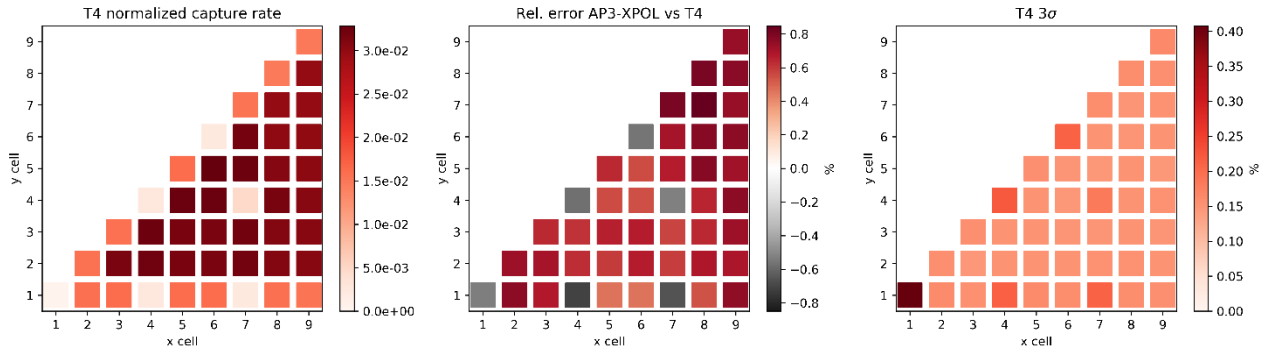


Figure B.21: Layer 5 comparison with TRIPOLI-4® for the capture rate

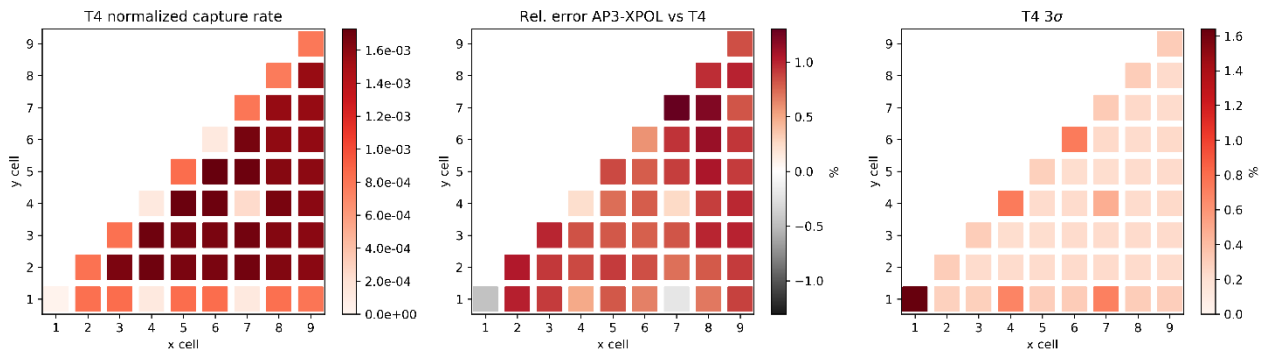


Figure B.22: Layer 6 comparison with TRIPOLI-4® for the capture rate

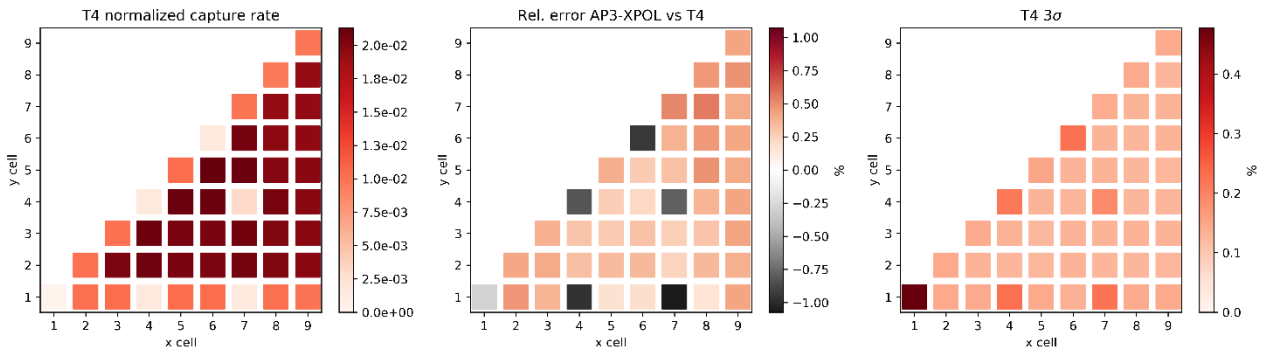


Figure B.23: Layer 7 comparison with TRIPOLI-4® for the capture rate

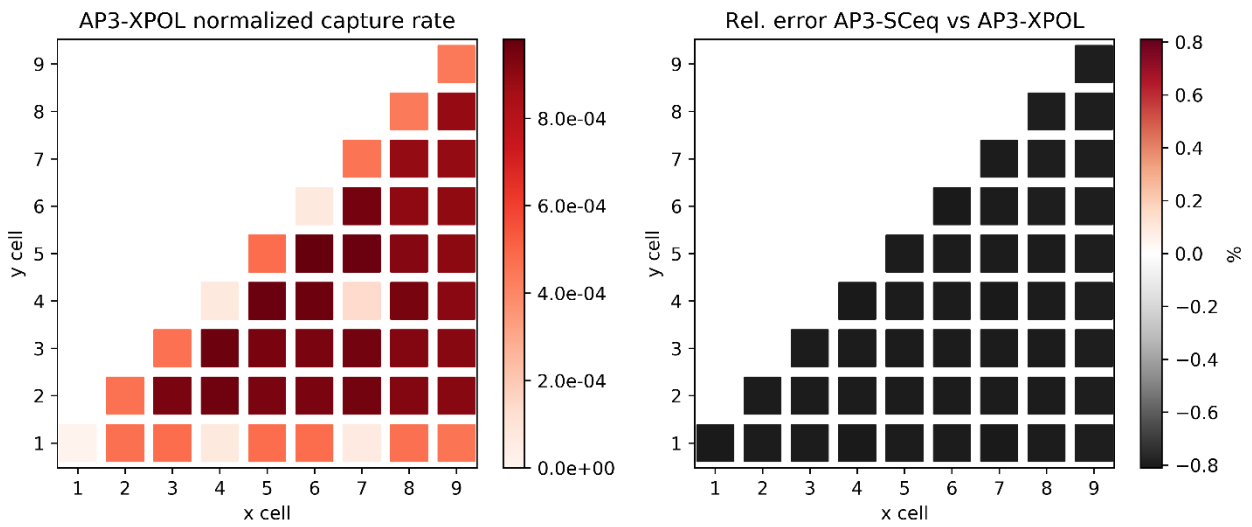


Figure B.24: Layer 8 comparison with TRIPOLI-4® for the capture rate

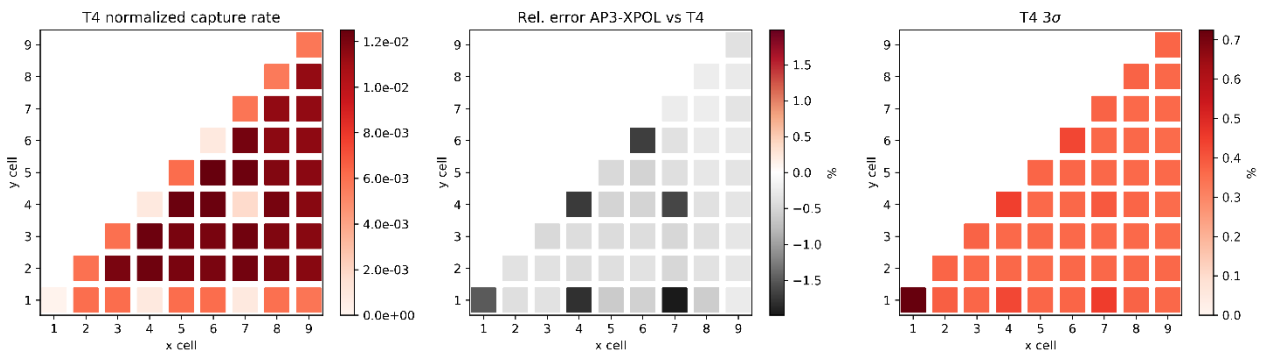


Figure B.25: Layer 9 comparison with TRIPOLI-4® for the capture rate

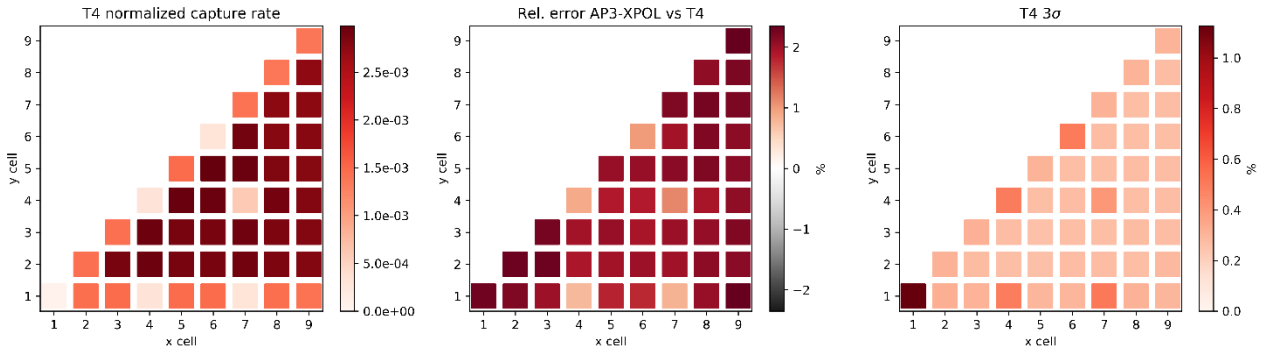


Figure B.26 : Layer 3 comparison with TRIPOLI-4® for the fission rate

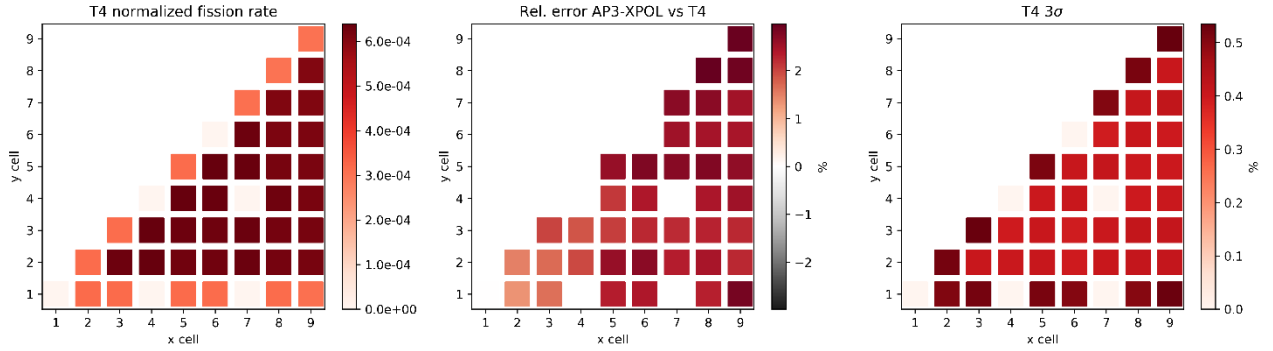


Figure B.27: Layer 4 comparison with TRIPOLI-4® for the fission rate

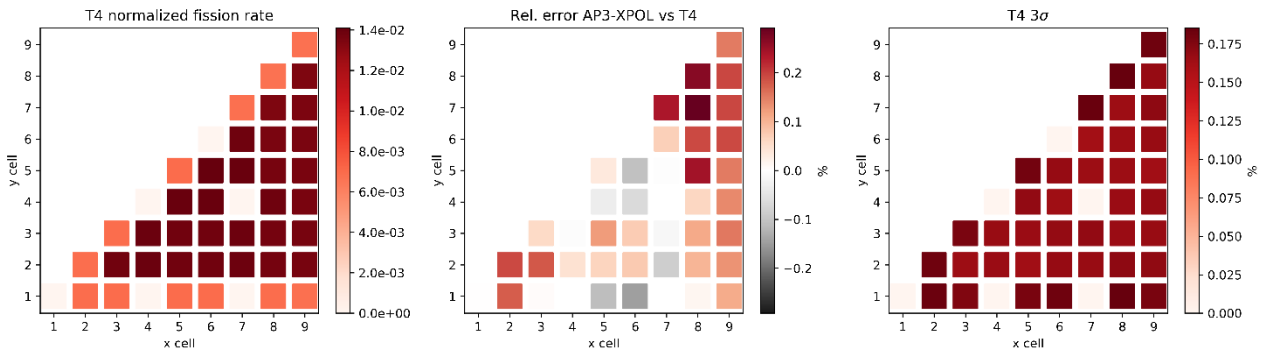


Figure B.28: Layer 5 comparison with TRIPOLI-4® for the fission rate

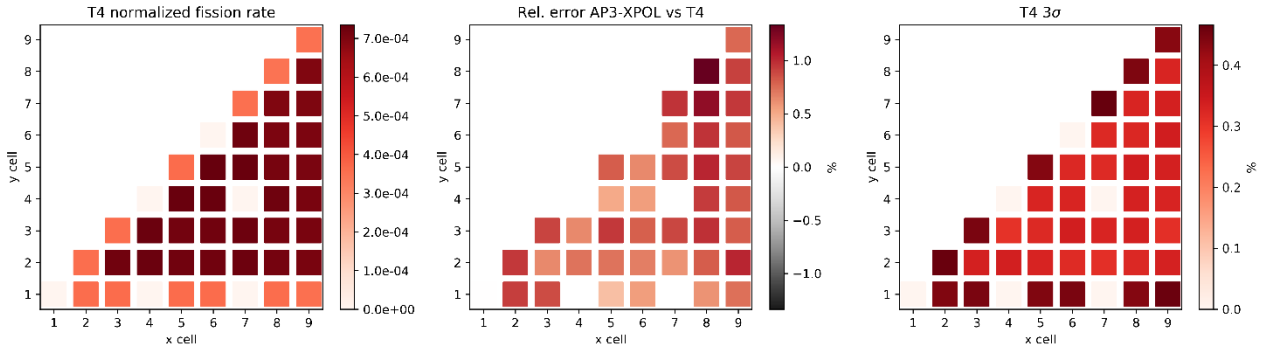


Figure B.29: Layer 6 comparison with TRIPOLI-4® for the fission rate

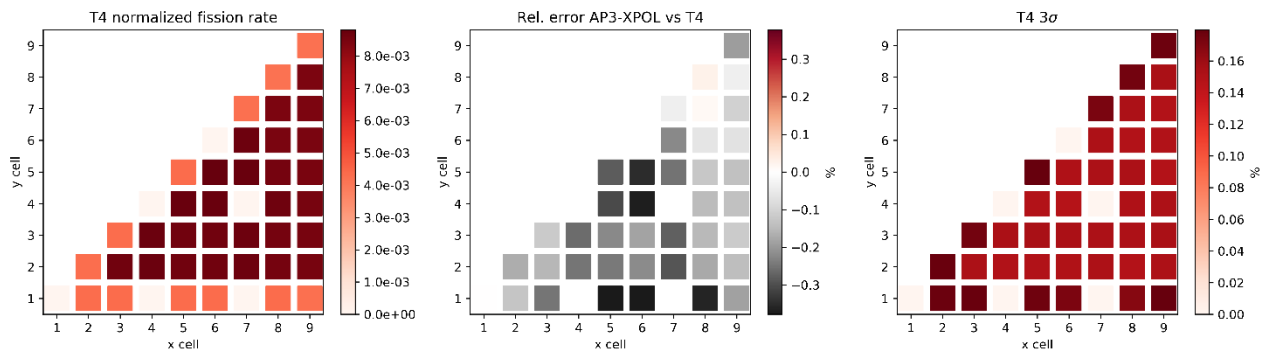


Figure B.30: Layer 7 comparison with TRIPOLI-4® for the fission rate

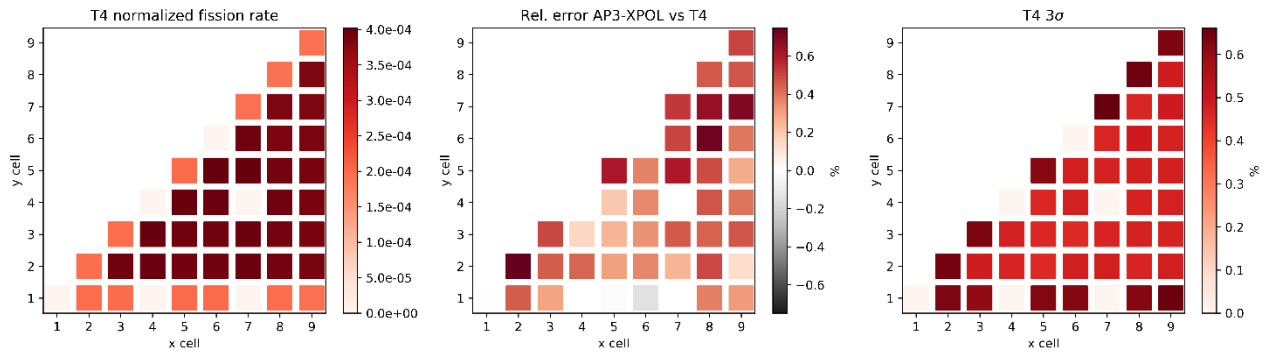


Figure B.31: Layer 8 comparison with TRIPOLI-4® for the fission rate

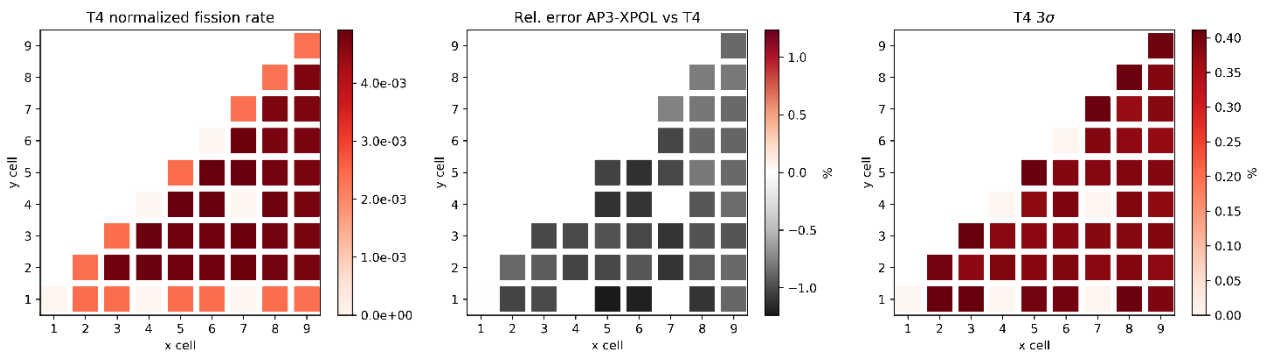


Figure B.32: Layer 9 comparison with TRIPOLI-4® for the fission rate